NASA TECHNICAL NOTE

NASA TN D-5206

C. 1

NASA TN D-5206

TURBULENCE MEASUREMENTS IN SUPERSONIC, SHOCK-FREE JETS BY THE OPTICAL CROSSED-BEAM METHOD

by
M. J. Fisher
IIT Research Institute
and
K. D. Johnston
George C. Marshall Space Flight Center

NATIONAL AERONAUTICS AND SPACE ADMINISTRATION • WASHINGTON, D. C. • FEBRUARY 1970

TURBULENCE MEASUREMENTS IN SUPERSONIC, SHOCK-FREE JETS BY THE OPTICAL CROSSED-BEAM METHOD

By M. J. Fisher

IIT Research Institute
Chicago, Ill.

and

K. D. Johnston

George C. Marshall Space Flight Center
Huntsville, Ala.

NATIONAL AERONAUTICS AND SPACE ADMINISTRATION

For sale by the Clearinghouse for Federal Scientific and Technical Information
Springfield, Virginia 22151 – Price $3.00

TABLE OF CONTENTS

LIST OF ILLUSTRATIONS

LIST OF ILLUSTRATIONS (Continued)

LIST OF ILLUSTRATIONS (Concluded)

DEFINITION OF SYMBOLS

Symbol	Definition
Å	Angstrom, 10^{-10} meter
C	Cospectrum function
D	Nozzle exit (inside) diameter
D_y	Photodetector for horizontal beam
D_z	Photodetector for vertical beam
d	Diameter of light-scattering particle
E	Three-dimensional spectrum function
E_1	One-dimensional spectrum function
f	Frequency, cps
G	$\overline{i_y (t + \tau)\ i_z (t)}$
I(t)	Radiation intensity measured by photodetector
i(t)	Deviation from time-averaged radiation intensity, $I(t) - \overline{I}$
K(t)	Radiation extinction coefficient, cm^{-1}
k(t)	Deviation from time-averaged extinction coefficient, $K(t) - \overline{K}$
L_x, L_y, L_z	Integral length scales in the x, y, and z directions
L_τ	Moving axes time scale, sec
M	Mach number
N	Concentration of light scattering particles, particles/cc
P	Pressure, N/m^2
p	Partial pressure of a gas, N/m^2

DEFINITION OF SYMBOLS (Continued)

Symbol	Definition
R_B	Two-beam correlation coefficient, Equation (23)
R_P	Two-point correlation coefficient between a point on the horizontal beam and a point on the vertical beam, Equation (5)
$r(\xi,\tau)$	Two-point space-time correlation coefficient between points B and C, Figure 1 and Equation (7)
S_x	Strouhal number, Equation (27)
T	Temperature, °C
T*	Integration time, sec
t	Time, sec
U	Mean flow speed, m/sec
V	Voltage output of detector
W	Shear layer thickness
x, y, z	Space-fixed coordinates with origin on nozzle center line at nozzle exit plane (Fig. 1)
γ	Ratio of specific heats, C_p/C_v
η	$\frac{y - D/2}{x}$
$\vec{\kappa}$	Wave number vector (directed spatial frequency) rad/m
λ	Radiation wave length
$\Delta\lambda$	Radiation wave length interval
ξ, η, ζ	Beam-fixed coordinates with origin at point B (Fig. 1)
ρ	Density, kg/m^3

DEFINITION OF SYMBOLS (Concluded)

Symbol	Definition
τ	Time delay introduced between signals from the two beams, sec
τ_P	Time lag corresponding to a peak in two-beam correlation coefficient curve
τ^*	Radiation transmission, fraction of initial radiation to penetrate the absorbing path
Ω	Solid angle
ω	Circular frequency, rad/sec

SUBSCRIPTS

a	Denotes atmospheric conditions
c	Convective quantity
e	Conditions at nozzle exit
t	Total, or stagnation, conditions

SUPERSCRIPT

$\overline{(\quad)}$	Denotes a time-averaged quantity

TURBULENCE MEASUREMENTS IN SUPERSONIC SHOCK-FREE JETS BY THE OPTICAL CROSSED-BEAM METHOD

SUMMARY

A new optical "crossed-beam" technique was used to measure the turbulence properties of two supersonic, shock-free, cold air jets. The method as used here is based on the absorption of ultraviolet radiation by air. The measurements were highly successful in that reasonable and consistent values of the turbulence properties such as convection speeds, length scales, and spectra were obtained, and the data generally followed the trends set by hot-wire measurements in subsonic jets. The most interesting feature of the crossed-beam technique which was investigated in these experiments is the possibility of a direct measurement of three-dimensional spectral density. However, the demonstration that the crossed-beam technique can be used for turbulence measurements in supersonic flow is considered to be the major accomplishment of these experiments.

INTRODUCTION

This report presents the first systematic turbulence measurements in supersonic jet shear layers (November 1966) using the recently developed optical crossed-beam correlation technique [1, 2]. Supersonic flow does not present additional difficulties to the crossed-beam method, in contrast to the hot-wire technique, since it is only necessary to penetrate the flow field with two beams of radiation which do not disturb the flow.

The measurements were made in two supersonic, shock-free, cold air jets (Mach 2.46 and 3.34) and covered the region from the nozzle exit to 8 diameters downstream. The nozzles were designed for uniform, shock-free flow to provide the simplest possible supersonic flow field. Convection speeds, eddy lifetimes, turbulence intensity profiles, length scales, and spectral densities were determined from the data. Most of the measurements were made with minimum turbulence in the jet core; however, some runs were made with a turbulence-generating screen just upstream of the nozzle throat to determine the effect of core turbulence on the shear layer. Pitot pressure profiles were also obtained to compare with the crossed-beam data.

This test is one in a series to develop the crossed-beam technique as a reliable tool to study complex supersonic turbulent flow fields such as in vehicle interstage and base regions, and interacting jets. The method of approach has been to start with the simplest subsonic flow, in which hot wire data is available for comparison, and proceed to successively more complex flow fields.

The crossed-beam apparatus was developed by the IIT Research Institute (IITRI) under contract to the Marshall Space Flight Center (MSFC). The first successful measurements were made during July 1965 at IITRI, in a subsonic jet using visible light beams and adding a water droplet tracer to the jet to modulate the intensity of the beams by scattering. The convection speeds which were obtained compared well with previous hot wire results [1] . Exploratory measurements were then made at IITRI in a supersonic jet (Mach 1.5) using an ultraviolet focussed-beam optical system without adding a tracer to the jet [4]. After these tests, the ultraviolet (uv) crossed-beam apparatus was transferred to MSFC for the measurements described in this report.

The original purpose of using ultraviolet radiation was to measure fluctuations in the thermodynamic properties of air since ultraviolet radiation is absorbed by oxygen and, therefore, the detected light intensity fluctuations would be related to the thermodynamic property fluctuations caused by the turbulence. However, the radiation was also absorbed by water vapor and scattered by various particles, so it is now uncertain which constituent caused the predominant fluctuations in radiation intensity, although a hypothesis is given in the section, Processes of Radiation Intensity Modulation. Therefore, no attempt was made to interpret these measurements in terms of thermodynamic properties; however, much useful information was obtained with only limited knowledge about the processes which created the measured signal.

This test was performed at the newly-constructed MSFC Thermo-Acoustic Jet Facility (TAJF). Since no heater was available at the TAJF at that time, the test was run using cold air. The resulting low temperatures in the jets undoubtedly caused condensation of the entrained water vapor in the shear layer (the air in the jet core was dried) and perhaps caused condensation of other constituents of air at some test conditions. Therefore, unwanted condensation droplets of unknown size and concentration contributed to the uncertainty about the processes of radiation attenuation.

The crossed-beam data are compared with published hot wire data from subsonic jets to determine the similarity between the turbulence properties of subsonic and supersonic jets.

ACKNOWLEDGMENT

We wish to acknowledge the many-contributions made to this work by Dr. A. Montgomery, Mr. G. Johnson, Mr. A. Appel, Dr. W. Davies, Mr. M. Cann, Mr. D. Prosser, Dr. R. Damkevala, Dr. M. Clinch, Mr. S. Pernic and Mr. J. Fitzgerald, all of IIT Research Institute, Chicago, Illinois. Also, we appreciate the cooperation of Mr. W. Tidmore and the facility operating crew of Northrop Space Laboratories, Huntsville, Alabama. In addition, the following personnel of the Marshall Space Flight Center are acknowledged for their help in various phases of the work: Dr. F. Krause, Mr. B. Funk, Mr. H. Belew, Mr. J. Clark, Mr. E. Simon, Mr. J. Heaman, Mr. J. Sims, Mr. R. Elkin, Mr. W. Neighbors, Mr. H. Bush, and Mr. J. Smith of the Aero-Astrodynamics Laboratory; and Mr. J. Jones and Mr. G. Curet of the Computation Laboratory.

THE CROSSED-BEAM CORRELATION TECHNIQUE

The crossed-beam technique is an optical method for measuring local turbulence properties without disturbing the flow. The method has the potential of measuring fluctuating scalar quantities such as temperature and pressure, but is incapable of measuring velocity fluctuations. Therefore, the crossed-beam technique complements, but does not substitute for, the hot-wire technique. Other possible applications include the measurement of species concentration fluctuations in a reacting flow or turbulent diffusion process by using suitable optical wavelengths.

The basic concept can be understood with the aid of Figure 1. Two mutually perpendicular beams of radiation are passed through the turbulent flow region where it is desired to obtain a local measurement. Measurements are made either with the beams intersecting or separated such that the line of minimum separation (BC) is aligned with the local mean flow direction. The case of intersecting beams is considered first. Photodetectors D_y and D_z placed outside the flow field measure the radiation intensity of the horizontal and vertical beams, respectively. Fluctuations of the detected radiation intensity are caused by turbulence-induced fluctuations in optical density. Ideally, the intensity fluctuations can be related to the fluctuations of some flow property, e.g., pressure, temperature, and species concentrations. This point is discussed later.

The intensity fluctuations measured at each detector, however, result from an integral of the fluctuations along the entire length of that beam. The essence of this technique is to retrieve the time-averaged local fluctuations from a "correlation volume" which is common to both beams by obtaining the covariance of the signals from the two detectors. The common correlation volume, which includes a portion of each beam, is centered about the beam intersection point. The size of the correlation volume is determined by the average eddy size, or integral scale, of the turbulence and not by the beams. It is assumed that the beam diameter is small compared to a typical dimension of the correlation volume. The components of the two signals which are due to fluctuations outside the correlation volume are uncorrelated and, therefore, do not contribute to the covariance; i.e., these components are "noise." Therefore, we have the problem, which is familiar in communication engineering, of extracting a common signal embedded in the noise of two other signals.

Since the mathematical formulation of the crossed-beam technique has been presented previously [1-5], only the results needed in this report are given here. The basic result, from which all other information is obtained, is the cross-correlation of the fluctuating signals received by the two detectors. This quantity is called the two-beam product mean value, $G(x+\xi, y, z, \tau)$.

$$G(x+\xi, y, z, \tau) = \lim_{T^* \to \infty} \frac{1}{T^*} \int_0^{T^*} i_y(t+\tau)\, i_z(t)\, dt = \overline{i_y(t+\tau)\, i_z(t)} \tag{1}$$

In Figure 1, the coordinates x, y, and z locate the point B. The quantity ξ is the separation distance (minimum distance) between the beams, τ is a time increment added to one of the signals during data reduction, and $i(t)$ is the fluctuating component of radiation intensity at a detector.

Turbulence Intensity

We shall first consider the case of zero beam separation, $\xi = 0$, and zero time increment, $\tau = 0$.

$$G(x, y, z) = \overline{i_y(t)\, i_z(t)} \tag{2}$$

The problem now is to interpret Equation (2) in terms of local fluctuations in the flow. As mentioned before, the technique does not yield truly pointwise information. Moreover, the spatial resolution is beyond the control of the

experimenter; it is determined by the characteristics of the turbulence, i. e., the size of the correlation volume at the beam intersection point. However, an acceptable approximation to local values can be obtained. Furthermore, for some applications it is advantageous not to obtain pointwise information, but an integral over a correlation area [6].

An interpretation of G(x, y, z) in terms of local fluctuations is given in Reference 1 and, in revised form, in Reference 3. We shall use the results of Reference 3, which shows that G(x, y, z) is a spatial double integral that is weighted by the two-point correlation coefficient to give the following approximation to the mean square of the fluctuating "extinction coefficient," k, at the point of beam intersection:

$$G(x, y, z) = \bar{I}_y \bar{I}_z \overline{k^2(x, y, z, t)} \; A(x, y, z) \quad , \tag{3a}$$

where

$$A(x, y, z) \equiv \int_{\zeta} \int_{\eta} R_P(x, y+\eta, z+\zeta)\, d\eta\, d\zeta \quad . \tag{3b}$$

Now, k(x, y, z, t) is the deviation from the time-averaged extinction coefficient, $\overline{K(x,y,z,t)}$

$$k(x, y, z, t) = K(x, y, z, t) - \overline{K(x, y, z, t)} \tag{4}$$

The term "extinction coefficient," the "constant" of the Lambert-Beer law, is used here for any type of absorption or scattering process following the practice of Reference 7. Since we are dealing with a turbulent, optically inhomogeneous medium, K is not a constant, but is a function of position and time. The connection between K and the desired flow properties is discussed later.

The quantity A(x, y, z) is called the integral correlation area, by analogy to the familiar integral length scale. It can be regarded as the cross-sectional area, in the plane of the beams, of the common correlation volume at the beam intersection point. The integrand of Equation (3b) is the correlation coefficient between a point on the y beam and a point on the z beam; the coordinates η and ζ give the distances of these points from the beam intersection point.

$$R_p(x, y+\eta, z+\zeta) = \frac{\overline{k(x, y+\eta, z, t)\; k(x, y, z+\zeta, t)}}{\left[\overline{k^2(x, y+\eta, z, t)}\;\; \overline{k^2(x, y, z+\zeta, t)}\right]^{\frac{1}{2}}} \quad . \qquad (5)$$

The approximation of Equation (3a) is "exact" for the case of locally homogeneous turbulence, where $\overline{k^2}$ is independent of position within the common correlation volume. Reference 3 gives arguments to show that Equation (3a) is a good approximation also for the most probable types of inhomogeneous turbulence. Therefore, we have a method to estimate pointwise turbulence intensities from crossed-beam measurements if we can determine $A(x, y, z)$. If we can assume that $A(x, y, z)$ is constant along a chosen direction, we can obtain a relative intensity profile in that direction without knowing $A(x, y, z)$. If we use the approximation of Reference 1

$$A(x, y, z) = L_y L_z \qquad (6)$$

where L_y and L_z are the integral length scales in the y and z directions, we see that $A(x, y, z)$ is constant across the flow field if the length scales are constant. The assumption of constant length scales is justified even in some cases of inhomogeneous turbulence; e.g., Reference 11 shows that the radial length scales in a subsonic jet are relatively constant in planes perpendicular to the mean flow direction and vary significantly only in the streamwise direction. However, to obtain absolute values of $\overline{k^2(x, y, z, t)}$, the length scales must first be estimated, and this is considered later.

An alternate interpretation of $G(x,y,z)$ as an area integral of the product of the extinction coefficient $k(x, y, z, t)$ at the beam intersection point with $k(x, y+\eta, z+\zeta, t)$ at all other points on the surrounding correlation area was given by Krause in Reference 5 for the conditions of homogeneous turbulence and in Reference 8 for more general conditions.

Measurement of the local mean square extinction coefficient, $\overline{k^2(x, y, z, t)}$, using Equation (3) does not yield directly the absolute magnitude of any particular property of the flow. One must first find a "calibration factor" which relates $\overline{k^2(x, y, z, t)}$ to a desired flow property, e.g., pressure or temperature. To obtain such information, it is desirable that only one constituent of the flow attenuates the intensity of the beam. Secondly, the radiation should preferably be attenuated only by the desired property, although

this is not essential in some cases. Finally, one must find the relation between the desired property and the extinction coefficient. There are two different approaches to this problem, one method using light scattering from tracer particles placed in the flow and the other method using absorption by a gaseous constituent.

If the flow is seeded with solid particles of uniform size and if the proper radiation wavelength is chosen such that the light is scattered by the particles but not attenuated by other constituents, then the local extinction coefficient is proportional to the local concentration of the particles [7]. Therefore, fluctuations in particle concentration causes fluctuations in the measured radiation intensity. Now, if the relationship between particle concentration fluctuations and fluctuations of a flow property can be found, we are then able to obtain the desired local property fluctuations from crossed-beam measurements.

Alternatively, we could use a radiation wavelength which is absorbed by a gaseous constituent of the flow. The fluctuations of the extinction coefficient are then caused by fluctuations in thermodynamic properties or species concentration of the flow. By appropriate selection of wavelength, λ, and wavelength interval, $\Delta\lambda$, we can in some cases arrange that the extinction coefficient is dependent predominantly on one thermodynamic property, e.g., pressure.

Then by selection of another wavelength, we can choose a different thermodynamic property, e.g., temperature. This selectivity makes this method potentially very powerful. By spectroscopic analysis of crossed-beam data, using laboratory calibration measurements and absorption band model theories, we can obtain the desired thermodynamic property fluctuations. A possibility exists that this can also be done if the absorption depends on more than one thermodynamic property [9, Part II]. Reference 9 describes the initial effort in spectroscopic crossed-beam analysis, and Reference 10 discusses the possibility of measuring mean values of thermodynamic properties. Also, by appropriate choice of wavelength, we could measure concentration fluctuations of one species in a non-uniform mixture of gases.

It must be emphasized that complicated calibration procedures are not necessary to determine certain inportant turbulence properties which are frequently called the kinematic properties, e.g., convection speeds, eddy lifetimes, relative intensity profiles, integral length scales, and relative power spectra. However, at least some of the above properties can be different for different fluctuating quantities of the turbulent field; e.g., the length scale of temperature fluctuations can differ from the length scale of velocity fluctuations. Therefore, it is highly advantageous, even in measuring kinematic properties, to be able to select a wavelength, λ, so that the desired thermodynamic property causes the predominant modulation of the beams.

Two-Point Space-Time Correlation Coefficient

It was shown in Reference 1 that an acceptable estimate of the cross-correlation coefficient between two points separated by a distance ξ along a streamline is given by:

$$r(\xi,\tau) = \frac{G(x+\xi,\ y,\ z,\ \tau)}{G(x,\ y,\ z)} \tag{7}$$

By using several different beam separation distances, ξ, we can obtain a set of space-time correlation curves from which the convection speed and eddy lifetime can be easily determined.

Length Scales

The integral length scale in the streamwise direction can be obtained from Equation (7).

$$L_x = \int_{-\infty}^{\infty} r(\xi, 0)\, d\xi \tag{8}$$

This definition, which is convenient for crossed-beam work, is just twice that normally used, because the integration extends in the negative as well as positive direction.

The length scales L_y and L_z in two perpendicular cross-flow directions are needed for an estimate of A from Equation (6). The scale L_y in this report is measured in the radial (outward from jet centerline) direction, and L_z is measured perpendicular to L_y in the circumferential or tangential direction. This notation was used because all measurements were made in a horizontal plane which contained the jet centerline and, there, y and z corresponded to the radial and circumferential directions, respectively. A method for estimating L_z is given in Reference 4.

$$L_z = \int_{-\infty}^{\infty} \frac{\bar{I}_y}{\bar{I}_z} \frac{G(x,\ y,\ z)}{\overline{i_y^2(t)}}\, dy \tag{9}$$

To evaluate this integral numerically, the horizontal beam is kept fixed and the vertical beam is moved in small increments to intersect the horizontal beam at a number of y locations so that the dependency of G(x, y, z) and $\overline{I}_z$ on y can be determined across the entire turbulent flow region. In the derivation of Equation (9), it was necessary to assume that both L_y and L_z are invariant along the y direction within the region of turbulence. This condition is, of course, met in the special case of homogeneous turbulence; furthermore, as mentioned earlier, it is also met for some cases of inhomogeneous turbulence as was shown, at least for L_y, in subsonic jets [11]. L_y can also be obtained from Equation (9) by interchanging y and z, keeping the vertical beam fixed and moving the horizontal beam, if we can reasonably assume that the length scales are constant along the z direction.

Spectra

To obtain the spectral analysis of local fluctuations, we can Fourier-transform the quantity G from Equation (1). However, since G results from an integration by the beams over a correlation volume, we do not get the one-dimensional spectrum which would be obtained from a point probe measurement. Instead, a function which resembles mathematically the three-dimensional spectral density is obtained. This was recognized by Krause [6] quite early in the formulation of the crossed-beam concept; however, this is the first attempt to investigate this feature experimentally.

Equation (1) can be expressed in the following way [1]:

$$G(x+\xi, y, z, \tau) = \overline{I}_y \overline{I}_z \int_{-\infty}^{\infty} \int \overline{k(x, y+\eta, z, t+\tau)\, k(x+\xi, y, z+\zeta, t)}\, d\eta d\zeta . \tag{10}$$

The point $(x, y+\eta, z)$ is on the horizontal beam and the point $(x+\xi, y, z+\zeta)$ is on the vertical beam. The double line integral is accomplished by optical integration along the beams.

Now, following Hinze [12], the three-dimensional spectral density of a scalar quantity k is given by

$$E(\kappa_x, \kappa_y, \kappa_z) = \frac{1}{8\pi^3} \int\int\int_{-\infty}^{\infty} k(x, y, z, t)\, \overline{k(x+\xi, y+\eta, z+\zeta, t)}\, e^{-i(\kappa_x \xi + \kappa_y \eta + \kappa_z \zeta)}\, d\xi\, d\eta\, d\zeta . \tag{11}$$

This is identical to Hinze's function $E\gamma, \gamma$ for scalar quantities and is analogous to the three-dimensional spectrum tensor for vector quantities, $E_{i,j}$. By restricting $\vec{\kappa}$ to the streamwise, or x direction, we get

$$E(\kappa_x, 0, 0) = \frac{1}{8\pi^3} \int_{-\infty}^{\infty} \left[\int\int_{-\infty}^{\infty} \overline{k(x, y, z, t)\ k(x+\xi, y+\eta, z+\zeta, t)}\, d\eta\, d\zeta \right] e^{-(i\kappa_x \xi)} d\xi \ . \tag{12}$$

The quantity in brackets is very similar to Equation (10). In fact, if we assume local homogeneous turbulence in the region of minimum beam separation, we have

$$\overline{k(x, y+\eta, z, t)\ k(x+\xi, y, z+\zeta, t)} = \overline{k(x, y, z, t)\ k(x+\xi, y-\eta, z+\zeta, t)} \ . \tag{13}$$

Upon substitution of Equation (13) in Equation (10), the integral of Equation (10) becomes identical to the brackets of Equation (12); this is also true for inhomogeneous turbulence if the inhomogeneity is a linear or an odd function of η or ζ [3, 8]. Therefore, we obtain the following:

$$E(\kappa_x, 0, 0) = \frac{1}{8\pi^3} \int_{-\infty}^{\infty} \frac{G(x+\xi, y, z, \tau=0)}{\bar{I}_y \bar{I}_z} e^{-(i\kappa_x \xi)} d\xi \ . \tag{14}$$

This gives the energy per unit volume of wave number space for wave number of magnitude κ_x in the streamwise direction.

To evaluate the integral of Equation (14), a large number of measurements must be made with different beam separations, ξ. However, it is more convenient to make only one measurement with intersecting beams and use Taylor's hypothesis to substitute a time increment for the space increment in the stream direction:

$$\xi = U_c \tau \ . \tag{15}$$

It should be kept in mind that Equation (15) is an approximation and involves the assumptions of constant convection speed, homogeneity, and small fluctuations, and is not recommended for use in shear flow [12]. Nevertheless, for the purpose of this report, it was decided to use Equation (15) to reduce the number of experiments to manageable proportions. Substituting Equation (15) into Equation (14) yields:

$$E(\kappa_x, 0, 0) = \frac{U_c}{8\pi^3 \bar{I}_y \bar{I}_z} \int_{-\infty}^{\infty} G(x, y, z, \tau)\, e^{-(i\kappa_x U_c \tau)} d\tau \quad . \tag{16}$$

Because it usually proves more convenient to compute the frequency spectrum rather than the wave number spectrum, the following convective flow approximation is used:

$$\omega_x = \kappa_x U_c \tag{17}$$

and

$$E(\omega_x, 0, 0) = \frac{U_c}{8\pi^3 \bar{I}_y \bar{I}_z} \int_{-\infty}^{\infty} G(x, y, z, \tau)\, e^{-(i\omega_x \tau)} d\tau \quad . \tag{18}$$

This equation is used later to compute power spectra.

EXPERIMENTAL APPARATUS

The apparatus used in these experiments consisted of the crossed-beam system, Pitot pressure probes, fluctuating pressure transducers, microphones, and schlieren and shadowgraph equipment. Only the crossed-beam and Pitot probe systems are described because they provided the most important data.

Crossed-Beam System Mechanical Support

A photograph of the crossed-beam apparatus at the test site is shown in Figure 2. The optical components are mounted on a modified lathe bed to facilitate positioning the beams. The light sources and spectrometer systems for both horizontal and vertical beams are mounted on a movable framework so that both beams can be moved simultaneously to any desired axial location along the jet. The horizontal beam, which does not have the capability of vertical motion, is positioned to go through the center of the jet. The vertical beam can be moved relative to the horizontal beam in the streamwise, x, and crossflow, y, directions by means of an auxiliary traverse mechanism which is mounted on the larger framework. A combination of these motions allows us to intersect the beams anywhere in a horizontal plane which contains the centerline of the jet, or to separate them in the streamwise direction.

Selection of Radiation Wavelength

Ultraviolet radiation was selected for these experiments in an effort to measure thermodynamic property fluctuations. Of course, any wavelength which is absorbed by some constituent of air could have been used. In fact, it now appears that an infrared wavelength might have been preferable.

Figure 3 gives some experimental data from Reference 9 which shows the variation of radiation transmission, τ^*, with optical wavelength, λ, and pressure, P, for a path length of 34.25 cm and a constant temperature of approximately 310°K. The transmission, τ^*, is the fraction of radiative energy which penetrates the absorbing path. The air used in this experiment was practically free of water vapor and carbon dioxide. The absorption in this wavelength band ($1750 < \lambda < 1900$Å) is primarily due to the Schumann-Runge bands of oxygen at moderate pressures. However, water vapor also absorbs in this band, and if a significant percentage of water vapor is present, its contribution to the total absorption can be appreciable [9, Part I]. The effects of water vapor on the measurements of this report are discussed in the section, Processes of Radiation Intensity Modulation. The absorption by oxygen is also dependent on temperature, although to a lesser degree than on pressure. Therefore, one is faced with the problem of separating the contributions of pressure and temperature [9, Part II].

A wavelength of 1850Å was selected for these experiments. This wavelength was chosen because it corresponded to a relative maximum in emissive power of the light source which was used and also gave the largest ratio of fluctuating signal to shot noise for a given rms pressure level as determined by measurements in a dynamic absorption calibration cell. The mean transmission was in the range 0.45 to 0.60 for this wavelength at atmospheric pressure for the absorbing path lengths which were used (approximately 30 and 48 cm for the vertical and horizontal beams, respectively). Although there is an optimum transmission for any given experiment [3], any τ^* in a range of about 0.3 to 0.7 is considered satisfactory. To obtain sufficient radiative power, a rather broad bandpass, $\Delta\lambda$, of 50Å centered about 1850Å was chosen.

The Optical System

Figure 4 shows the arrangement of the optical components. The major components for both beams are identical, but the focusing optics are arranged differently. The components are listed below along with a brief discussion of each. A more complete discussion is given in Reference 13.

Light source. McPherson Model 630 vacuum ultraviolet discharge lamp.

The lamps were operated with research grade hydrogen at 15 mm Hg pressure and 0.6 amperes. They were powered by separate Forest Electric Co. Model W-1356 dc power sources which had less than 0.1 percent voltage ripple. The operating voltage was approximately 2000. The lamps had relatively large radiative power output in the ultraviolet range of interest with a relative peak at approximately 1850Å. However, the power output was still inadequate to obtain a good signal-to-noise ratio (to be discussed later). This is the main drawback in using ultraviolet radiation for crossed-beam applications.

Monochromator. Jarrell Ash Model 84-110, 0.5 meter vacuum Ebert type with grating of 1180 lines per millimeter.

The monochromators were used to select a bandpass of 50Å, centered about 1850Å, from the radiation spectrum emitted by the McPherson lamps. Although partially shielded from jet noise by thick acoustic insulation shields, the monochromators were not entirely covered.

Photo-detector. EMR Model 541 A-05-14 multiplier phototube.

The phototubes were bolted to the monochromators at the exit slit. They had adequate frequency response characteristics and radiant sensitivity (about 0.018 amp/watt at 1850Å). They were powered by John Fluke Model 404 M dc power sources at about 1200 volts. (Reference 13 erroneously listed the photo-detectors as EMR model 543F-05-14.)

Focusing Optics. Both beams were focused at the point of beam intersection by suprasil lenses. The purpose of focused beams is discussed later. Although a mirror system would have been preferable, the lenses were chosen because they were quicker and cheaper to make and install. The suprasil gives satisfactory transmission at 1850Å, e.g. $\tau^* \approx 0.80$ for 10 mm thickness. The lenses of the vertical beam were fixed so that the focal point always remained in a horizontal plane which contained the centerline of the jet. The focal point position of the horizontal beam could be easily moved by sliding the two inner lenses the same distance. The beam path between the lens and the light source on one side and between the lens and the monochromator on the other was enclosed and leak-sealed to maintain a vacuum. This left an absorbing path of 30 cm for the vertical beam and about 48 cm for the horizontal beam.

Vacuum System. The monochromators and beam enclosures were evacuated to a pressure of approximately 5 to 10 mm Hg by rotary vacuum pumps to minimize radiation absorption except along the unenclosed path through the jet.

The purpose of using focused beams rather than collimated beams was to increase the radiative power incident on the detector and thereby increase the signal-to-detector noise ratio. (Detector noise is discussed in Reference 14.) Originally, collimated beams of 2 mm diameter were used which resulted in a mean signal to rms noise ratio of about 70. However, this ratio proved insufficient to allow practical and reliable computation of the small values of G which are obtained by the crossed-beam method, although some degree of success was attained.

Since the mean detected signal is proportional to the mean incident radiative power and the rms shot noise is just proportional to the square root of this power, a considerable improvement in the ratio of signal to shot-noise can be obtained by using a greater percentage of the source power. This was accomplished by accepting a much greater solid angle ($\Omega \approx 0.012$) from the source and focusing this light at the point where the two beams intersected. This still gave rather small beam diameters within the local correlation volume surrounding the beam intersection point. This change resulted in a mean signal to rms noise ratio of about 500. This improvement (factor of 7) made computation much easier and more practical. No significant difference is expected in the value of G due to the difference in shape of the collimated and focused beams. The focused beams have the additional advantage that they reduce the effect of scattering particles.

Data Acquisition Chain

A block diagram of the data acquisition chain is shown in Figure 5a. Each component is described briefly below. For more information, see Reference 13.

Amplifier. Constructed by the IIT Research Institute from Fairchild solid state components, the amplifiers, located adjacent to the photo-detectors (Fig. 2), had a fixed gain of 1000. This large gain was desirable to minimize acoustic pickup in the coaxial cables which led to the data acquisition equipment and also to minimize loss of high frequency response due to the capacitance of these cables which were approximately 11 meters long. The amplifiers were ac coupled to give a low frequency cutoff of approximately 200 cps.

Emitter Follower. Constructed by the IIT Research Institute, the emitter followers, located near the amplifiers (Fig. 2), served to match impedances between the photo-detector and tape recorder and other monitoring devices for maximum power transmission.

Attenuator. Daven attenuators with small adjustments from 0.1 dB to 100 dB were used to reduce the signal voltage to the appropriate level for the tape recorder. The attenuators, as well as all remaining equipment, were located in the instrumentation room (Fig. 6).

Filter. Allison Model 2-BR high and low pass electronic filters were used to limit the electronic bandpass from 400 to 20 000 cps. This bandpass was chosen to eliminate 120 cps ripple introduced by the light source power supplies and also to eliminate detector noise at those frequencies where no appreciable signal amplitude was expected.

A frequency response check of the data acquisition chains from the amplifiers through the filters revealed a flat frequency response from 300 to 20 000 cps. Also, a check of the phase matching between the two data acquisition chains showed satisfactory agreement.

D. C. Voltmeter. The mean voltage from each photo-detector was measured via a secondary cable which was connected between the photo-detector and amplifier. When fluctuating data were being recorded, the dc cable was disconnected by means of a remotely operated two-way relay switch.

Tape Recorder System. CEC Model VR 3600 tape machine with Data Control Systems multiplex equipment was used to record the fluctuating signals from each beam on magnetic tape for storage and subsequent data reduction. A multiplex tape recorder system was used to minimize phase errors by storing both signals on one tape track and thereby avoiding interchannel time displacements. A block diagram of this system is shown in Figure 5b. The excellent frequency response characteristics of the system are shown in Figure 7. Its upper usable frequency limit is about 50 000 cps which was more than adequate for this test.

Analog Time Delay Correlator. The Honeywell Model 9410, used for on-line determination of correlation functions, was particularly useful for exploratory testing to find those locations where significant correlations could be obtained.

Pitot Probe System

The Pitot pressure was measured with a pneumatically actuated traversing pressure probe shown in Figure 8a. The probe moved continuously across the jet at the rate of 0. 5 cm per second to obtain a complete pressure profile in one run. The pressure was sampled at the rate of five times per second to give ten points per cm. The position of the probe was monitored by a potentiometer. This system had adequate position accuracy and time response as shown by the excellent agreement of the data with measurements in the same jets using accurately positioned stationary pressure rakes [15]. A block diagram of the data acquisition system is shown in Figure 8b. The maximum error in the measured pressures is supposed to be less than 1 percent.

THE THERMO-ACOUSTIC JET FACILITY

The Thermo-Acoustic Jet Facility (TAJF), a plan view of which is shown in Figure 9, consists of a cold flow air jet facility, a heated jet facility which can use any desired gas, and an acoustically insulated instrumentation room. Since the heater had not been installed at that time, this test was conducted on the cold flow jet facility. This facility consists of a pressure control valve system and a settling chamber to which any desired nozzle can be attached. Figure 10 is a photograph of the facility, and Figure 11 gives a cross-sectional view of the settling chamber. The facility has the capability for a wide range of mass flow rate and pressure up to a maximum of about 82 kg/sec (180 lb/sec) at 1.72×10^7 N/m^2 (2500 psi). The stagnation pressure can be controlled so that the maximum deviations from the mean are only about ± 0.3 percent. Because of the large air supply capacity, sufficient air was usually available to run as long and often as desired.

A honeycomb and five screens are placed in the upstream end of the settling chamber to damp the turbulence generated in the pipes and valves. Figure 12 gives the noise levels measured in the settling chamber. Turbulence can be added to the jet core, if desired, by placing coarse screens at two locations just upstream of the nozzle in the high flow speed region (Fig. 11). The screens are held in place by retainer rings which fit into large circumferential slots. Normally, when the screens are not used, the wall contour is kept smooth by placing filler rings in the slots. Unfortunately, the filler rings were inadvertently left out for most of the crossed-beam measurements. This omission was discovered only when the screens were installed before the last few runs of the test. Although a later check of the static pressures along the

nozzle walls with and without the slots showed no measurable effect of the slots (Fig. 14), it is not known to what extent the slots affected the crossed-beam data.

The settling chamber and all other parts downstream of the control valves were made of stainless steel to prevent corrosion and the consequent roughening of the walls and contamination of the flow. The supply air is dried to a specific humidity of 10^{-6} to 3×10^{-6}, so that no corrosion will occur in the supply pipes. However, a thin film of powder on the settling chamber walls after the test showed that solid particles were present in the flow. This was attributed to the drying agent.

The air in the storage tanks was usually at about atmospheric temperature. However, because of the Joule-Thomson cooling effect in the control valves, the stagnation temperature was quite low (+6° C to -13° C). This caused extremely low temperatures in the jets.

NOZZLES

It was desired to perform the crossed-beam measurements in the simplest possible supersonic jets and to compare the data with published hot-wire results for subsonic jets. Therefore, nozzles were designed to obtain supersonic jets which would have the closest possible similarity to subsonic jets. Each jet was to (1) have uniform velocity across the nozzle exit plane, (2) be free of shocks, and (3) have a jet boundary which would deviate from a circular cylinder only because of shear layer growth, i.e., no billowing or contraction of the plume due to pressure forces. All three conditions are synonymous as far as nozzle design is concerned.

Two nozzles with exit Mach numbers of 2.5 and 3.4 were chosen to determine the influence of Mach number on the turbulence properties. Mach 3.4 was thought to be the highest Mach number which could be attained and still avoid air liquefaction. However, because inadequate allowance was made for the temperature decrease across the control valves, the equilibrium liquefaction temperature was reached for some runs.

The nozzle contours were computed using the method of characteristics. These contours were corrected for boundary layer displacement thickness following the method of Reference 16. The relative size of the two nozzles was chosen so that they produced equal thrust when operated at their design stagnation pressures.[1] The nozzles are shown in Figure 13.

1. The authors are grateful to Mr. J. Sims and Mr. R. Elkin of MSFC for computing the nozzle contours and boundary layer corrections, respectively.

Figure 14a shows the Mach number profiles along the walls of the two nozzles as determined by static pressure measurements. As stated in the preceding section, the presence of the slots upstream of the nozzle throat did not affect these data appreciably. The cause of the upturn in indicated Mach number near the exit of the Mach 3. 4 nozzle is not known. However, since it was consistent throughout the calibration test at various stagnation pressures, it might be a real effect. Figure 14b shows the Mach number distributions, determined from the Pitot pressure rake measurements of Reference 15, across the nozzle exit planes. Both sets of data show that the actual Mach numbers obtained at the nozzle exits were slightly less than the design values. The approximate Mach numbers obtained by averaging these results are 2. 46 and 3. 34. The discrepancies were perhaps partially caused by inadequate correction for boundary layer displacement thicknesses since errors of 0. 066 cm (Mach 2. 5 nozzle) and 0. 074 cm (Mach 3. 4 nozzle) at the nozzle exits would account for the observed effects.

The ratio of stagnation pressure to ambient atmospheric pressure for on-design ($P_e = P_a$) operation is 16. 05 for the Mach 2. 46 nozzle and 60. 64 for the Mach 3. 34 nozzle. The stagnation pressure was varied with changes in atmospheric pressure throughout the test to maintain these ratios.

Figures 15 and 16 are shadowgraph and schlieren photographs of the jets when operated at their design pressure ratios. The photographs show that the jets were free of shocks, or very nearly so, since the Mach lines emanating from the lip of each nozzle were parallel to the other Mach lines in that jet. The Mach angles correspond to the same Mach numbers, within measurement accuracy, which were determined from the pressure measurements. The Pitot pressure profiles measured downstream of the nozzle exits [15] also indicate that the jets were free of shocks when operated at the design stagnation pressures, because the pressure profiles were uniform across the potential flow region.

It is interesting to note from Figure 12 that a microphone placed near a nozzle exit measures a minimum in noise level at a pressure near the design value.

THE EXPERIMENTS

The objective of this test was to determine the turbulence properties of the jet shear layers at several axial locations. At each selected axial location,

an "intensity traverse" was first made to determine the turbulence intensity profile. This consisted of the following steps:

1. The beams were intersected at the jet axis ($y = 0$).

2. With the jet operating at its design stagnation pressure, the covariance of the detector outputs and their individual mean square levels were determined on-line, using the analog correlator. The mean signal levels were measured with the dc voltmeter. No data were recorded on the tape machine.

3. The beams were then intersected at a new "y" position by keeping the horizontal beam fixed, except to move the focal point, and moving the vertical beam in the "y" direction. The measurements were then repeated.

4. This process was repeated for successively larger values of "y" until the measured covariance first increased sharply, indicating that the beams were intersecting in the shear layer, and then dropped to zero, indicating that the intersection point had moved outside the shear layer.

The information obtained was sufficient to determine the turbulence intensity profile and the integral length scale L_z. From the intensity profile, several "y" locations, usually five, were selected at which to make space-time correlation measurements to obtain the remaining turbulence properties. These five "y" positions covered the range of measurable covariance. The following procedure was used:

1. The beams were intersected at a point (x, y, o) corresponding to one of the five selected "y" positions at the axial location where the intensity traverse was made. The signals were recorded on magnetic tape for approximately 15 seconds.

2. Next, the horizontal beam was left fixed, and the vertical beam was moved a short distance in the "x" direction to introduce a streamwise beam separation. The data were again recorded as above.

3. Step 2 was repeated at successively larger "x" values for a total, in most cases, of five beam separations.

4. Steps 1 through 3 were then repeated for the other four selected "y" positions.

Intensity traverses were made at x/D of one, four, and eight in the Mach 3.34 jet and at one, two, and four in the Mach 2.46 jet. Space-time measurements were made at x/D of one, four, and eight in the Mach 3.34 jet and at two and four, with and without a turbulence-producing screen, in the Mach 2.46 jet. Three hundred runs were made in the crossed-beam test.

No serious problems developed during the testing. The worst difficulty experienced was a continuous decrease in radiation intensity due to deposition of electrode material on the lamp windows. It was necessary to clean the lamp windows after every six or eight hours of operation. This problem could have been alleviated if the hydrogen had been run continuously through the lamps. However, since it was thought that this advantage might be offset by fluctuations in radiation intensity caused by the flowing hydrogen, the lamps were run with still hydrogen.

It had been feared that the noise and vibration might cause difficulties with the instrumentation, particularly the monochromators. However, the instrumentation operated in a noise environment of about 150 dB (Fig. 12) without difficulty. In addition to the effect of the noise shields, evacuation of the monochromators prevented direct transmission of sound to the gratings and mirrors. Because the supporting framework was remarkably stable to the touch during jet operation, the effect of fluctuating motions of the beams was considered insignificant.

As noted previously, the mean signal to rms noise ratio with no flow was roughly 500. The maximum ratio of rms fluctuating signal with jet on, $V_{rms(jet\ on)}$, to rms noise with jet off, $V_{rms(jet\ off)}$, was about 3.34 for both beams. The ratio of $V_{rms(jet\ on)}$ to $V_{rms(jet\ off)}$ for the vertical beam was typically 1.5 when the beam was moved to a "y" position for which the covariance between beams became zero. This rather small increase in noise level due to the jet running probably had several causes including small contributions from jet noise, vibration, and radiation intensity fluctuations caused by particles being entrained in the jet outside the region of beam intersection. It is not known which of these sources was the dominant contributor to the extra jet-on noise. However, it is important to note that this noise was not correlated between the two beams; the covariance always dropped to zero when the vertical beam was moved outside the jet. Therefore, the jet-on noise caused no major problem.

DATA REDUCTION

The turbulence intensity profiles were obtained using the analog correlator on-line to compute the covariance between the two signals. The space-time correlation and power spectra were computed digitally from the tape-recorded data. The data reduction chain is shown in Figure 17. Each signal was digitized at the rate of 20 000 samples per second at a tape speed of 1/8 the record speed. This gave a real-time sampling rate of 160 000 samples per second, which was more than adequate for the frequency bandwidth (400-20 000 cps) of the data.

The computer program used in this work was developed especially to analyze crossed-beam data [17]. Its principal features are (1) a "piecewise" operation in computing correlation coefficients, (2) computation of confidence intervals for the correlation coefficients, (3) limitation of computer time to the minimum required to obtain the statistical accuracy requested by the experimenter, and (4) computation of power spectra. The program has the capability of extracting small correlations from large noise, provided the data are stationary, by extending the integration time "indefinitely." This feature is very advantageous for crossed-beam applications because it is routinely necessary to compute correlation coefficient curves with peak values smaller than 0.1 and sometimes as small as 0.01.

The program operates in the following way. A short data piece (three times the maximum time lag) of each signal is first accepted from the digital tape and the cross-correlation coefficient is calculated. Successive pieces of the same length are similarly processed to obtain a resultant correlation coefficient which is the average of those for all previous pieces. The standard deviation and confidence interval of the correlation coefficients are computed. After each data piece is processed, the program asks if the specified confidence interval at the required degree of confidence has been attained. If not, more pieces are processed until the desired statistical accuracy is reached or the data are exhausted. For the data presented in this report, the confidence intervals for correlation coefficients were varied between 0.010 and 0.020 with a degree of confidence of 95 percent. After the correlation curve is computed to the required accuracy, a Fourier transform is performed, Equation (18), to find the power spectra, if they are desired.

Figure 18a gives the average confidence interval, at a degree of confidence of 0.95, as a function of integration time for a typical run. This confidence interval is an average of the confidence intervals for all time lags, and the integration time is the total length of data processed, in seconds, up to the data piece in question. A total of 9.99 seconds of data consisting of 14 800 pieces was processed. To obtain the average confidence interval of 0.02, which was most frequently used in this work, it was necessary to process about two seconds of data. It usually took about 10 minutes of computer time to compute a correlation curve, consisting of about 30 time lags, to this accuracy.

The same data are plotted in the insert as a function of $\frac{1}{\sqrt{T^*}}$. This shows that the confidence interval was a linear function of $\frac{1}{\sqrt{T^*}}$, which is an indication that the data were stationary. An extrapolation of the curve to $\frac{1}{\sqrt{T^*}} = 0$ gives zero confidence interval, which implies that any desired confidence interval can be obtained if one is willing to expend the necessary computer time. Expressed another way, very small correlation coefficients can be extracted from signals which consist primarily of noise, provided enough computer time is available. Of course, several practical limits exist which place a lower boundary on the size of correlation coefficients which can be reliably computed [3].

Figure 18b shows the correlation coefficient curve for several integration times up to a maximum of 9.99 seconds. Applying the appropriate confidence interval from Figure 18a to any one of these curves, we observe that the correlation coefficients which were computed using larger integration times fall well within the confidence interval, except in the case of the $T^* = 0.0675$ second curve.

PROCESSES OF RADIATION INTENSITY MODULATION

Before presenting the experimental results, it is worthwhile to examine the processes by which the fluctuations in radiation intensity of the beams were produced. But to do so, we must use some of the results of the next section.

As stated previously, the original purpose of this test was to determine thermodynamic property fluctuations in the jet shear layer by first measuring the fluctuations of the absorption coefficient of oxygen and then applying appropriate calibration techniques. However, since it became apparent that other extinction processes were significant and probably dominant, this goal had to be abandoned.

The principal sources of difficulty were (1) the moisture entrained by the jets from the ambient air and (2) the low stagnation temperature. The air from the nozzles was very dry (specific humidity $\approx 10^{-6}$ to 3×10^{-6}), but the entrained water vapor provided an additional absorbing constituent in the shear layers. Also, since the jets were very cold ($T \approx -150°C$ for Mach 2.46 jet, $T \approx -190°C$ for Mach 3.34 jet) some of the water vapor undoubtedly condensed to form droplets and ice crystals which could cause radiation extinction by scattering and absorption. Likewise, appreciable amounts of carbon dioxide probably condensed in the cores of both jets. The equilibrium liquefaction points of oxygen and nitrogen were also reached, for some runs, in the core of the Mach 3.34 jet. Therefore, traces of liquid air might have occurred. In addition, small quantities of solid particles, such as dust and dryer agent, were present.

Since there were several absorbing and scattering species which could have contributed to the radiation extinction, the resultant instantaneous extinction coefficient at a point was the sum of the contributions of all species.

$$K(x, y, z, t, \lambda, \Delta\lambda, p, P, T, d, N) = K_{A_{O_2}} + K_{A_{H_2O}} + K_{S_{H_2O}} + K_{S_{CO_2}} + K_{S_{\text{Other particles}}} \tag{19}$$

The subscript A indicates absorption by a gaseous constituent, and S indicates scattering by liquid droplets or solid particles. It is recognized that liquid and solid particles can absorb as well as scatter radiation, but for the sake of compactness the term "scattering" is used loosely in this section to denote both scattering and absorption by liquid or solid particles. The extinction coefficient for a gaseous absorption process is dependent on the partial pressure, p, of the absorbing gas, the "total" pressure (sum of partial pressures), P, and temperature, T [9, Part II]. The extinction coefficient for a scattering process is primarily dependent on the diameter, d, concentration, N, and index of refraction of the scattering particles. Oxygen and water vapor are

the only constituents of air which absorb significantly at the wavelength used here, $\lambda = 1850\text{Å}$ [9, Part I]. The fluctuating component of the extinction coefficient is given by:

$$k(x,y,z,t,\lambda,\Delta\lambda,p,P,T,d,N) = K - \overline{K} = k_{A_{O_2}} + k_{A_{H_2O}} + k_{S_{H_2O}} + k_{S_{CO_2}} + k_{S_{\text{Other particles}}} \quad (20)$$

Because the concentrations of most species and the sizes of all scattering particles were unknown, it is difficult to determine which constituent dominated the resultant fluctuating extinction coefficient, k. To attempt this, we examine the measured turbulence intensity profiles. Figure 19 shows a relative intensity profile (from Fig. 23) of the Mach 3.34 jet at four nozzle diameters downstream of the nozzle. Also shown for comparison is a relative intensity profile at the same location obtained recently[1] with a laser crossed-beam system. The helium-neon lasers which were used had an optical wavelength, λ, of 6328Å (red) which is more than 3.4 times longer than the ultraviolet radiation used. It is emphasized that these intensity profiles give the intensities of the fluctuating extinction coefficient and are not necessarily the same as the fluctuating velocity intensity profile.

The laser beams were modulated entirely by "natural" scattering particles, since all gaseous constituents of the flow were transparent to this wavelength and no tracer particles were added. Because the ultraviolet beams could be modulated by either scattering or absorption but the laser beams only by scattering, it was hoped that a comparison of the two intensity profiles might reveal the extinction process which was most effective in modulating the ultraviolet beams. It was thought that the uncontrolled parameters T_t and atmospheric humidity, which determine condensation droplet and water vapor concentrations, were close enough (Fig. 19) for the two tests to permit at least qualitative comparison of the results. The mean velocity profile obtained from Pitot pressure measurements (from Fig. 38) is also shown for comparison.

The two intensity profiles are quite different, the peaks being approximately 1.3 cm apart and the uv profile being much broader than the laser profile. This difference is quite disconcerting, since it demonstrates that at least one of the crossed-beam systems did not yield a peak value at the point in the shear layer where the turbulent activity was most intense. In fact, it is the

1. The authors are grateful to Mr. B. H. Funk of MSFC for providing these previously unpublished data.

laser system which yielded a peak intensity near $y/D = 0.5$ ($\eta = 0$) where, from subsonic jet data, we expect the most intense turbulence [11, 18, 19]. The indicated peak intensity from the ultraviolet system, on the other hand, occurred in the lower velocity, outer portion of the shear layer. This is also evident from the shadowgraph in Figure 16, where the intensity profiles are plotted. Clearly, therefore, the two systems responded to different radiation extinction processes.

To explain the differences between the two intensity profiles, it is necessary to determine the fluctuating extinction processes which modulated the beams. Of course, to conduct more meaningful experiments in the future, we must be able to control the extinction process and to know which property of the turbulence field we are measuring. We first state the obvious fact that, if there is no absorbing or scattering constituent in the flow, then no signal is produced and, therefore, no turbulence is indicated no matter how intense the turbulence may actually be. Similarly, if the concentration of the absorbing or scattering species is non-uniform such that the species is sparse in the region of most intense turbulence and dense in regions of less intensity, then the peak indicated intensity will likely not occur at the point of true maximum turbulence intensity. Rather, it will occur at the point of maximum intensity of the extinction coefficient fluctuations. Therefore, it appears that non-uniformities in mean "tracer" concentrations are an important factor in the interpretation of crossed-beam measurements.

Three possible mechanisms of radiation intensity modulation in turbulent jet shear layers are discussed below:

1. Mean Gradient in Mole Fraction of the Absorbing or Scattering Species.

If the jet contains an absorbing or scattering species and the surrounding air is relatively free of that species, or vice versa, a mean gradient in mole fraction of the species is established across the turbulent shear layer. Transverse turbulent motions will then cause the displacement of relatively transparent "blobs" of fluid by relatively opaque ones and vice versa. This results in large time-varying spatial inhomogeneities in optical density which, in turn, cause large fluctuations in detected radiation intensity. Therefore, if the gradient is large, this mechanism is likely to dominate the detected signal fluctuations and produce an indicated peak in turbulence intensity in the region of maximum gradient even if the true peak in turbulence intensity occurs elsewhere. This process is illustrated in Figure 20 for a mean concentration gradient of scattering particles; however, the gradient could just as well be in an absorbing species.

2. Mean Gradients in Thermodynamic Properties.

Mean gradients in thermodynamic properties of the gas mixture can exist across the shear layer with or without gradients in mole fractions. Although the pressure is relatively uniform ($P \approx 1$ atmosphere) in jet shear layers, large gradients in temperature and density can exist. If the radiation extinction is dependent on one of these properties, fluctuations in the detected signal are created in the same manner as in case 1 above.

In the case of scattering particles, if the ratio of particle concentration to gas density is uniform and if no other extinction mechanism is present, the fluctuations in particle concentration, which produce fluctuations in the detected signal, can be related to density fluctuations of the gas. However, it would be very difficult to achieve such a uniform concentration ratio in practice, since it would be necessary to uniformly seed the surrounding atmosphere, as well as the jet.

In the case of absorption, calculations[1] using the Elsasser band model indicate that temperature fluctuations , for the experimental conditions of this report, dominate the fluctuating signal, although density fluctuations also contribute[20] . Some recent experimental data on the temperature dependence of ultraviolet radiation absorption are given in Reference 21.

3. Velocity Fluctuations

Turbulent velocity fluctuations cause thermodynamic property fluctuations whether mean gradients of those properties exist or not. Also, velocity fluctuations and vorticity cause concentration fluctuations of tracer particles. An order of magnitude estimate of pressure fluctuations can be obtained from wall pressure fluctuation measurements beneath a turbulent boundary layer where there is no mean pressure gradient. Typical rms pressures for attached boundary layers are of the order 0.005 of the stream dynamic pressure which gives rms pressures of 2 and 4 percent of atmospheric pressure for the Mach 2.46 and 3.34 jets, respectively. Corresponding fluctuations in temperature and density also occur. Figure 3b indicates that pressure fluctuations of this magnitude would produce rather small fluctuating signals for $\lambda = 1850$Å.

The relative contributions of the three processes discussed above to the detected signal depend on the conditions of the experiment. However, it is probable that if a significant gradient in mole fraction of an absorbing species exists, then type 1 predominates over types 2 and 3. In this case, it would

---

1. The authors are grateful to M. W. P. Cann of IITRI for performing these calculations.

not be possible to relate the signal fluctuations to the thermodynamic property fluctuations of the gas mixture since the signal would then be produced primarily by fluctuations in mole fraction, or partial pressure, of the absorbing gas. However, this type of modulation could be used to advantage in studies of turbulent diffusion of an absorbing gas through a transparent gas. If mean mole fraction gradients did not exist, then it would be possible to measure thermodynamic property fluctuations which result from types 2 and 3.

Unfortunately, in the experiments of this report, gradients of type 1 did exist. Since the jet core was dry and the surrounding air was moist, a mean water vapor gradient across the shear layer resulted from the mixing of dry and moist air. In addition, gradients of scattering particles were probably formed by non-uniform condensation of water vapor and carbon dioxide due to temperature and water gradients.

The probable contributors to the fluctuating signals are compared for the ultraviolet and laser beams in Table I.

TABLE I. COMPARISON OF PROBABLE RADIATION INTENSITY MODULATION PROCESSES FOR ULTRAVIOLET AND LASER BEAMS

Absorbing or Scattering Species	Probable Gradients Across Shear Layer Which Influence Extinction	Can This Species Modulate This Beam?		Possible Types of Modulation
		UV System	Laser System	
water vapor	mole fraction temperature	yes	no	1, 2, 3 (absorption)
water droplet or ice crystal	concentration	yes	yes	1, 3 (scattering and absorption)
oxygen	temperature density	yes	no	2, 3 (absorption)
carbon dioxide particles	concentration	yes	yes	1, 3 (scattering)
dryer agent and dust particles	concentration	yes	yes	1, 3 (scattering)

We shall now try to infer from Table I and Figure 19 the probable dominant process which modulated the ultraviolet beams. In interpreting Figure 19, we shall assume that the positions of the maxima in water vapor and scattering particle gradients were approximately the same for the laser and ultraviolet crossed-beam tests, although the magnitudes were probably different.

1. Since the peak in the turbulence intensity profile indicated by the uv system occurred in the outer part of the shear layer rather than near $y/D = 0.5$ ($\eta = 0$) where the maximum velocity fluctuations were expected, we conclude that the dominant modulation process probably was due to a gradient (type 1 or 2) whose maximum occurred in the outer shear layer. A type 3 modulation process would have produced a peak in the region of maximum velocity fluctuations.

2. Since the two peaks did not occur at the same location and since the laser beams were modulated only by natural tracer particles, it is probable that the uv beams were dominantly modulated by a gaseous absorption process. We might, at first, suppose that both peaks could have been caused by tracer particles, the difference in positions of the peaks being due to a distribution in particle sizes with the maximum scattering efficiencies for the laser and uv wavelength occurring at the locations of the turbulence peaks indicated by the laser and uv systems, respectively. However, further consideration shows that this is improbable.

There are indications that the particles were so small that the scattering was in the relatively weak Rayleigh range ($d << \lambda$) for both wavelengths rather than the more effective Mie range ($d \geq \lambda$). This premise is based on the facts that (1) the jets were very transparent to the eye from $x/D = 0$ to 10 or 15, and (2) the typical mean transmissions of the laser beams ($\tau^* \approx 0.8$) and uv beams were considerably higher than rough calculations, assuming predominant water droplet formation in the Mie range, indicated they should be. Therefore, since the scattering efficiency is proportional to $(d/\lambda)^4$ in the Rayleigh range, the maximum efficiency of individual drops for both wavelengths should have occurred at the position where the particles were largest. However, the maximum mean extinction coefficient due to scattering occurs where the sum of the individual droplet scattering cross sections per unit volume is a maximum. It is emphasized that the maximum rms fluctuating extinction coefficient does not necessarily occur where the mean extinction is largest, but probably occurs where the gradient in mean extinction coefficient is largest. The important observation here, however, is that in the case of Rayleigh scattering the location of the maximum rms fluctuating extinction coefficient

is independent of wavelength, although the magnitude is very much a function of wavelength. Therefore, if both ultraviolet and laser beams had been dominantly modulated by Rayleigh scattering, the peaks of the two intensity profiles should have occurred at the same place.

Even if the particles were in the Mie range for both beams, the ultraviolet peak would probably have occurred where the laser peak did ($y/D = 0.5$), if the uv beams had been dominantly modulated by scattering. For example, if the Mie scattering coefficient had been at its maximum (3.98 for water droplets) for the laser beams at $y/D = 0.5$ where the maximum rms fluctuating extinction coefficient occurred, the same particles would produce a coefficient of 2.02 for the uv beams [22]. Now, since the peak rms velocity fluctuations are assumed to occur at $y/D = 0.5$, the maximum rms fluctuating extinction coefficient for the ultraviolet wavelength should also have occurred near $y/D = 0.5$ because the maximum difference between the Mie scattering coefficients for the laser and ultraviolet wavelengths is not very large.

Figure 19 shows that the magnitude of the uv fluctuating extinction coefficient was less than that of the laser beams for $y/D < 0.55$. Assuming that the laser and uv beams were primarily modulated by Rayleigh scattering in that region, this effect could not have occurred if all conditions had been identical, except for wavelength. This effect was probably due to two factors: (1) the atmospheric humidity was greater in the laser test than in the uv test, and (2) light scattered within the cone angle (approximately 16 degrees) of the uv beams did not cause intensity fluctuations at the detector. Since forward scattering is quite large, the use of focused beams has the additional advantage of minimizing the effect of scattering particles.

3. Thus far, we have concluded that the probable dominant modulation process affecting the uv beams was due to a gradient in some property of an absorbing gas. From Table I, this gas could have been either oxygen or water vapor. In the case of oxygen, the mean temperature gradient would probably have had the dominant effect as discussed under type 2 modulation. However, the static temperature profile very nearly coincided with the mean velocity profile in Figure 19. Therefore, this effect would have produced an indicated turbulence intensity peak nearer the center of the shear layer where the maximum in the gradient of temperature occurred. Therefore, the remaining modulation process, i.e., modulation due to a mean mole fraction gradient of water vapor, appears to have been dominant. The maximum in the water vapor gradient evidently occurred in the outer shear layer rather than in the center of the shear layer where one might expect it if no condensation had occurred. The

effect of the condensation process would be to remove the water vapor which reached the inner shear layer and thus shift the water vapor profile outward.

Figure 21 shows that the mean absorption of ultraviolet radiation, at 1850Å, by the water vapor in air can be comparable to the absorption due to oxygen. Furthermore, since there was a large mole fraction gradient in water vapor across the shear layer and no gradient in oxygen, it is not at all surprising that water vapor could produce the dominant fluctuating signal. This demonstrates the effectiveness of a mean mole fraction gradient in modulating the beams.

Since the peak in the intensity profile occurred near the outer shear layer, the intermittency phenomenon undoubtedly contributed significantly to the beam modulation process. A spot at the edge of the shear layer which is momentarily filled by "fresh" ambient air with a high water vapor content is replaced a moment later by an eruption from the inner shear layer which is relatively dry, and thus the beam picks up a large "signal."

4. The relative importance of water droplets and carbon dioxide particles in modulating the laser beams could not be inferred from the data because there was no way to determine the respective sizes and concentrations of the particles.

The inferences drawn above are by no means conclusive since they are based on several assumptions, the most important being that (1) the maximum velocity fluctuations occurred at $\eta = 0$ ($y/D = 0.5$) in analogy to subsonic jets and (2) the gradients which influenced the fluctuating extinction coefficients occurred at the same locations in both the laser and uv crossed-beam tests. The later assumption is supported by the fact that two repetitions of the laser test under different humidity conditions produced turbulence intensity peaks in the same location as shown in Figure 19, although the magnitudes of the peaks varied.

Considering the tentative conclusions reached above, it was thought useless to try to interpret the data in terms of thermodynamic properties. However, it is emphasized that the uncertainties about what processes caused the beam intensity fluctuations do not prevent us from obtaining useful turbulence flow properties, as demonstrated in the next section. We merely treat all absorbing or scattering species as passive tracers which are carried about by the turbulent motion of the flow. The worst complication arises in the case of separated beams because of the possibility of change of phase from water

vapor to water droplets in any given fluid volume from the time it passes through the upstream beam until it passes through the downstream beam.

From the discussion in this section, it is clear that to measure thermodynamic property fluctuations in jets using gaseous absorption, we should (1) choose a wavelength which is absorbed by only one gas in the flow, this gas having uniform mole fraction in the jet and surrounding air, and (2) eliminate scattering particles. The first condition precludes any wavelength at which water vapor absorbs. The second condition can probably be satisfactorily met by raising the stagnation temperature to prevent condensation. However, even for ideal flow conditions, indications are that measurement of thermodynamic property fluctuations in the absence of a mean gradient in thermodynamic properties will be a formidable task because of the small fluctuating signal-to-noise ratio. Prospects are considerably brighter for flows in which large gradients in thermodynamic properties exist.

PRESENTATION OF RESULTS

The experimental data are presented and analyzed in this section. The results demonstrate the utility of the crossed-beam technique in turbulence investigations.

Intensity Profiles

Equations (3a) and (6) were used to obtain relative rms intensity profiles of the fluctuating extinction coefficient assuming constant length scales L_y and L_z at any particular axial location.

$$\sqrt{\overline{k^2(x, y, z, t)}\, L_y L_z} = \sqrt{\frac{G(x, y, z)}{\bar{I}_y \bar{I}_z}} \qquad (21)$$

Figure 22 shows relative intensity profiles at x/D of 1, 2, and 4 for the Mach 2.46 jet. However, from the discussion in the previous section, these profiles are not assumed to be indicative of the intensity profiles of any of the thermodynamic properties T, P, or ρ as originally intended, but are believed to be the intensity profiles of water vapor concentration fluctuations. Nevertheless, it was thought worthwhile to present the data because the profiles do exhibit reasonable and consistent trends, e.g., the width of the profiles increase with increasing distance from the nozzle. The reason for the increase in

$\sqrt{\overline{k^2}\, L_y L_z}$ with increasing x/D was the increase in length scales L_y and L_z (Fig. 28). The average stagnation temperature and average atmospheric temperature, pressure and relative humidity for each profile are listed on the figure since these quantities are expected to influence the results. Also, the sonic points which were determined from Pitot pressure data (Fig. 37) are marked on the figure.

Figure 23 shows similar intensity profiles at x/D of 4 and 8 for the Mach 3.34 jet. Although an intensity profile was also obtained at x/D = 1, the data were regarded as too erratic to present. Furthermore, most other testing near the nozzle exit produced erratic results. This was attributed to (1) the difficulty of accurately positioning the beam intersection point in the thin shear layer and (2) the rather weak modulation of the beams because of the small correlation volumes (or integral scales) in the thin shear layer.

Comparison of Figures 22 and 23 shows that the peak values of $\sqrt{\overline{k^2}\, L_y L_z}$ obtained at x/D = 4, the only x/D location common to the two figures, were quite close. Also, the location of these peaks ($y/D \approx 0.7$) agreed fairly well, although the tails of the profiles showed poorer agreement. The non-dimensional widths of the two curves at $\sqrt{\overline{k^2}\, L_y L_z} = 0$ also agreed reasonably well. The peaks in all curves shifted outward from the jet centerline with increasing distance from the nozzle. These peaks occurred in the outer shear layer in the region of intermittent turbulent flow as can be determined from the shadowgraphs of Figures 15 and 16.

Figure 24 gives relative intensity profiles at x/D of two and four in the Mach 2.46 jet with a coarse turbulence-producing screen (mesh = 1.6 wires/cm, wire dia = 0.16 cm) placed upstream of the nozzle throat (Fig. 11). The magnitudes of $\sqrt{\overline{k^2}\, L_y L_z}$ in the shear layer were much larger for a turbulent jet core than for a non-turbulent core flow (Fig. 22). However, the increase is largely due to increased length scales, L_y and L_z, although the magnitudes of $\sqrt{\overline{k^2}}$ also increased (Figs. 28 and 30). There was much more scatter in the data with the screen than without it. The turbulence in the jet core was not measurable at x/D = 2, but small values were measured at x/D = 4. However, the relative magnitudes of $\sqrt{\overline{k^2}\, L_y L_z}$ in the jet core and

in the shear layer are probably not indicative of the true relative magnitudes of turbulence intensity, because of the gradient in mean water vapor concentration in the shear layer as discussed in the previous section.

The data in Figures 22 through 24 were used together with the length scales, L_z, obtained in Figures 28 through 30 to calculate $\sqrt{\overline{k^2(x, y, z)}}$, assuming that the radial length scale was equal to the circumferential length scale at any point ($L_y \approx L_z$). The data for each x/D location were normalized by the maximum value observed at that x/D and plotted as a function of the non-dimensional variable η in Figures 25 through 27.

$$\eta = \frac{y - D/2}{x} \tag{22}$$

Lines of constant η are straight lines drawn from the nozzle lip at various angles to the jet axis; $\eta = 0$ corresponds to a line parallel to the jet axis.

These figures show that this method of presentation practically collapses the data from the different x/D locations to one curve as it does in the case of hot-wire data from subsonic jets [19]. One should not, however, expect data from supersonic jets run at off-design pressures to collapse in a similar fashion when plotted against η. In off-design operation the jet either billows out or contracts depending on whether the stagnation pressure is greater or less than the design pressure, and a series of expanding and contracting cells are formed in the jet [23]. The data from x/D = 1 were not included on Figure 25 because they differed markedly from the other data. This lack of agreement was probably caused, at least partially, by small inaccuracies in positioning the beams which could cause large errors in η at x/D = 1. The beams were rather difficult to position with respect to the nozzle, especially since the radiation was invisible to the eye.

Figures 25 and 26 give a non-dimensional width of the intensity profiles which is only about half that of hot-wire data from subsonic jets [19]. However, the width of the profile in Figure 27 in which the turbulence-generating screen was used is comparable to subsonic jet values. The screen also caused severe scatter in the data.

The peaks in intensity profiles occurred at large positive values of η instead of near $\eta = 0$ as they do in subsonic jets. The probable reason for this was discussed in the previous section.

Circumferential Integral Length Scales, L_z

The integral length scales, L_z, can be estimated from the data obtained in the intensity traverses by using Equation (9). The integrand of Equation (9) is plotted in Figure 28 for three axial locations (x/D = 1, 2, and 4) of the Mach 2.46 jet. The area under these curves was found numerically to obtain the length scales listed on the figure. Each length scale is equal to twice the area under the displayed curve to account for the symmetric area on the opposite side of the jet axis. Similar results for the Mach 3.34 jet are shown in Figure 29.

The primary source of error in this method is probably the light source and detector noise included in $\overline{i_y^2}$. However, since the noise was not excessively large in these experiments, no correction for noise was attempted.

It should be emphasized that,as a result of the tentative conclusions reached in the Section on Process of Radiation Intensity Modulation, the length scales obtained here are thought to be primarily a measure of the distance over which water vapor concentration fluctuations were correlated. These length scales need not be the same as those which would have been obtained from velocity fluctuation measurements. For example, the existence of different length scales for different fluctuating quantities (temperature and velocity) of a turbulent field was demonstrated theoretically for isotropic turbulence in reference 25 and experimentally for shear flow turbulence in reference 26. The change of phase from water vapor to water droplets probably influenced the length scales measured in the crossed-beam experiments in a way somewhat analogous to the influence of heat conduction on temperature length scales.

The length scales for the Mach 2.46 jet with turbulence-producing screen were obtained in Figure 30. According to these results, the presence of the screen approximately doubled the length scale.

Figure 31a shows the circumferential length scales, L_z, obtained in Figures 28 through 30 plotted as a function of distance from the nozzle exit. This figure shows that the length scales increase at about the same linear rate with distance, except when the screen is installed, irrespective of nozzle diameter or Mach number. Also shown for comparison is the radial, or lateral, length scale, L_y, obtained by Laurence [11] from hot-wire measurement in subsonic jets. Laurence's length scales were doubled before plotting

on Figure 31a to conform to the definition used in this report (see Section on Crossed-Beam Correlation Technique). The circumferential scales, L_z, measured with the screen installed are fairly close to the radial subsonic scales, L_y. However, the scales measured without the screen are considerably smaller than the subsonic shear layer values. Although the length scales obtained by the crossed-beams and hot-wires were measures of the correlation distances of two different quantities, it seems probable that the main reason for the differences in length scales was the differences in the two flow fields, primarily in shear layer thickness. The supersonic jet shear layers were much thinner than the subsonic shear layers as shown below.

The shear layer widths, W, determined by two different methods are plotted in Figure 31b as a function of distance from the nozzle exit. The open symbols were obtained from the mean velocity profiles and the filled symbols from the crossed-beam intensity profiles (Figures 22 through 24). The shear layer width from a mean velocity profile was defined as the distance between the two points where $U/U_e = 0.99$ and $U/U_e = 0.01$. The shear layer width from a turbulence intensity profile was defined as the distance between the two points where $\sqrt{\overline{k^2} L_y L_z} = 0$, as determined by a projection of the "best fit" curve. The mean velocity data gave two distinct straight lines for the two different Mach numbers. However, the crossed-beam data, without screen, nearly gave a single straight line. The uv crossed-beam intensity profiles indicated somewhat wider shear layers than the mean velocity profiles indicated. Furthermore, as illustrated in Figure 19, the shear layer indicated by the ultraviolet crossed-beam profiles was displaced outward from the jet centerline relative to the shear layer indicated by the velocity profiles. The two points obtained from crossed-beam data with the screen installed show a marked increase in shear layer width due to the presence of the screen. Unfortunately, no Pitot pressure data were obtained with the screen installed. The dashed line shows the shear layer thickness of a subsonic jet obtained from the velocity profiles of Reference 11.

Figure 32 shows the length scales of Figure 31a plotted against shear layer thicknesses obtained from Figure 31b. Two shear layer widths were used for each length scale, except for the two points obtained with the screen installed. The shear layer widths obtained from mean velocity profiles for the appropriate jet were used to obtain the open symbols. The closed symbols resulted from using the straight line fit of all the points from the crossed-beam intensity profiles. The two points from the jet with screen were plotted against the shear layer thicknesses indicated by the crossed-beam intensity profiles for that jet. The dashed line is the radial length scales, L_y, obtained by Laurence for subsonic jets.

Figure 32 suggests that the integral scales, L_y and L_z, from subsonic and supersonic jets, with or without turbulent core flow, can almost be made to coincide, at least for a considerable distance downstream of the nozzle, when they are plotted against shear layer thickness. The ratio of shear layer thickness to integral scale is about 3.

Space-Time Correlations

The space-time correlation curves are presented in Figures 33 through 36. Equation (7) could have been used to plot the estimated two-point correlation coefficients. However, all the required information can be obtained from two-beam correlation coefficients which are somewhat more informative since they reveal the magnitudes of the correlation coefficients obtained by the crossed-beam method. The two-beam correlation coefficient is defined below:

$$R_B(\xi,\tau) \equiv \frac{\overline{i_y(t+\tau)\, i_z(t)}}{\sqrt{\overline{i_y^2(t)}\;\overline{i_z^2(t)}}} = \frac{G(x+\xi, y, z, \tau)}{\sqrt{\overline{i_y^2(t)}\;\overline{i_z^2(t)}}} \qquad (23)$$

Figure 33 gives the two-beam correlation coefficient curves for the Mach 2.46 jet at x/D = 2. Parts (a) through (e) of this figure correspond to different y/D locations. Each different curve corresponds to a different beam separation, ξ, which is noted on the figure. Similar curves are presented in Figure 34 at x/D = 4 for the Mach 2.46 jet. Figures 35 and 36 present the curves obtained at x/D of 4 and 8, respectively, for the Mach 3.34 jet. The maxima of these curves, which occur at successively larger time-delay values as the beam separation increases, clearly indicate the presence of convected turbulence (to be discussed later). The average confidence interval (degree of confidence = 0.95) is shown on each curve.

The peaks in the $R_B(\xi, \tau)$ curves for zero beam separation, $\xi = 0$, were usually displaced from the $\tau = 0$ axis, contrary to expectations. This effect could have been caused either by errors in intersecting the beams or by a static phase displacement between data acquisition channels. However, it is believed that neither of these possible errors was large enough to account for the observed effect since it would require errors in beam displacement up to 0.6 cm or errors in time displacement up to 50 microseconds (180 degree phase shift at 10 KC). Although the beams were rather difficult to align because the radiation was invisible, it is believed that the errors were always less than 0.2 cm. Therefore, the peak displacement appears to be primarily an unexplained effect of the crossed-beam technique.

Since the correlations for the turbulence intensity profiles (Figs. 22 through 24) were measured only for $\tau = 0$ using the analog correlator online, the maximum values of the correlations were not obtained in those cases for which the peaks were displaced from $\tau = 0$. The solid symbols on Figure 23 for $x/D = 4$ were obtained using the maximum correlations, rather than the values at $\tau = 0$, from the digitally computed space-time correlations for zero beam separation (Fig. 35). The curve formed by these points has basically the same shape, but is displaced upward from the one obtained from the analog correlator data.

Because the curves of $R_B(\xi, \tau)$ which were obtained at x/D of 2 and 4 for the Mach 2.46 jet with the turbulence-generating screen in place were more difficult to interpret than the above data, they were not presented. The presence of the screen had a rather marked effect on the $R_B(\xi,\tau)$ curves, particularly in producing large narrow-band components. However, it was thought that a more thorough study of the effect of the screen should be made before presenting any data.

Convection Speeds and Mean Velocity Profiles

The convection speed of the turbulence can be found by determining the time it takes coherent turbulence patterns, or eddies, to travel from the upstream beam to the downstream beam when the beams are separated a known distance along the stream direction. This time, τ_P, is determined from the space-time correlation curves as the time lag at which the peak correlation occurs.

$$U_c = \frac{\xi}{\tau_P} \tag{24}$$

To obtain acceptable accuracy, several beam separations were used and the results averaged. This is done in the insets on Figures 33 through 36 by plotting ξ versus τ_P and taking the slope of the best straight-line fit through these points. By taking the convection speed as the slope of this line rather than an average U_c obtained from Equation (24), the shifts in the peaks are accounted for. The peak shift appears to have occurred rather systematically for all beam separations because the best straight-line fit of all the other points usually went through the $\xi = 0$ point. The convection speed thus obtained and the ratio of this speed to the nozzle exit velocity are listed on each figure. The convection speed decreased with increasing distance from the jet axis as expected.

An alternate definition of convection speed, which is sometimes used [24], is based on the time delay, τ_T, for which the envelope of all space-time correlation curves is tangent to the curve for a particular beam separation.

$$U_{c_T} = \frac{\xi}{\tau_T} \tag{25}$$

The two convection speeds are distinguished by the subscripts P and T for the "peak" and "tangency," or "envelope," methods, respectively. The envelope method is thought to yield the more significant convection speed. However, because only a small number of curves was obtained for each y/D location and, also, the peaks did not consistently decay with increasing beam separation, it was difficult to draw an envelope and find the tangency points. For those cases in which this could reasonably be done, U_{c_T} was determined and listed on Figures 33 through 36. The value of U_{c_T} was always slightly less than U_{c_P}.

The reason for the irregular decay in the peaks of the space-time curves is not known. The confidence intervals computed for these curves indicate that the "scatter" does not fall within the computation error. This effect might be related to the possible phase change of water vapor discussed in the Section on Processes of Radiation Intensity Modulation.

Figure 35a is interesting because it shows a double peak in three of the space-time correlation curves. The first of these peaks for each curve, denoted by P_1, falls on the same straight line in the inset with the three single peaks. The second peak, P_2, for the three curves gives a slightly smaller convection speed, U_{c_2}. The reason for the double peak and why the double peak did not occur in all curves is unknown. It should be noted, however, that the correlation coefficients in this figure are very small.

The ratio of convection speed to nozzle exit velocity is plotted as a function of distance from the nozzle centerline in Figure 37 for the Mach 2.46 jet and in Figure 38 for the Mach 3.34 jet. The mean velocity profiles were also plotted in these figures. These curves exhibit the same trends which have been observed in subsonic jets; i.e., U_c is less than U at the inner shear layer and greater than U in the outer shear layer [19]. The sonic points are shown on each velocity profile.

The mean velocity profiles were obtained from the Pitot pressure data by finding the local Mach number and speed of sound. The Mach number was determined in the supersonic part of the shear layer by using the Rayleigh Pitot formula and assuming that static pressure was equal to atmospheric pressure. In the subsonic part of the shear layer, the isentropic relation

$$\frac{P}{P_t} = \left[1 + \frac{\gamma - 1}{2} M^2\right]^{\frac{\gamma}{\gamma - 1}} \qquad (26)$$

was used to find Mach number. The local speed of sound was determined assuming a linear variation in mean stagnation temperature across the shear layer from atmospheric, T_a, at the outer edge to T_t of the jet core at the inner edge. Any deviation from a linear variation of T_t produced only small errors because there was at most 30° C difference between T_a and T_t of the jet core. Much larger errors were probably introduced by the effect of turbulence on the measured Pitot pressures [12], especially in the outer layer where the flow was intermittent, and by using isentropic relations for viscous, turbulent flow.

The convection speeds from Figures 37 and 38 are plotted as a function of η in Figure 39. Again, the open symbols denote the convection speeds determined by the peak method, and the filled symbols were obtained by the envelope method. The data collapsed to a single curve, within experimental scatter, indicating convection speed profiles similar to those found for subsonic jets [19].

Also shown for comparison in Figure 39 is the convection speed profile for a subsonic jet [19] and the mean velocity data from Figure 37 and 38. Since the mean velocity data formed a fairly smooth curve when plotted against η, only the "best-fit" curve was plotted. The variation of U_c/U_e with η in the supersonic jets was much greater than in the subsonic jet, at least in the central part of the shear layer, following the same trend as the mean velocity profiles. All fluctuating quantities, which produce the measured signals, in a given turbulent field are expected to be convected downstream at approximately the same speed; therefore, the differences in U_c/U_e between the subsonic and supersonic jets are believed to be caused primarily by the differences in flow fields rather than differences in measuring techniques. If a new definition of η based on the shear layer thickness $\eta' = \frac{y - D/2}{W}$ is used, the convection speed curves from subsonic and supersonic jets are brought much closer together; thus, it appears that η' would be a more suitable nondimensional variable to unify the results from subsonic and supersonic jets.

Moving – Axes Time Scales

The majority of the space-time correlation curves presented in Figures 33 through 36 show a decrease in the peak values of successive curves as the beam separation increases. This demonstrates that turbulence patterns are distorted during passage between the two beams. It has become common to measure the rate of distortion by defining a moving-axes time scale, L_τ, as the time delay for which the envelope of a series of space-time correlation curves falls to 1/e of its initial value ($\tau = \xi = 0$). Values of L_τ determined from Figures 33 through 36 are presented in Table II.

TABLE II. ESTIMATES OF MOVING-AXIS TIME SCALES, L_τ

Mach No.	x/D	y/D	η	L_τ (μ secs)	$U_c L_\tau$ (cm)	$U_c L_\tau/x$
2.46	2	0.514	0.007	147	5.10	0.344
		0.548	0.024	165	3.96	0.267
		0.582	0.041	157	3.14	0.212
		0.652	0.076	185	3.18	0.214
	4	0.514	0.003	207	7.51	0.262
		0.616	0.029	245	6.49	0.226
		0.754	0.063	277	5.07	0.177
3.34	4	0.605	0.026	173	4.00	0.183
		0.698	0.049	225	4.50	0.206
		0.790	0.072	247	4.62	0.211
	8	0.650	0.019	270	7.37	0.172
		0.744	0.031	445	12.06	0.282
		0.837	0.042	360	8.35	0.195
		0.930	0.054	335	6.23	0.146
		1.115	0.077	480	7.77	0.182

Table II contains fifteen estimates of L_τ from the twenty graphs in Figure 33 through 36. Since it was difficult to draw envelopes to some of these curves, the worst cases were eliminated. Figures 34a and 34e were eliminated because they showed virtually no decrease in the peak values. Figures 33a,

35a and 35e were eliminated because the peaks were too scattered. The table indicates a trend for L_τ to increase with increasing distance from the jet axis, although this trend is violated several times.

The distance traveled by the turbulence pattern during its decay period is also of interest. This distance, also shown in Table II, is given by the product of the moving-axes time scale with the local convection speed.

To compare all the results from the two nozzles at the different axial locations, the dimensionless variable $U_c L_\tau/x$ was used. It was thought that this variable might reduce all of the data to a single curve when plotted against η because of two facts known from hot-wire measurements in subsonic jets.

1. L_τ is inversely proportional to the nozzle exit velocity so that for a given location the product $U_c L_\tau$ is practically independent of U_e.

2. L_τ increases linearly with distance from the nozzle.

Figure 40 shows $U_c L_\tau/x$ plotted as a function η. Although the data are scattered considerably, one feature is apparent; i.e., there is a minimum in the curve near $\eta = 0.05$ which is the location of the peaks in the intensity profiles (Figs. 25 and 26). The values of $U_c L_\tau/x$ are somewhat less than those obtained by hot-wire measurements in subsonic jets [19]. This fact indicates that the rate of distortion of turbulence patterns in supersonic jet shear layers is greater than in subsonic jets. Since the velocity gradient, $\partial U/\partial y$, is much greater in these jets than in subsonic jets, the above result does appear to be in qualitative agreement with the results of Reference 19; i.e., the moving-axes time scale is inversely proportional to $\partial U/\partial y$.

Spectra

The spectra of the individual signals, $i_y(t)$ and $i_z(t)$, from the two beams and also the local spectra obtained from the two-beam correlations, $\overline{i_y(t+\tau)\, i_z(t)}$, are presented in this section. A typical example of the spectral energy distributions of the two signals from the individual beams is shown in Figure 41 for the beams intersected at $x/D = 4$, $y/D = 0.698$ in the Mach 3.34 jet. A one-third-octave spectrum analyzer was used to obtain these results. It is emphasized that the signals from which these data were obtained

result from an integral of the fluctuations all along the beams. The two beams yielded very similar spectral density curves, although they traversed different paths. The magnitudes of these spectra decay with the $-\frac{5}{3}$ power of frequency at high frequencies, a behavior which is characteristic of hot wire measurements in subsonic flows, e. g., reference 11.

The crossed-beam power spectra were obtained by computing the integral of Equation (18) using the digital data analysis program described in the Section on Data Reduction. Two precautions were taken to assure reasonable accuracy in the power spectra computation: (1) A long integration time ($T^* \approx 1^{\wedge}$ sec) was used to obtain small confidence intervals (about 0.010 to 0.016) in the cross-correlation coefficients, and (2) only those zero beam separation runs were used for which $R_B(\xi = 0, \tau = 0) > 0.12$.

Figure 42a shows a typical two-beam correlation coefficient curve for zero beam separation ($\xi = 0$). The peak of this curve is displaced from $\tau = 0$, and the curve is not symmetric either about $\tau = 0$ or about the τ corresponding to the peak, as would be the case for a true auto-correlation of a point probe measurement. It is believed that this asymmetry is a characteristic of the crossed-beam technique and might be a measure for the asymmetry of the correlation volumes passing through the beam intersection point.

Figure 42b is the normalized co-spectrum obtained by Fourier-transforming the curve in Figure 42a. The absolute values of the spectral density have no physical significance since we were unable to relate our signals to physical quantities. The peak in $R_B(0, \tau)$ was shifted to $\tau = 0$ before performing the calculation. It was found that the shape of the spectral density curve was very sensitive to the magnitude of the confidence interval. For example, by increasing the confidence interval from 0.012 to 0.020, the co-spectrum went from a smooth curve such as shown in Figure 42b to a very irregular curve with relatively large negative values at some frequencies. Because of the asymmetry of the $R_B(0, \tau)$ curve, relatively large values of quad-spectra were also obtained. To determine the effect of this asymmetry on the co-spectrum curve, $R_B(0, \tau)$ was Fourier-transformed, after shifting the peak to $\tau = 0$, using only positive values of τ, assuming symmetry about the $\tau = 0$ axis, and truncating at $\tau = 0.001$ second. Figure 42b shows that these results agreed very well, for frequencies lower than 4000 cps, with the curve obtained by the previous method.

The frequency corresponding to the peak in the crossed-beam spectra, f_p, is shown on Figure 41. The crossed-beam and single beam spectra were obtained from the same run. The peaks in the two types of spectra occur at approximately the same frequency.

Figure 43 shows all the co-spectra data plotted as a function of the Strouhal number defined below.

$$S_x = \frac{f x}{U_c} \quad . \tag{27}$$

The curves for all beam intersection positions are similar; however, there is considerable scatter in the data. It is not known, at this time, whether this scatter is due entirely to errors in determination of the spectral density and U_c, or to the fact that the Strouhal number defined above is an insufficient similarity parameter to collapse all the data.

Comparison of Figures 41 and 43 indicates that at high frequencies the magnitude of the crossed-beam spectra falls off with increasing frequency at a considerably greater rate than do the single-beam spectra. The average slope of the spectral density curves in Figure 43 is about -3.0, although there is considerable variation about this slope. This greater slope at high frequencies is expected for three-dimensional spectra [12, p. 226] in the special case of isotropic turbulence. The relation obtained from Hinze is given below:

$$E(\kappa) = \frac{1}{4\pi\kappa} \frac{dE_1(\kappa)}{d\kappa} \tag{28}$$

The function $E(\kappa)$ is equivalent to Hinze's function, $E_{\gamma,\gamma}$ and $E_1(\kappa)$ is the one-dimensional spectrum function called $E_{\gamma,1}$ by Hinze. See Equation (11) for definition of $E(\kappa)$. The function $E(\kappa)$ should not be confused with Hinze's three-dimensional spectrum function $E_\gamma(\kappa)$ which is an integral of $E_{\gamma,\gamma}$ around a sphere in wave number space.

If E_1 has a slope of -5/3 at high frequencies, Equation (28) gives a slope of -11/3 for $E(\kappa)$, which is not too much different from the slope of -3 obtained in Figure 43. However, equation (28) holds only for isotropic turbulence, so we do not know what the slope should be for the anisotropic shear layer flow of this experiment. Nevertheless, it seems probable from the derivation of equation (28) that in the case of anisotropic turbulence $E(\kappa)$ should still have a larger negative slope, at large κ, than $E_1(\kappa)$. Therefore, the fact that the slope in Figure 43 is considerably greater than $-\frac{5}{3}$ is an indication that the crossed-beam technique might yield three-dimensional spectra as suggested by the analysis in the Section on The Crossed-Beam Correlation Technique. However, since the capability of the crossed-beam technique to measure three-dimensional spectra has not been conclusively demonstrated at this time, further interpretation of the spectral data presented here is unwarranted. Until further confirmation is obtained, it appears advisable to regard these data as just "crossed-beam spectra." To determine whether or not the crossed-beam technique does, in fact, measure three-dimensional spectra, one should measure crossed-beam spectra and one-dimensional spectra in an isotropic flow field to see if equation (28) is obeyed. The possibility of measuring three-dimensional spectra directly is one of the most attractive features of the crossed-beam technique.

Streamwise Length Scale

The streamwise, or longitudinal, length scale, L_x, can be found from Equation (8). However, since it takes a large number of measurements to obtain a length scale by this method, this approach was not used. Alternatively, one could use the convective flow approximation of Equation (15) to obtain the following relation:

$$L_x = \frac{U_c}{R_B(0,0)} \int_{-\infty}^{\infty} R_B(\xi = 0, \tau)\, d\tau \quad . \tag{29}$$

However, since the two-beam correlation curves in Figures 33 through 36 had a relatively large negative area which, in most cases, was nearly as large as the positive area, it was decided not to use the above relation but to use the following alternative length scale definition based on the spectral density curve presented previously:

$$L_x = \frac{U_c}{\pi f_P} \quad . \tag{30}$$

The quantity f_P is the frequency corresponding to the peak in the spectral density curve. The length scales for both jets are plotted as a function of shear layer thickness in Figure 44. Each point on this figure is an average of several L_x's across the shear layer (in the y direction) for that particular x/D location. The variations in L_x across the shear layer were fairly small and were without consistent trends, so this approach was thought to be reasonable. These data give a nearly linear variation with shear layer thickness, the ratio of length scale to shear layer thickness being about 1.2.

Also shown for comparison in Figure 44 are the streamwise integral length scales of a subsonic jet determined from the hot-wire measurements of Reference 19 and using the subsonic shear layer thickness data from Figure 31. An integral definition analogous to Equation (8), but not including the negative area under the space correlation curve, was used to compute L_x. The values from Reference 19 were doubled to conform to the length scale definitions used in this report; i.e., the correlation lengths are chosen to extend in the negative as well as positive direction. The subsonic and supersonic length scales agree quite well; however, the equivalence of the length scale definitions used in the two cases has not been shown. Also, the subsonic and supersonic length scales are measures of the correlation distances of different quantities as discussed in the section on L_z.

CONCLUSIONS

The major results from the first crossed-beam investigation of the turbulence characteristics of shock-free, supersonic jet shear layers are summarized below:

1. The success of these measurements demonstrated the usefulness of the crossed-beam technique for turbulence investigations in supersonic flow.

2. The crossed-beam technique shows promise of yielding three-dimensional spectra from a single measurement.

3. It was tentatively concluded that the radiation intensity of the beams in this experiment was predominantly modulated by water vapor concentration fluctuations which resulted from a large time-average gradient, across the shear layer, in the mole fraction of water vapor. This effect prevented the measurement of fluctuations in the thermodynamic properties P, T, and ρ by means of the absorption characteristics of oxygen.

4. A considerable degree of similarity exists between the turbulence properties of subsonic and supersonic jet shear layers when the supersonic jet is free of shocks, i. e. , operated at its design pressure. This similarity was found although the crossed-beam measurements in supersonic jets were believed to be primarily sensitive to water vapor concentration fluctuations and the hot-wire measurements in subsonic jets were sensitive to velocity fluctuations. The crossed-beam results for supersonic jets and published hot-wire data for subsonic jets are compared below:

a. The convection speed and intensity profiles of both subsonic and supersonic jets show self-similarity, at each Mach number, when plotted against the nondimensional variable η . Furthermore, a new nondimensional variable,

$$\eta' = \frac{y - D/2}{W}$$

which is based on the shear layer thickness instead of distance from the nozzle, can be used to bring the data from different Mach number jets much closer together.

b. The lateral and streamwise length scales and the shear layer thickness, for each Mach number, increase linearly with distance from the nozzle exit. The streamwise length scales, L_x , are roughly equal to the shear layer thickness, and the length scales L_y and L_z are roughly one-third of the shear layer thickness in both subsonic and supersonic jets. However, the shear layer thickness decreases with increasing Mach number.

5. The presence of a coarse, turbulence-generating screen just upstream of the nozzle throat produced remarkable effects on the shear layer characteristics including:

a. doubling the circumferential length scale, L_z,

b. approximately doubling the width of the intensity profiles, and

c. introducing narrow band components in the correlation coefficient curves (not shown in this report).

George C. Marshall Space Flight Center
National Aeronautics and Space Administration
Marshall Space Flight Center, Alabama 35812
933-50-07-01-62 July 1968

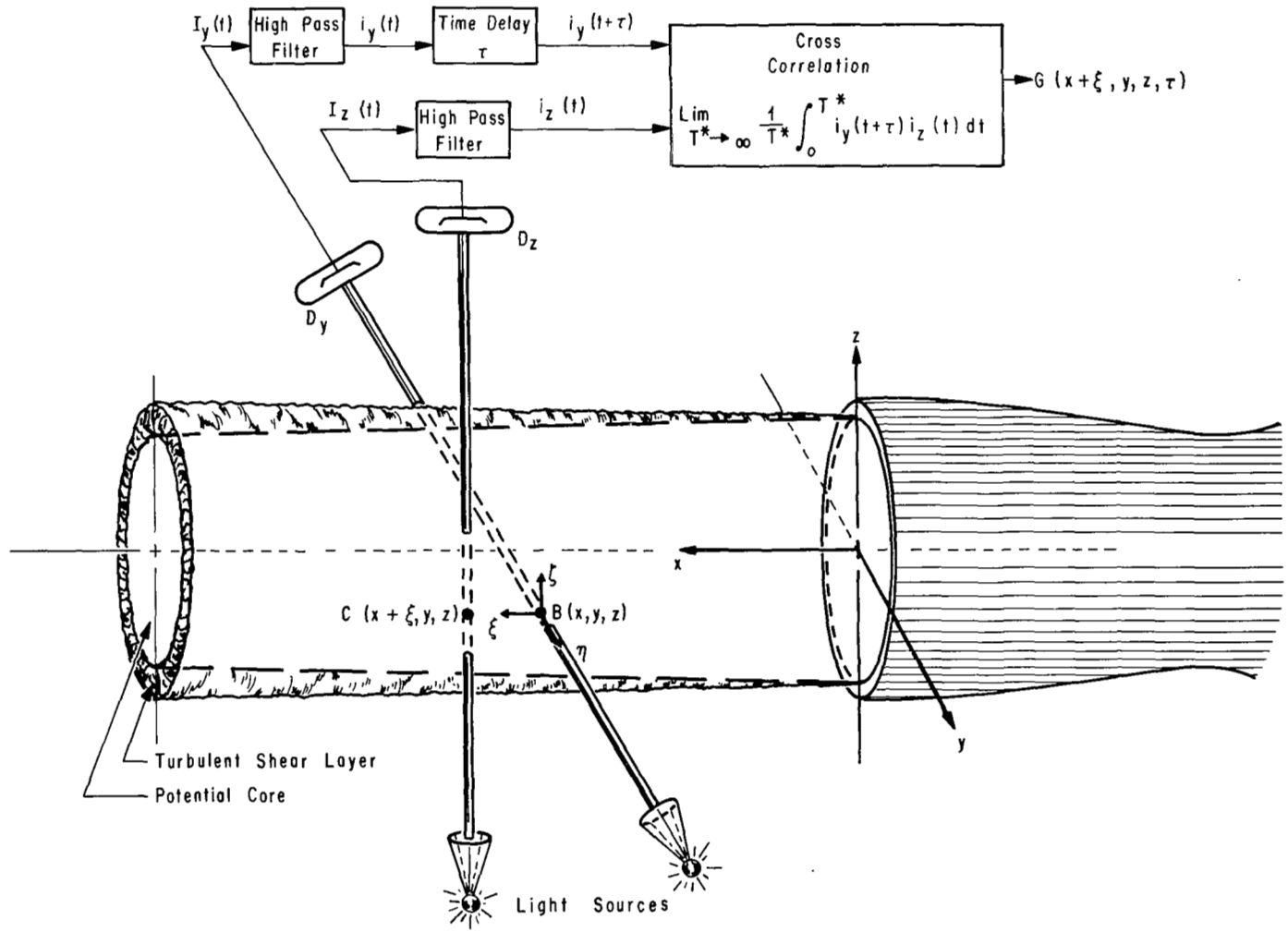

FIGURE 1. SCHEMATIC DIAGRAM OF CROSSED-BEAM OPERATION IN A JET

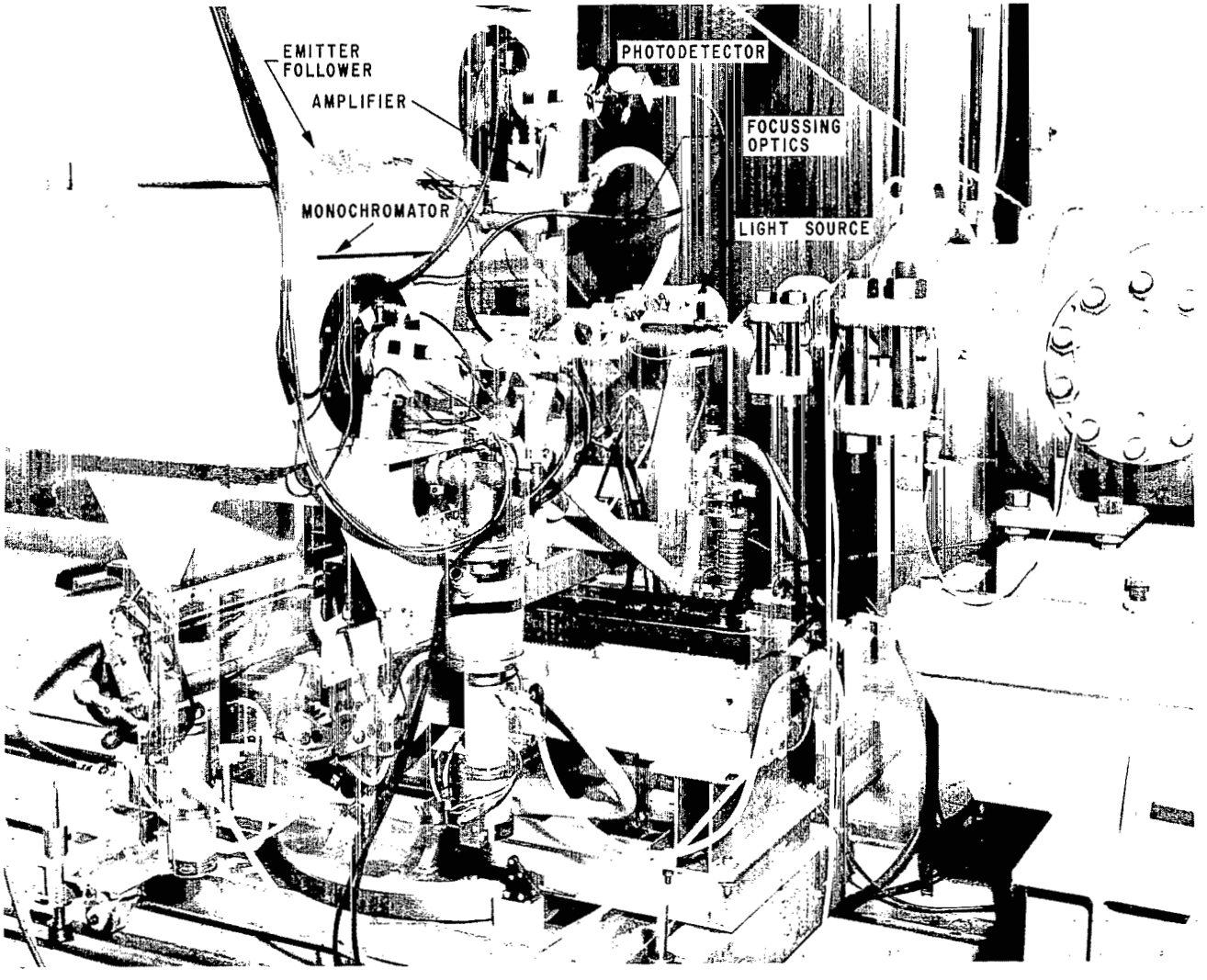

FIGURE 2. THE CROSSED-BEAM APPARATUS

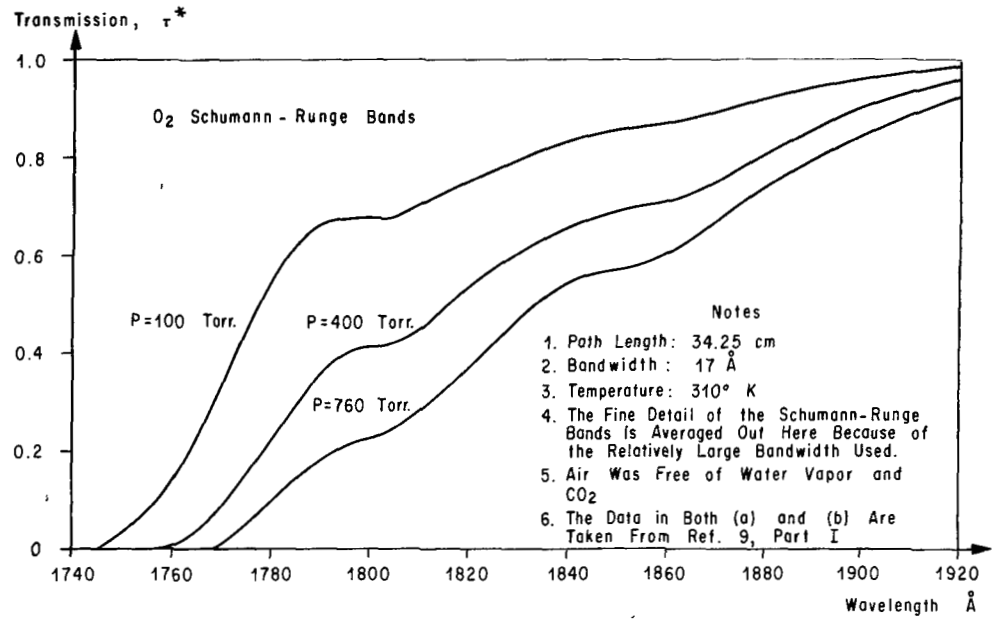

(a) Transmission As Function of Wavelength (Constant Pressure And Temperature)

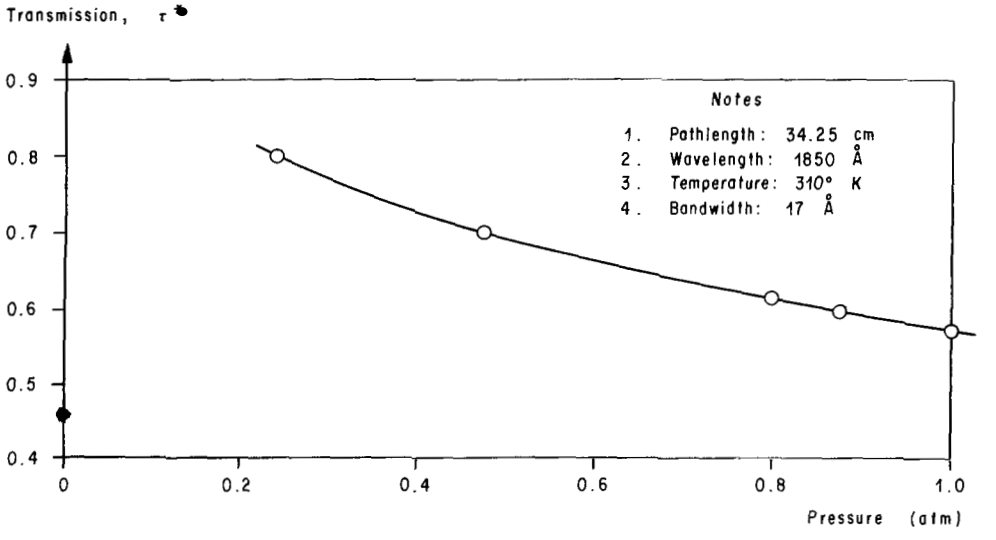

(b) Transmission As Function of Pressure (Constant Wavelength And Temperature)

FIGURE 3. MEASURED TRANSMISSION OF ULTRAVIOLET RADIATION THROUGH AIR

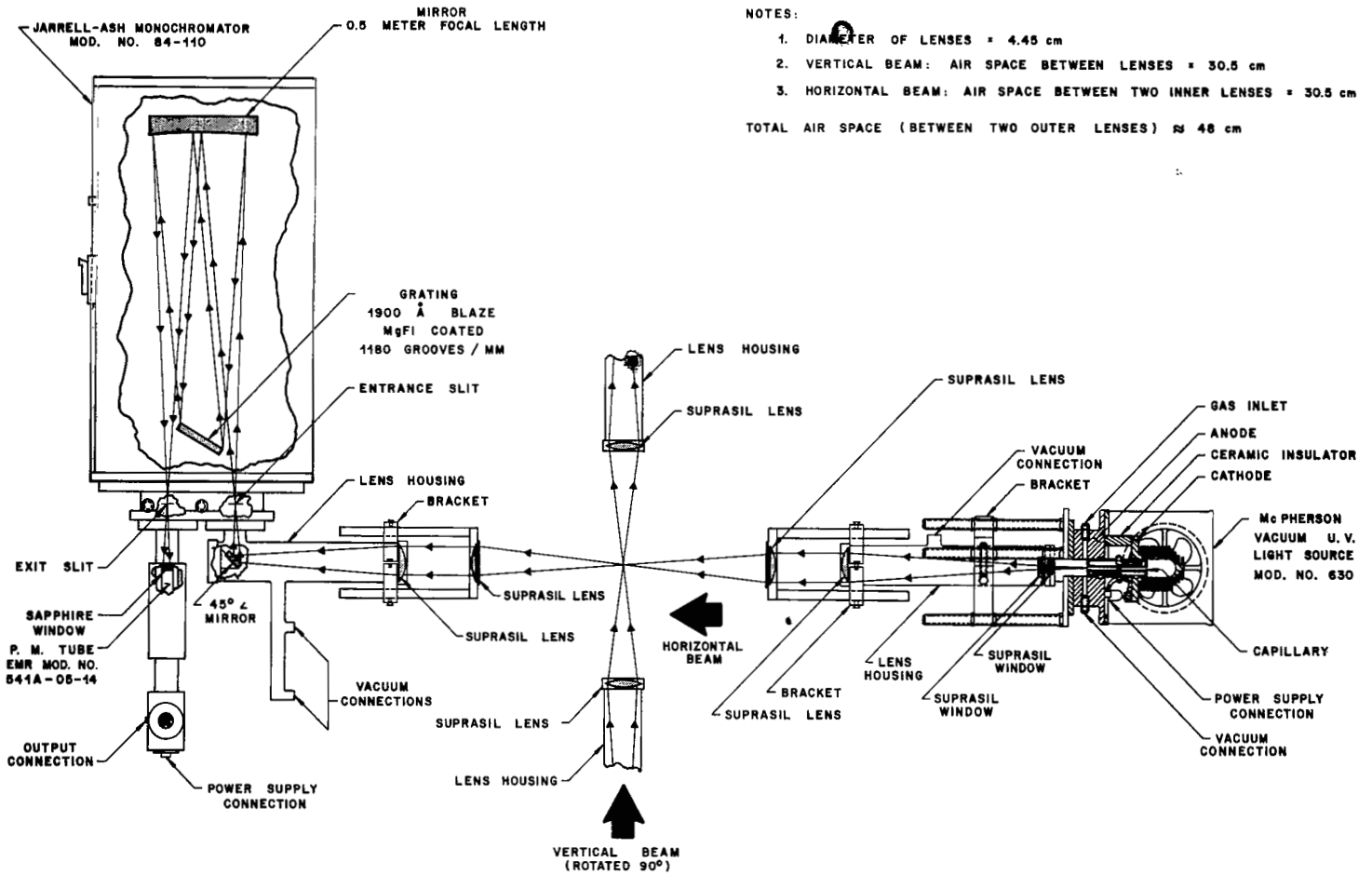

FIGURE 4. FOCUSSED-BEAM OPTICAL SYSTEM (Top View)

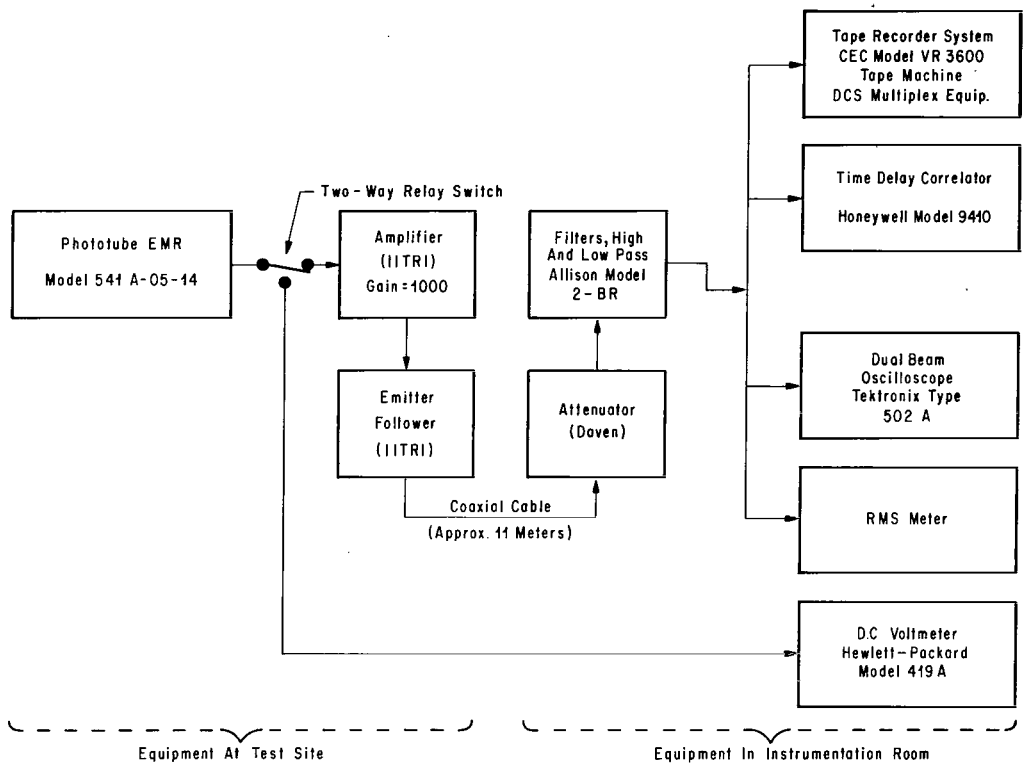

A. Data Acquisition Chain

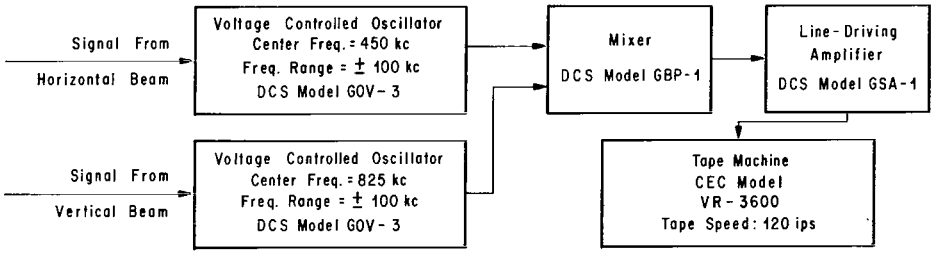

B. Multiplex Tape Recorder System

FIGURE 5. DATA ACQUISITION SYSTEM

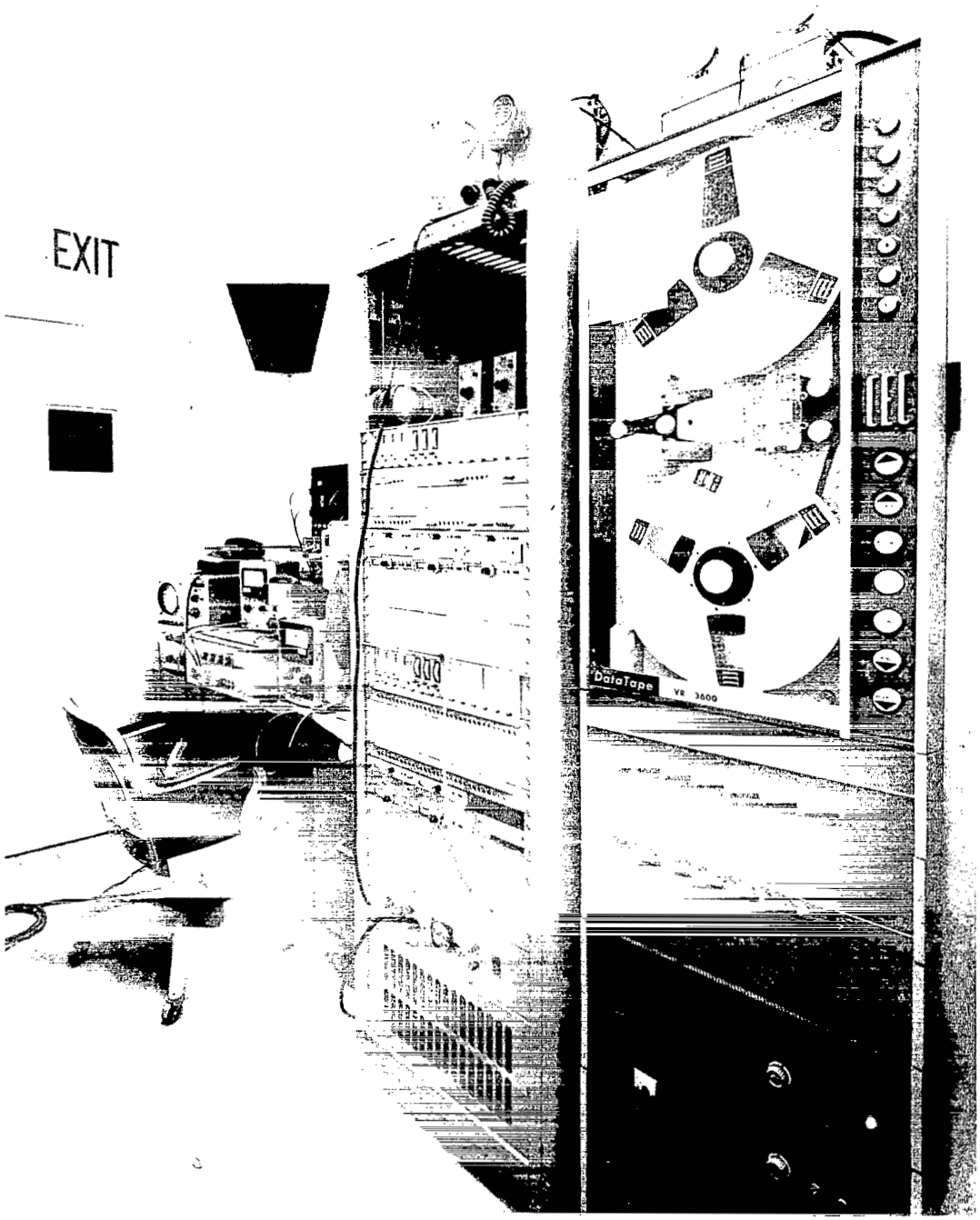

FIGURE 6. DATA ACQUISITION EQUIPMENT IN INSTRUMENTATION ROOM

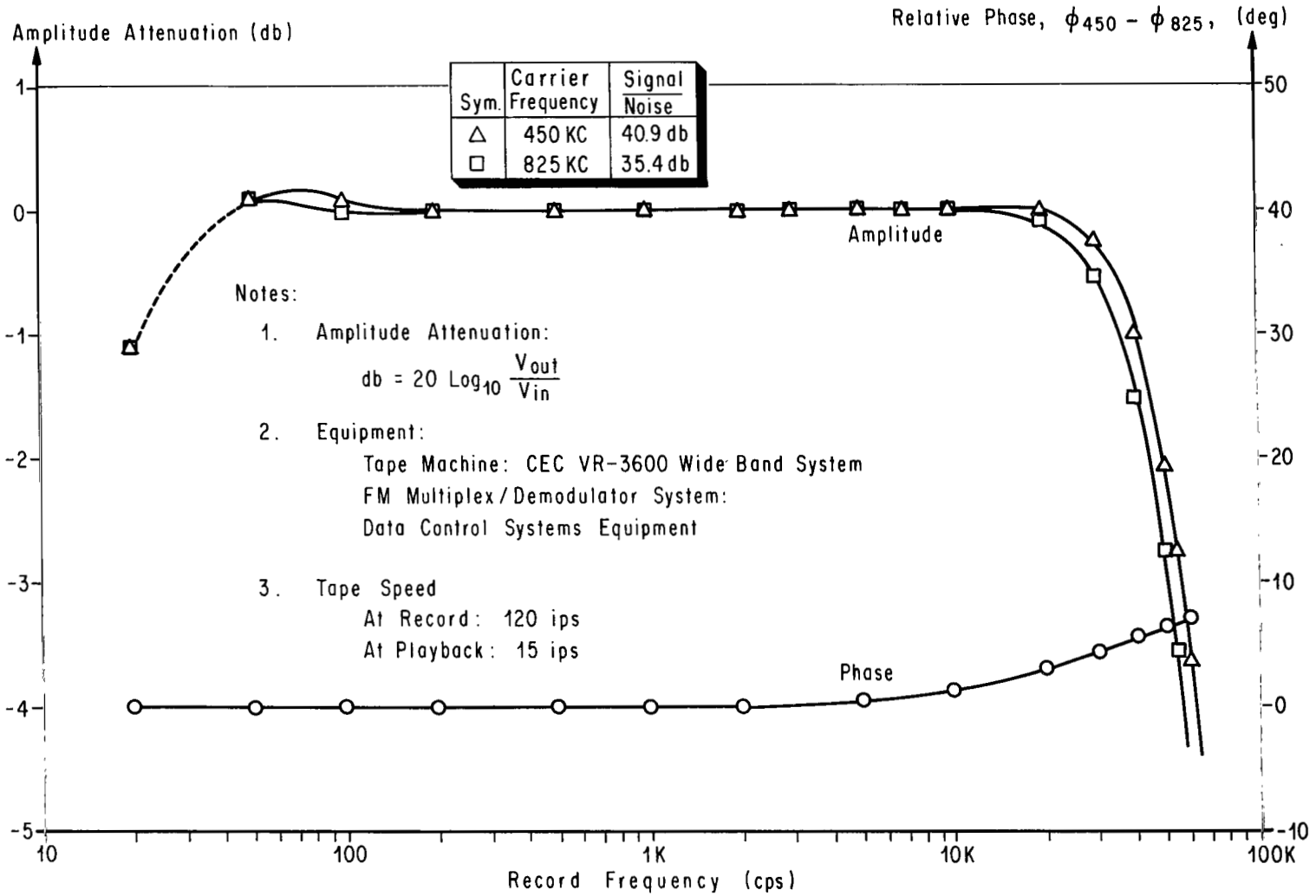

FIGURE 7. FREQUENCY RESPONSE OF TAPE RECORDER SYSTEM

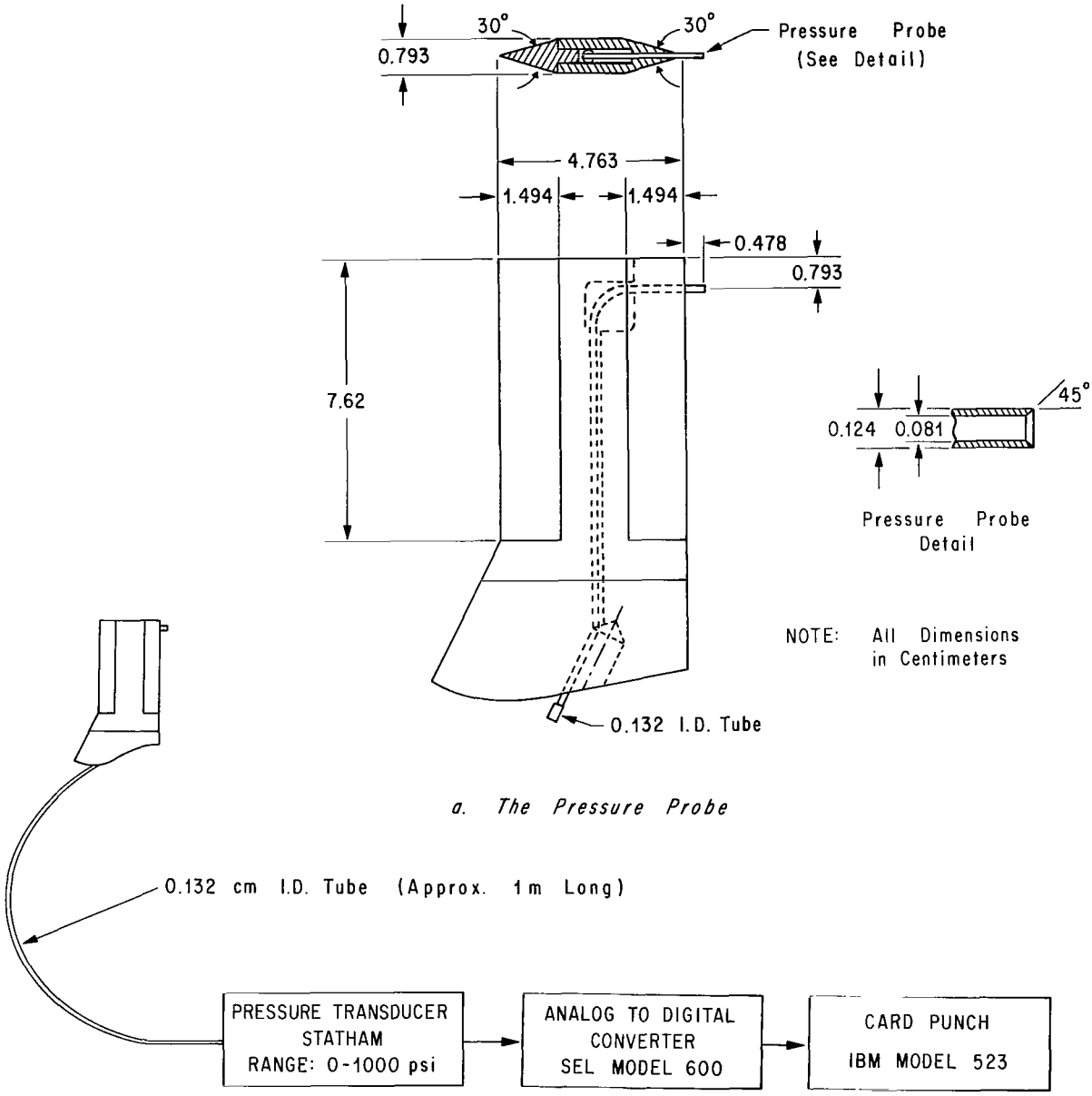

a. The Pressure Probe

b. Data Acquisition Chain

FIGURE 8. THE PITOT PRESSURE PROBE SYSTEM

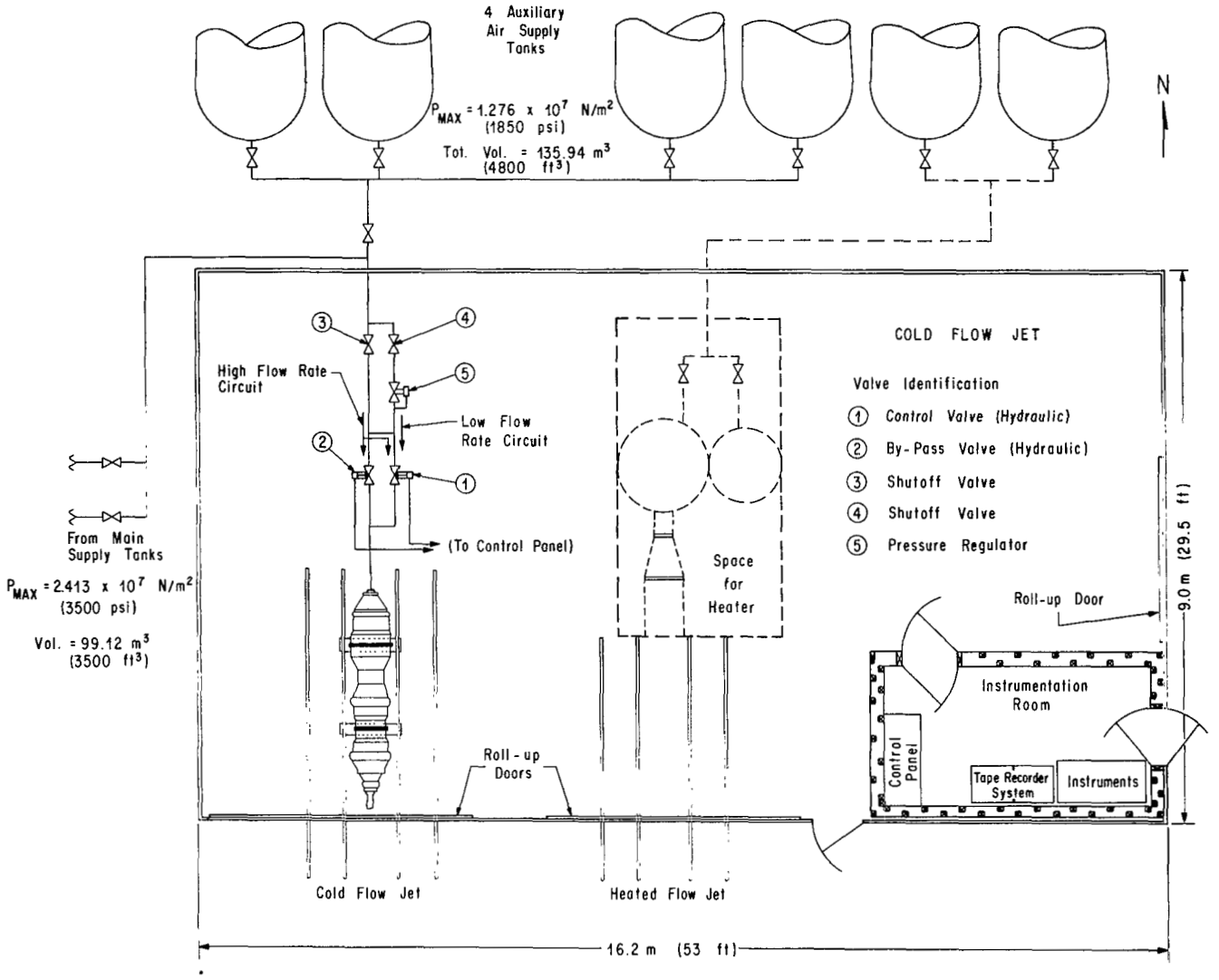

FIGURE 9. THERMO-ACOUSTIC JET FACILITY LAYOUT

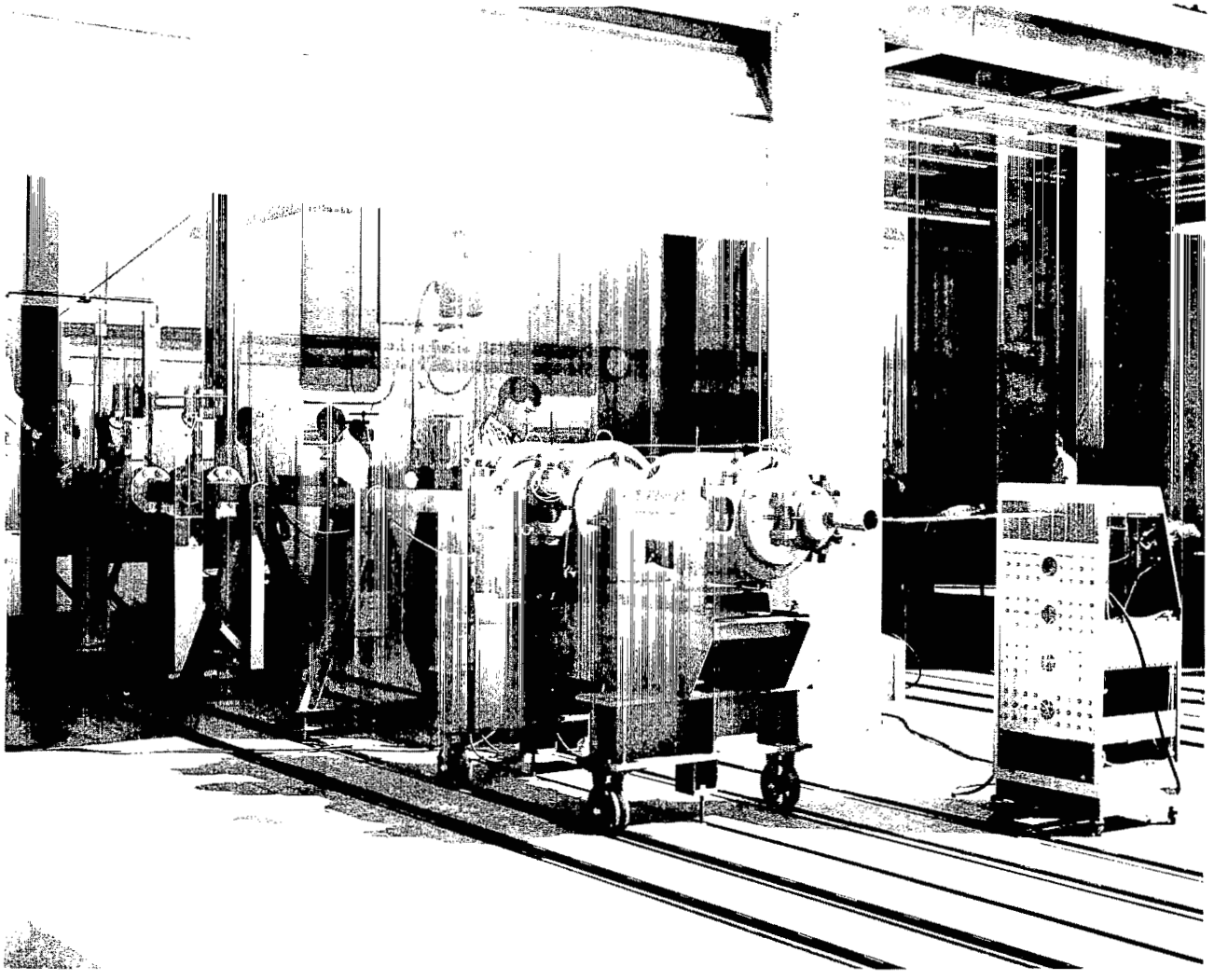

FIGURE 10. COLD FLOW JET FACILITY

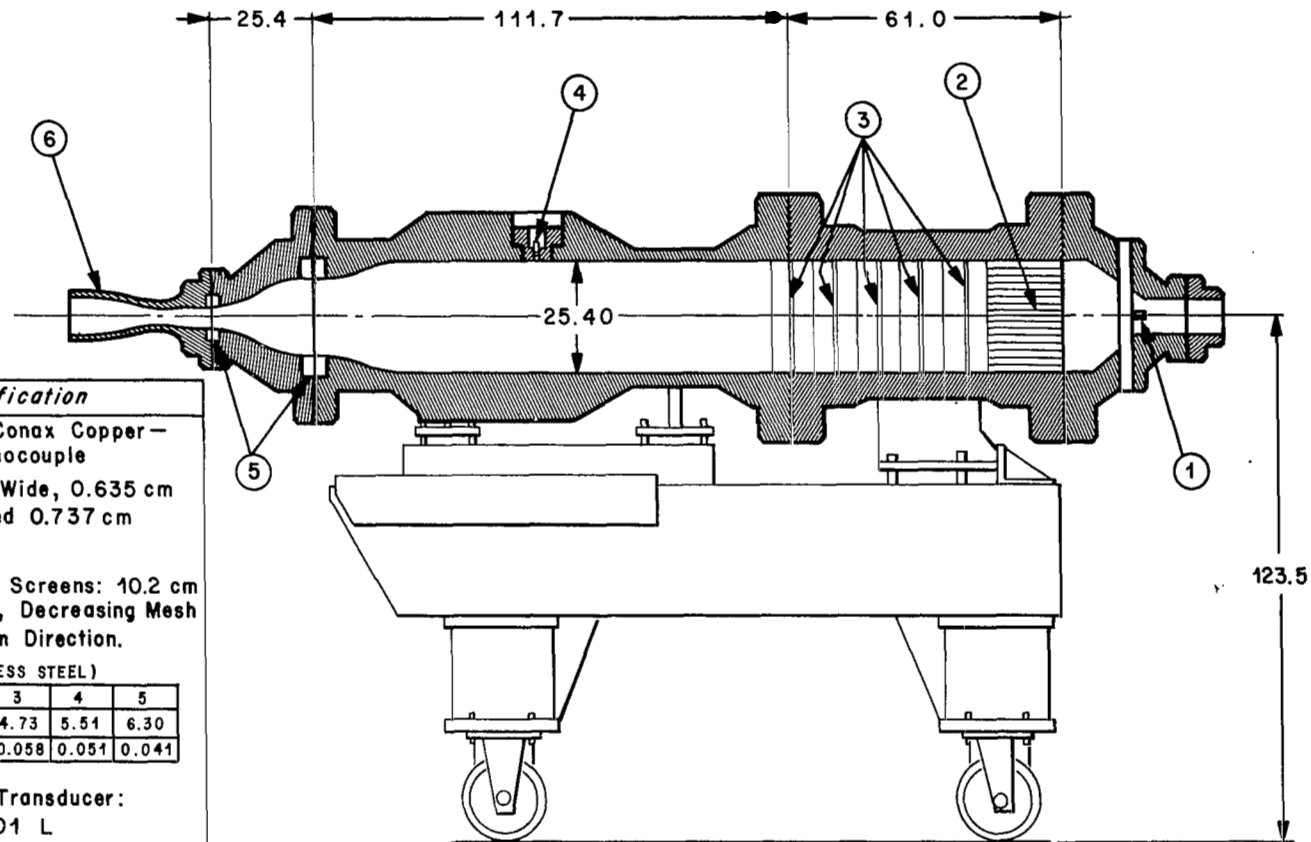

Parts Identification

1. Temperature Probe: Conax Copper–Constantan Thermocouple
2. Honeycomb: 10.2 cm Wide, 0.635 cm Dia. Holes Spaced 0.737 cm Between Centers
3. Turbulence Damping Screens: 10.2 cm Between Screens, Decreasing Mesh Size in Downstream Direction.

SCREEN (STAINLESS STEEL)

	1	2	3	4	5
WIRES/CM	3.15	3.94	4.73	5.51	6.30
WIRE DIA (CM)	0.081	0.063	0.058	0.051	0.041

4. Fluctuating Pressure Transducer: Kistler Model 601 L
5. Slots To Hold Turbulence-Generating Screens (Slots Filled When Screens Not Used)
6. Nozzle

Note: All Dimesions in Centimeters

FIGURE 11. CROSS SECTION OF SETTLING CHAMBER

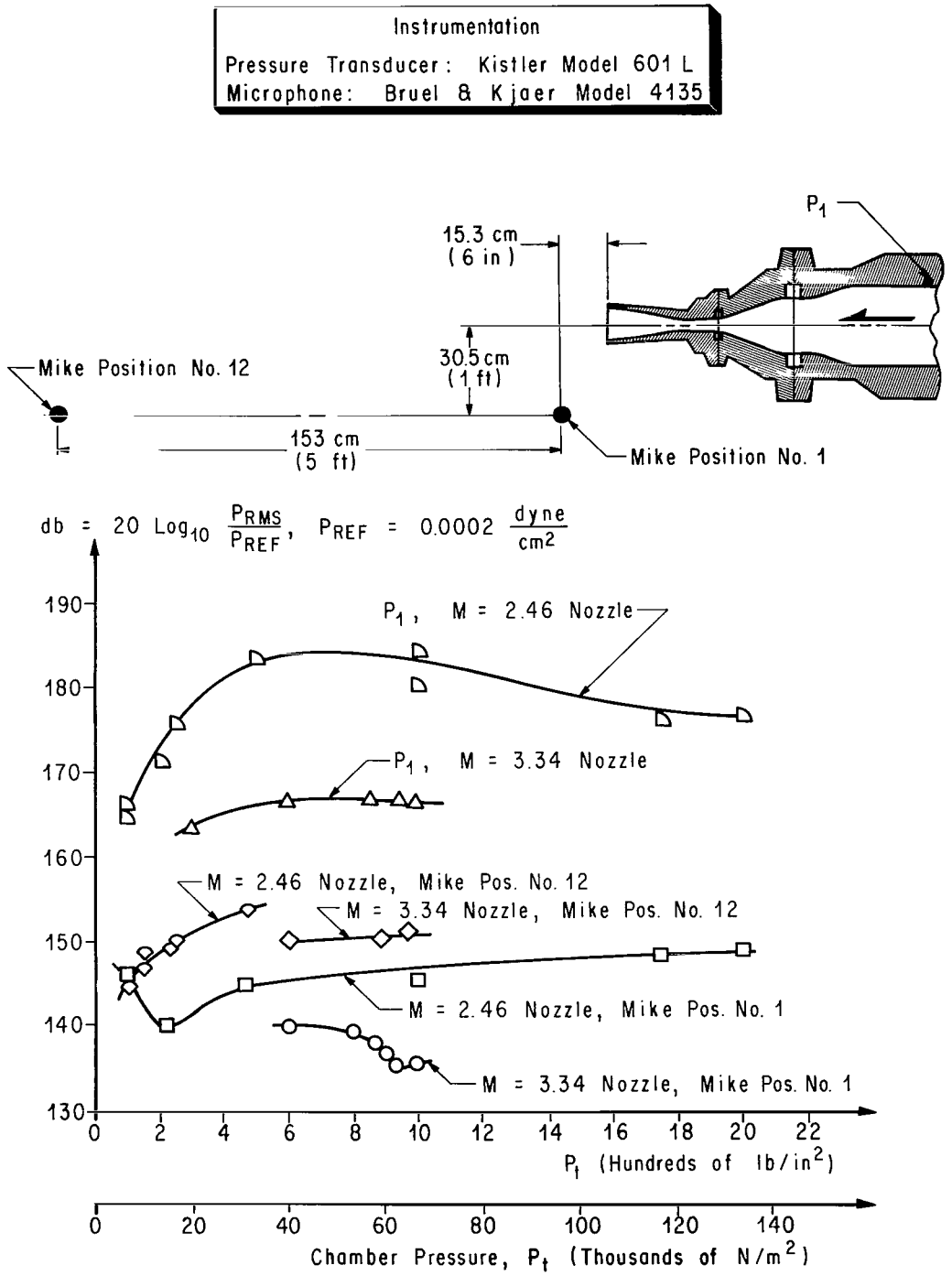

FIGURE 12. SOUND PRESSURE LEVELS AT THE COLD FLOW JET FACILITY

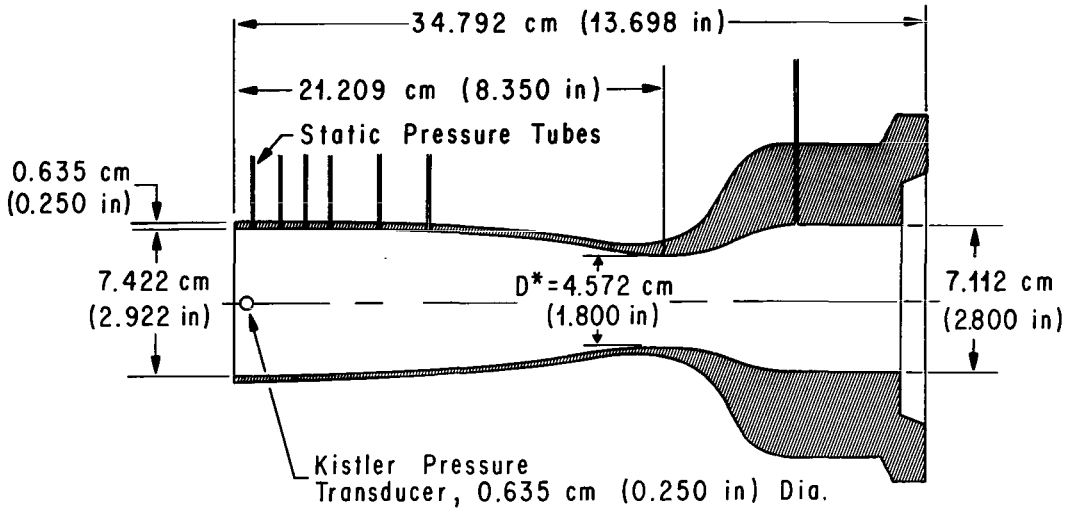

Mach 2.46 Nozzle

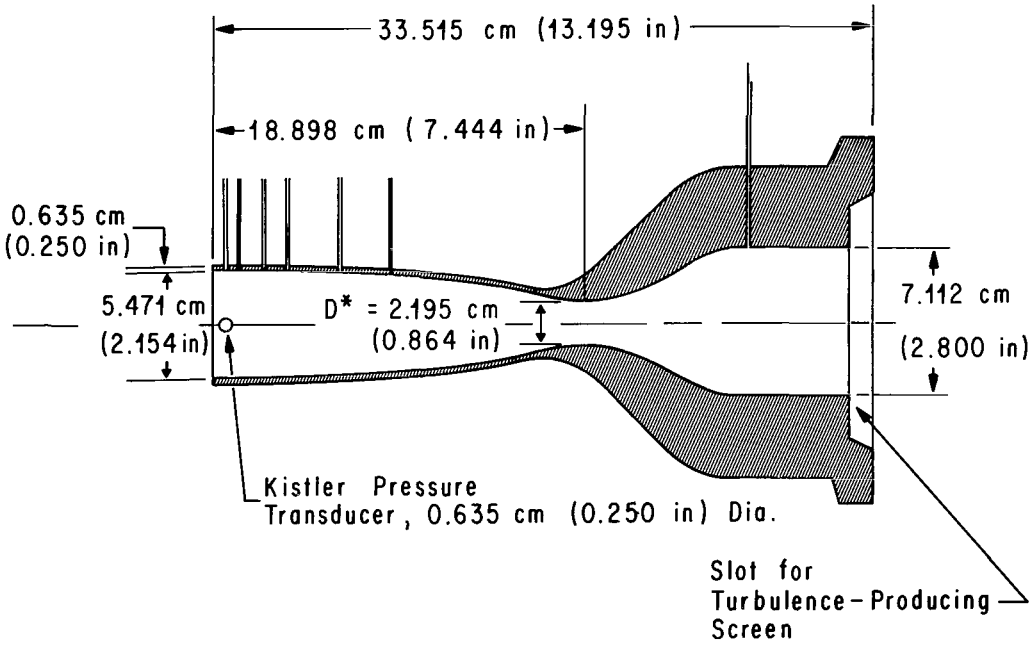

Mach 3.34 Nozzle

FIGURE 13. NOZZLES

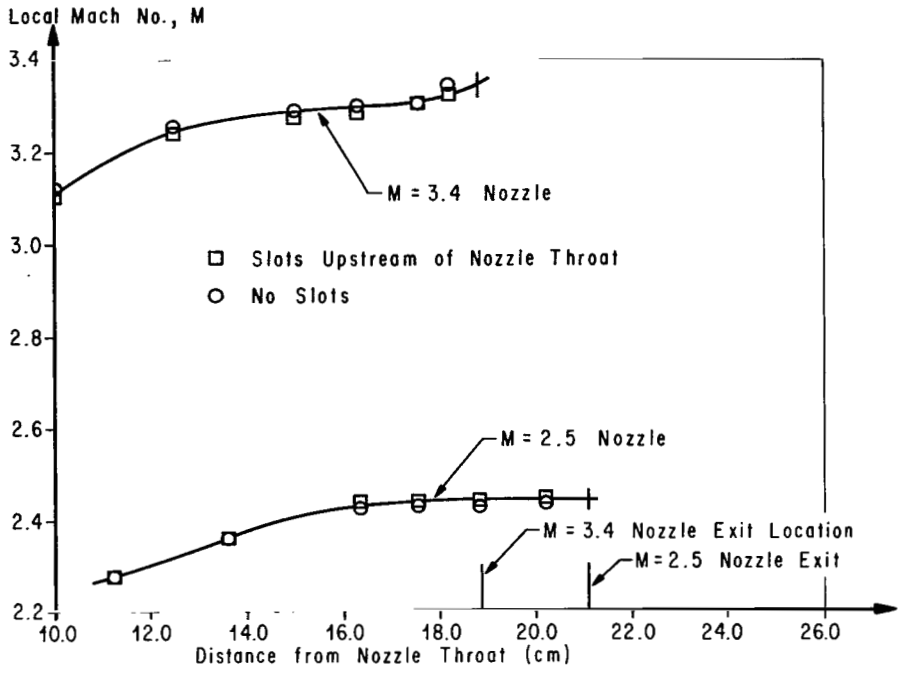

A. Mach Number Distributions Along Nozzle Walls

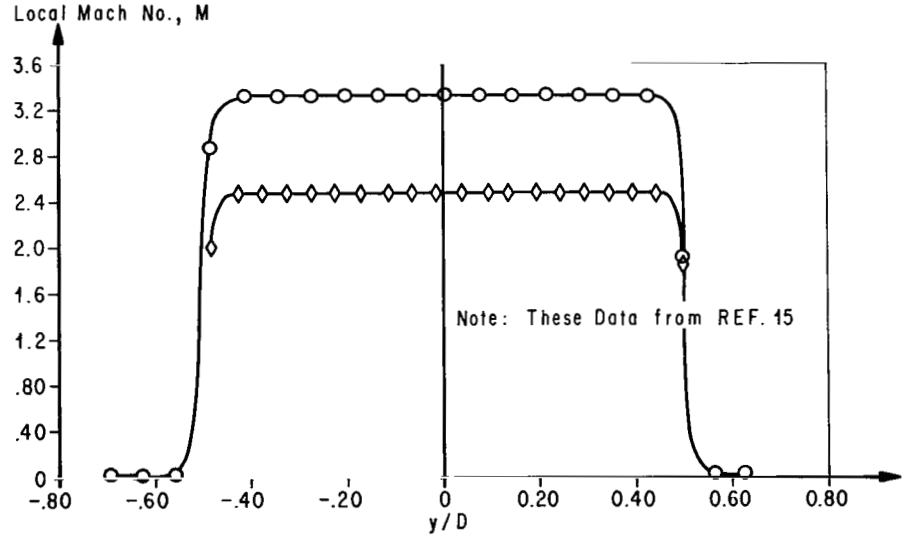

B. Mach Number Distributions Across Nozzle Exits

FIGURE 14. MACH NUMBER CHARACTERISTICS OF THE NOZZLES

a. Schlieren

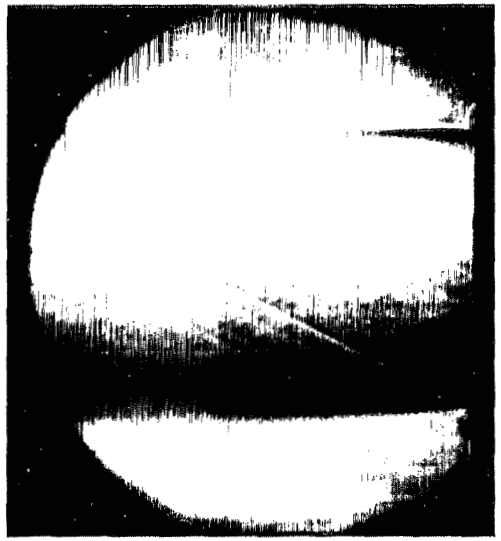

b. Shadowgraph

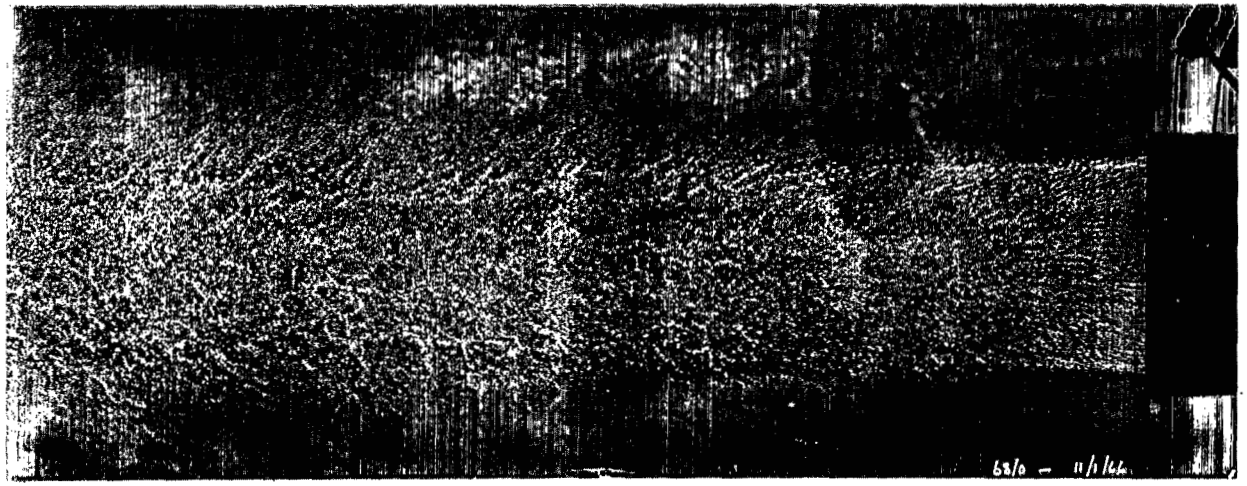

FIGURE 15. SCHLIEREN AND SHADOWGRAPH OF MACH 2.46 JET

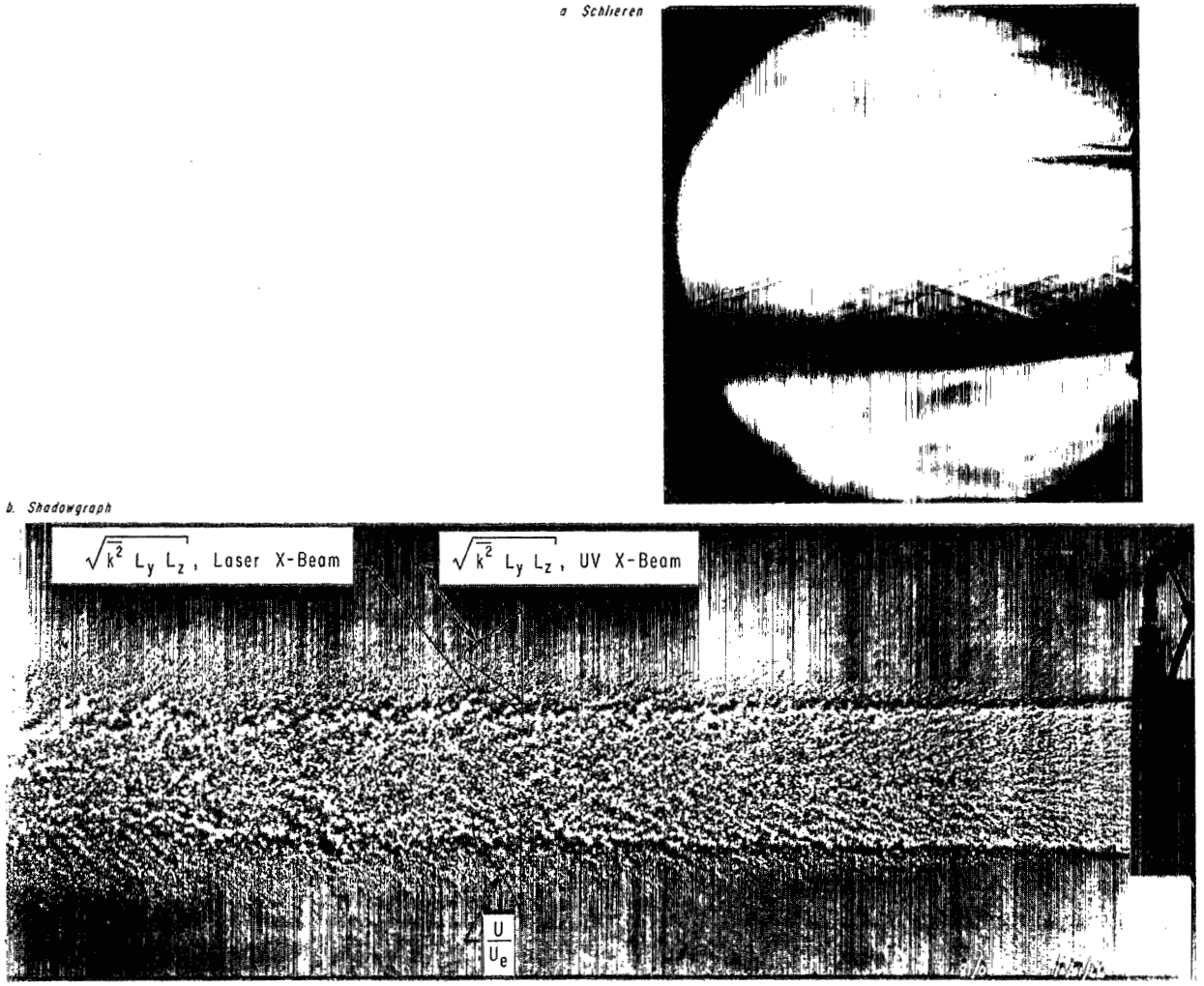

FIGURE 16. SCHLIEREN AND SHADOWGRAPH OF MACH 3.34 JET

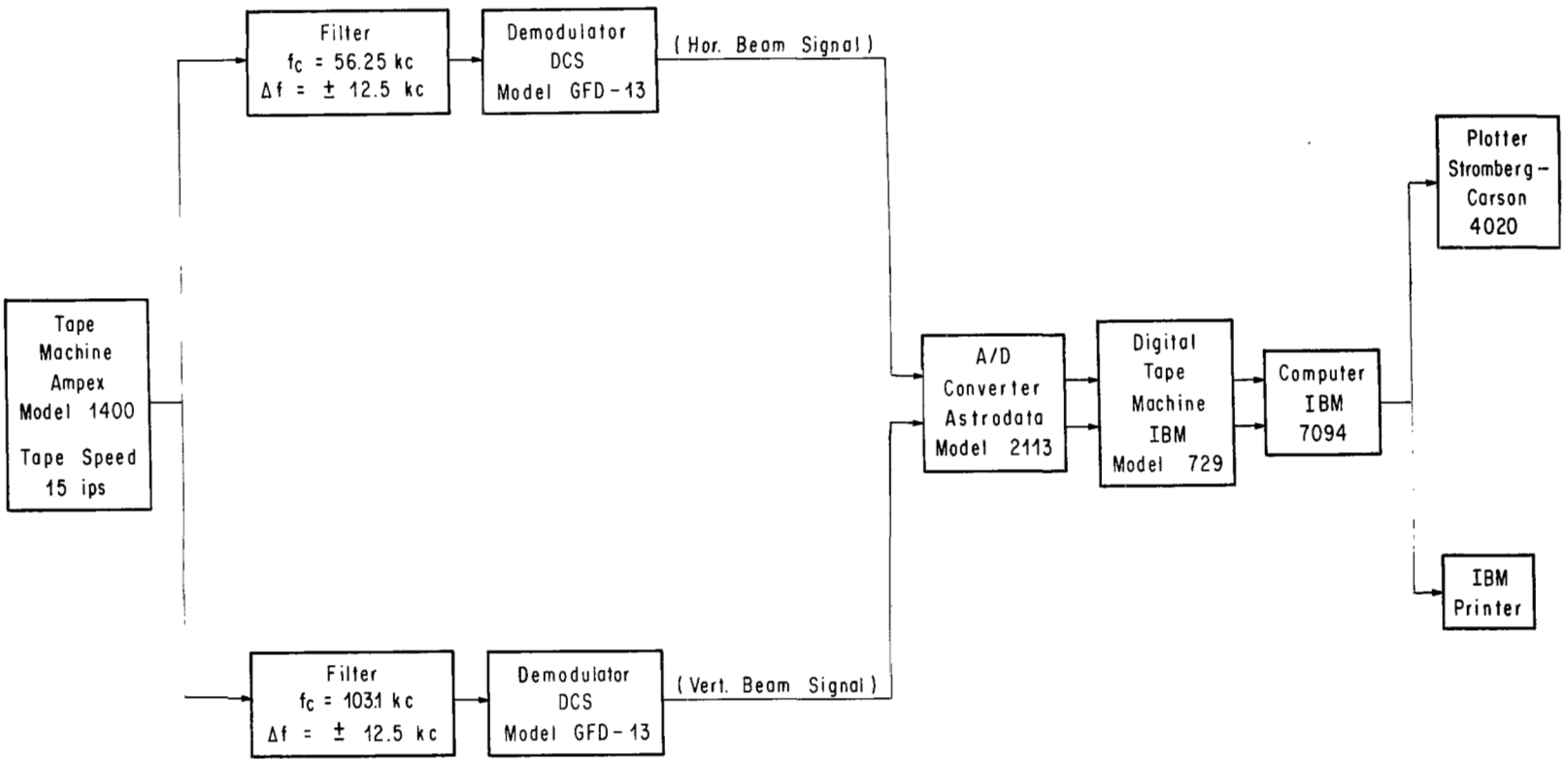

FIGURE 17. DIGITAL DATA REDUCTION CHAIN

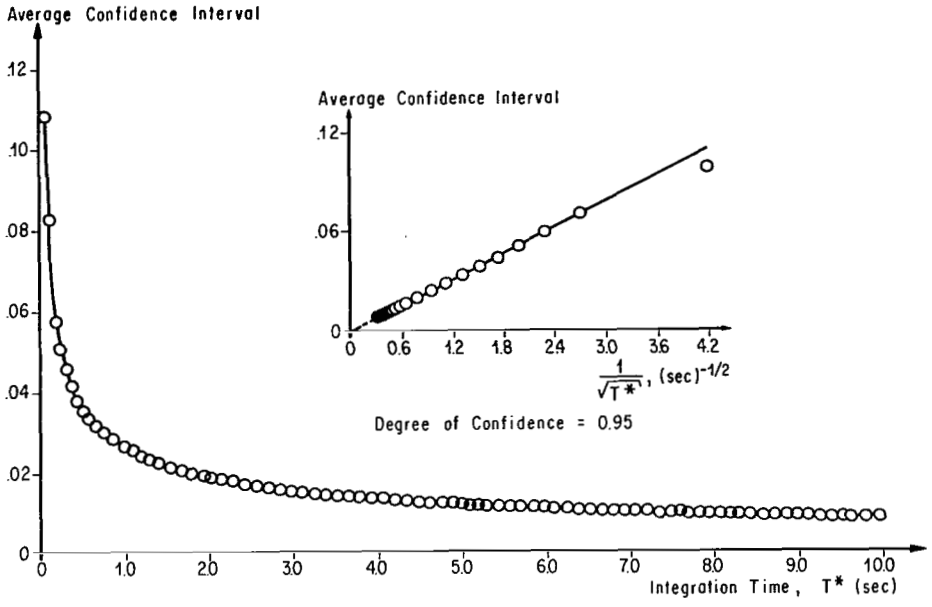

(a) Average Confidence Interval As Function of Integration Time

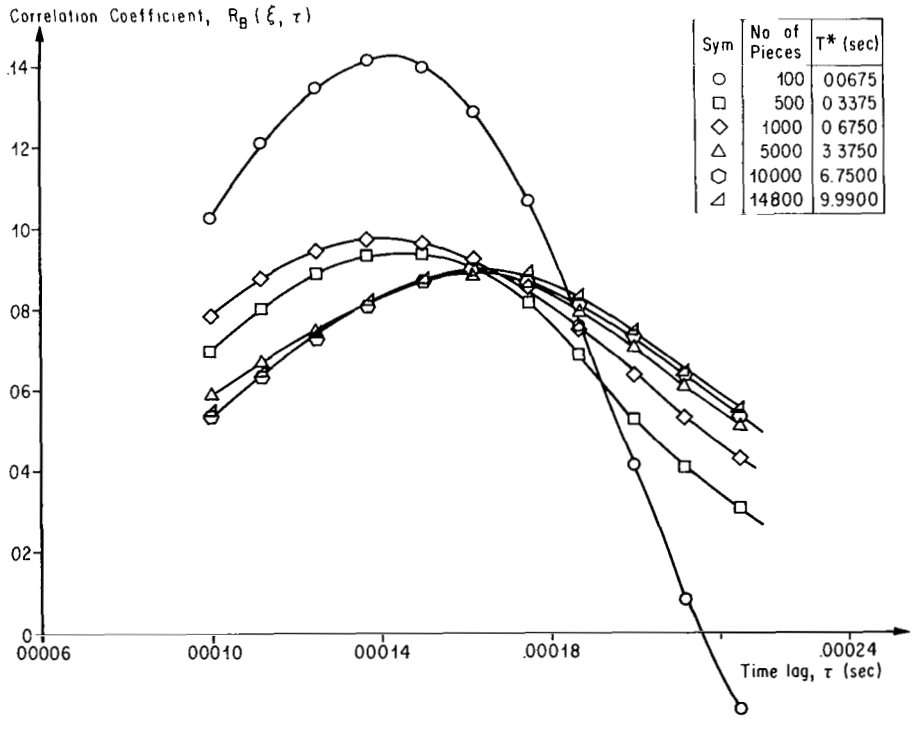

(b) Variation of Correlation Coefficient Curves With Integration Time

FIGURE 18. EFFECT OF INTEGRATION TIME ON ACCURACY OF CORRELATION COEFFICIENTS
(M = 3.34 Nozzle, x/D = 2, y/D = 0.652, Δx = 3.05 cm)

Test	Settling Chamber Conditions		Atmospheric Conditions			
	P_t (N/m^2)	T_t (°C)	P_a (N/m^2)	T_a (°C)	Relative Humidity (per cent)	Specific Humidity
UV X-Beam	5.989×10^6	3	1.004×10^5	10	75	0.0057
Laser X-Beam	5.998×10^6	9	1.000×10^5	15	84	0.0088
Pressure	6.157×10^6	4	0.993×10^5	24	—	—

M = 3.34 Nozzle

$\frac{x}{D} = 4.0$

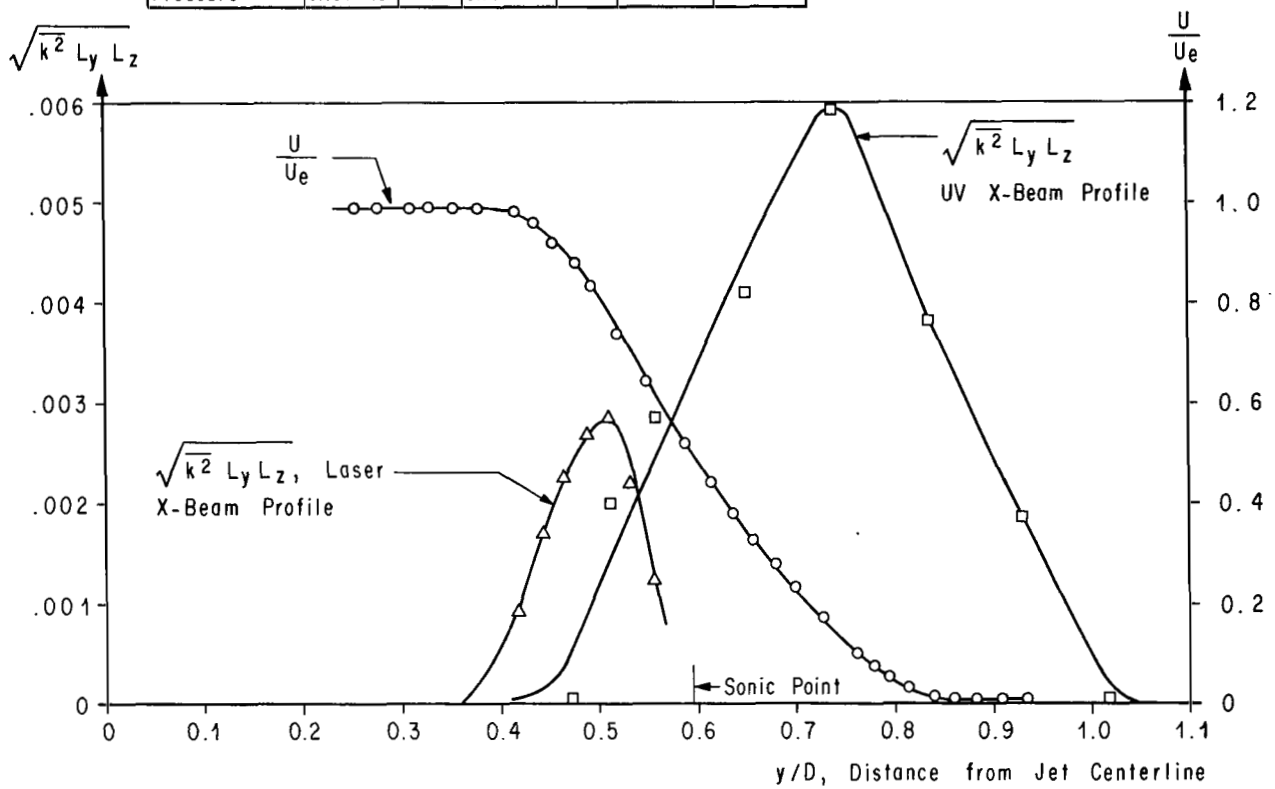

FIGURE 19. COMPARISON OF TURBULENCE INTENSITY PROFILES AND MEAN VELOCITY PROFILE

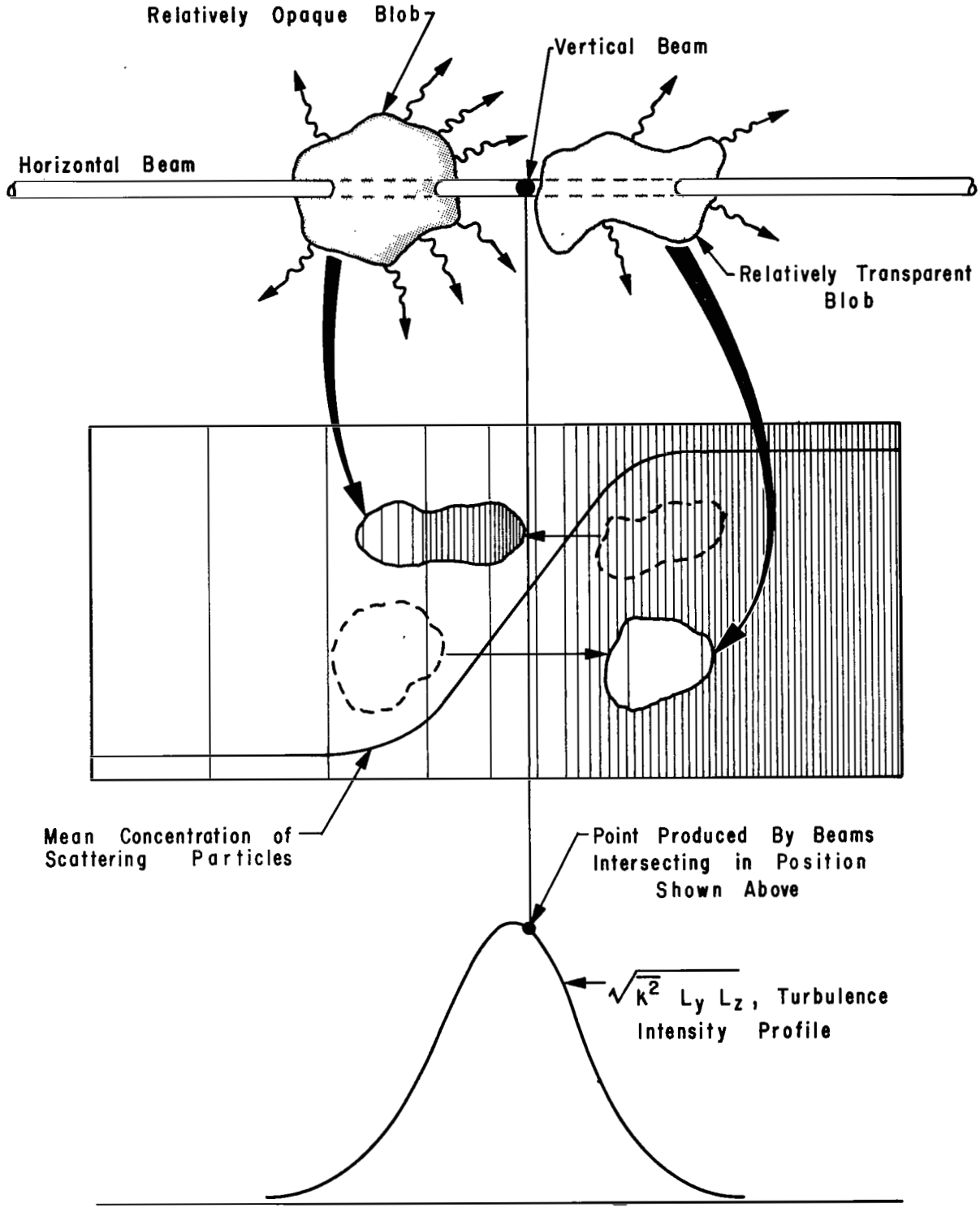

FIGURE 20. ILLUSTRATION OF HOW A MEAN CONCENTRATION GRADIENT OF SCATTERING PARTICLES CAN CAUSE A PEAK IN CROSSED-BEAM TURBULENCE INTENSITY PROFILE

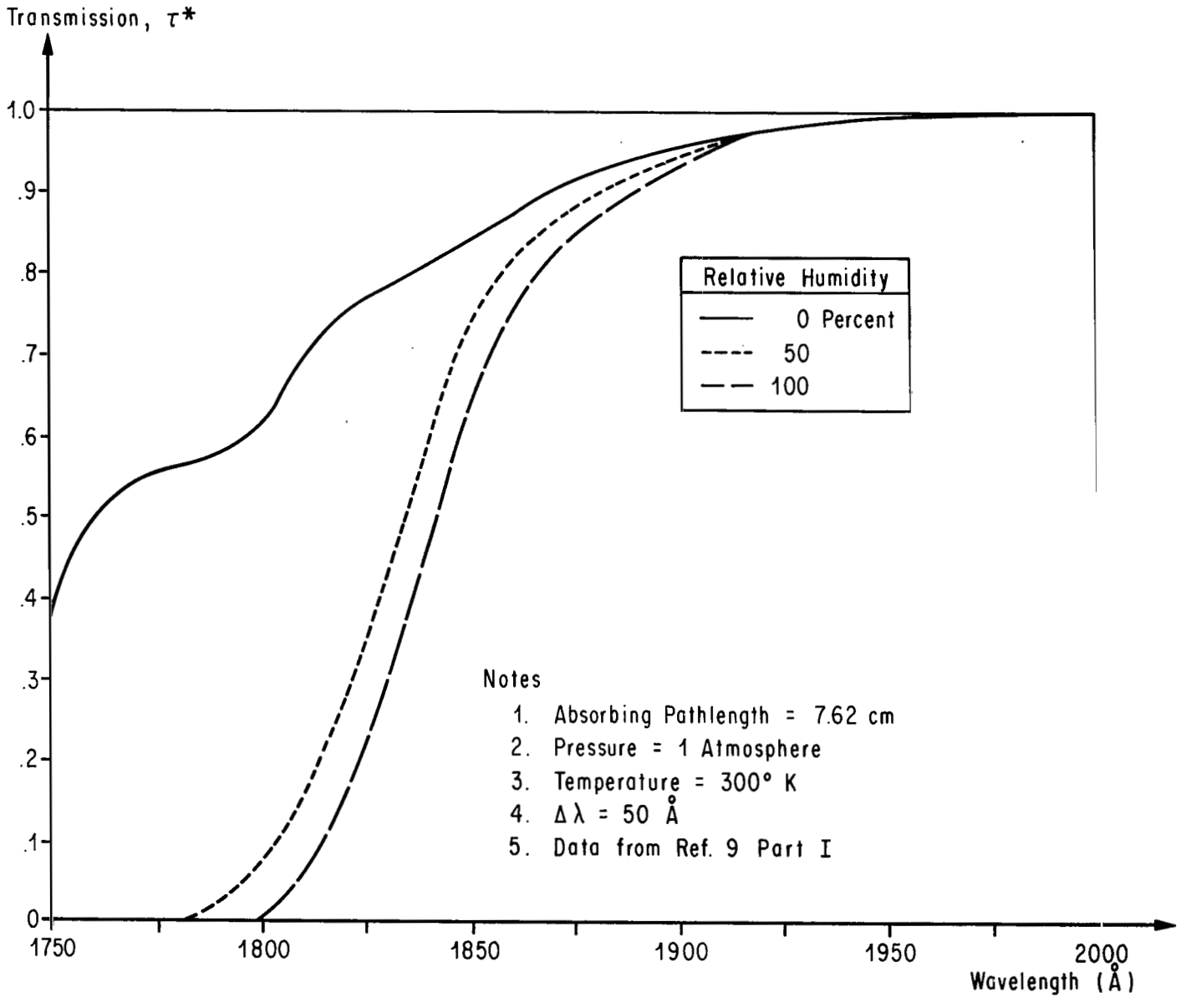

FIGURE 21. INFLUENCE OF WATER VAPOR ON THE TRANSMISSION OF ULTRAVIOLET RADIATION THROUGH AIR

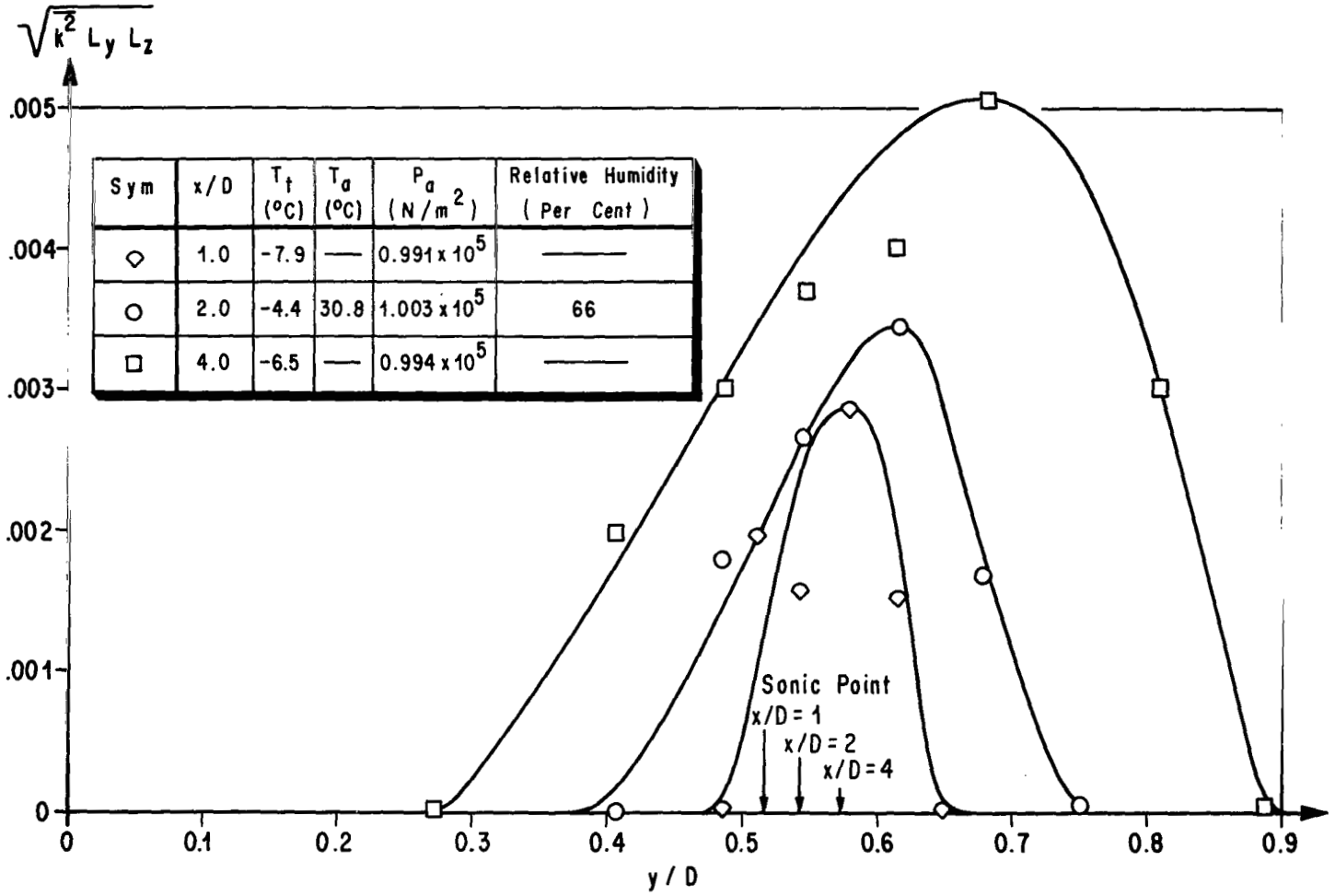

FIGURE 22. RELATIVE INTENSITY PROFILES OF MACH 2.46 JET

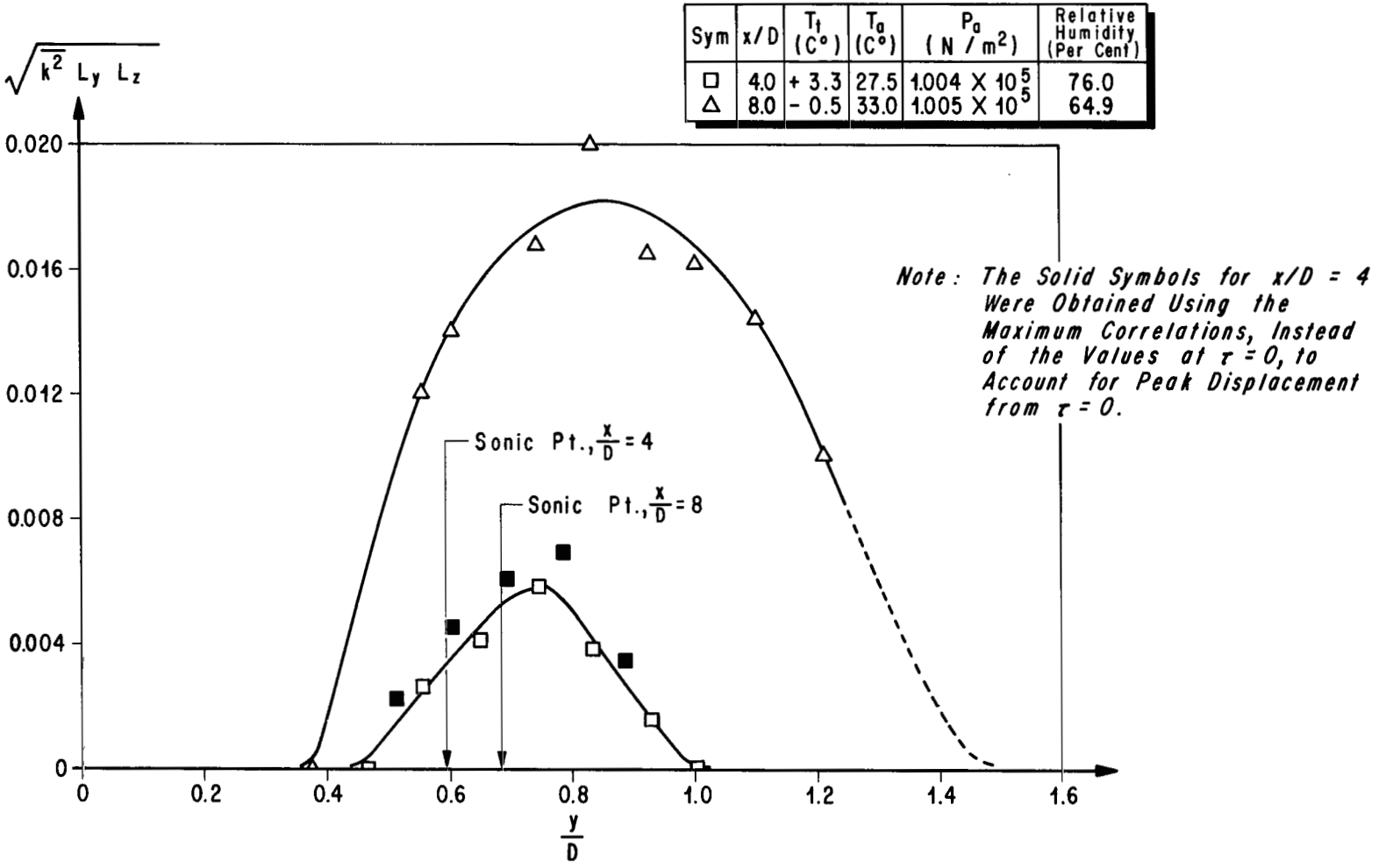

FIGURE 23. RELATIVE INTENSITY PROFILES OF MACH 3.34 JET

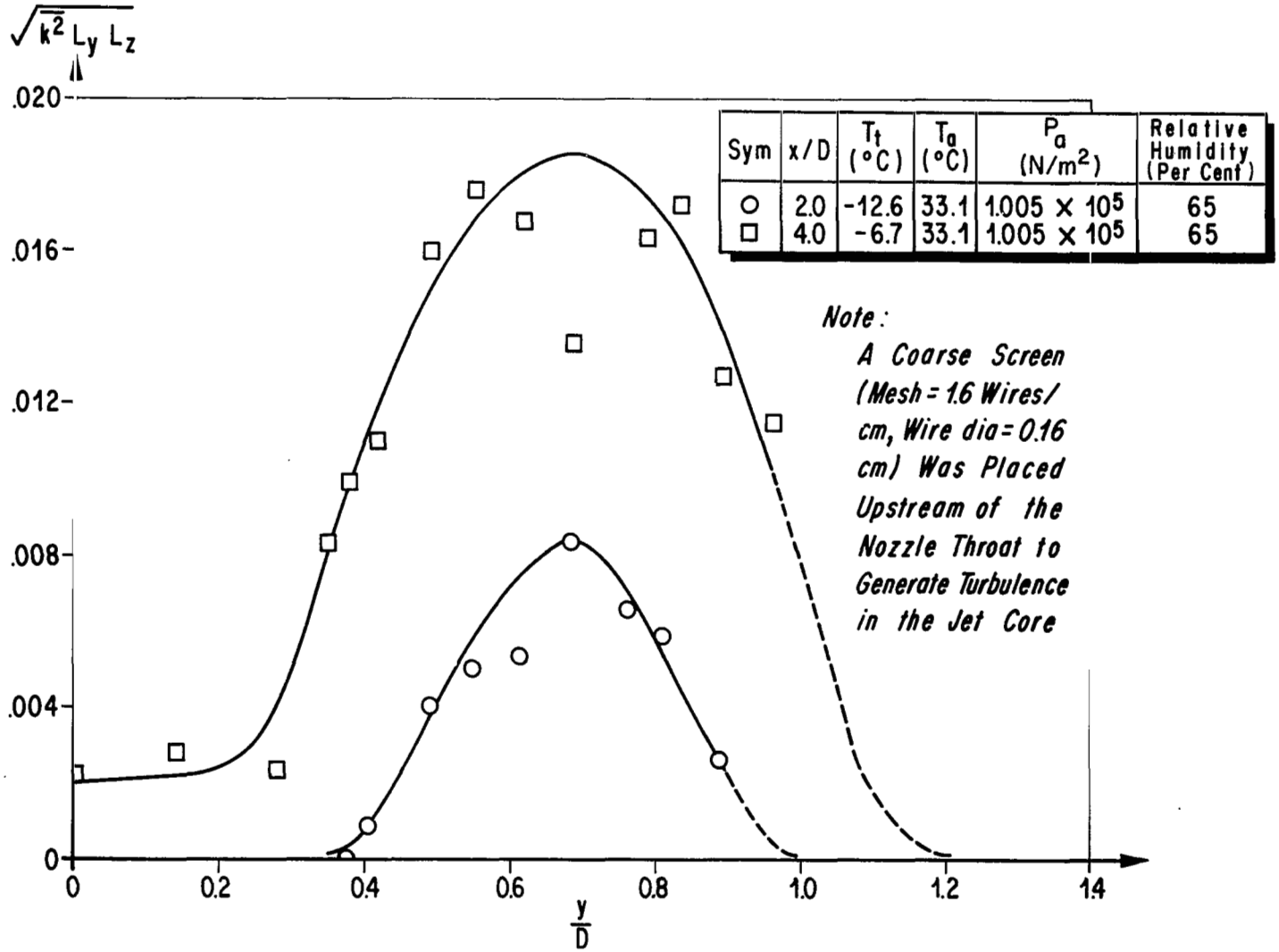

FIGURE 24. RELATIVE INTENSITY PROFILES OF MACH 2.46 JET (With Screen)

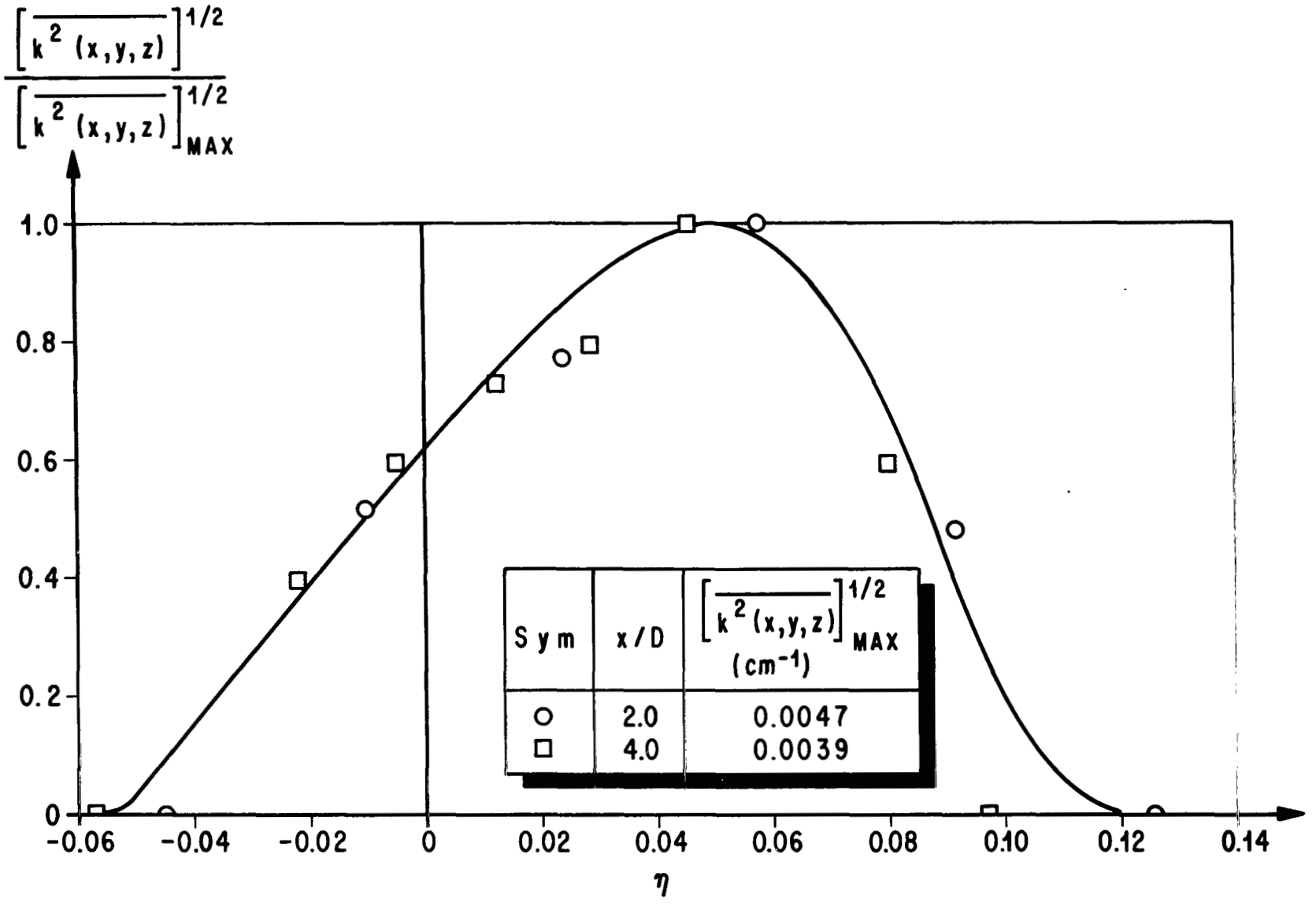

FIGURE 25. NON-DIMENSIONAL INTENSITY PROFILE OF MACH 2.46 JET

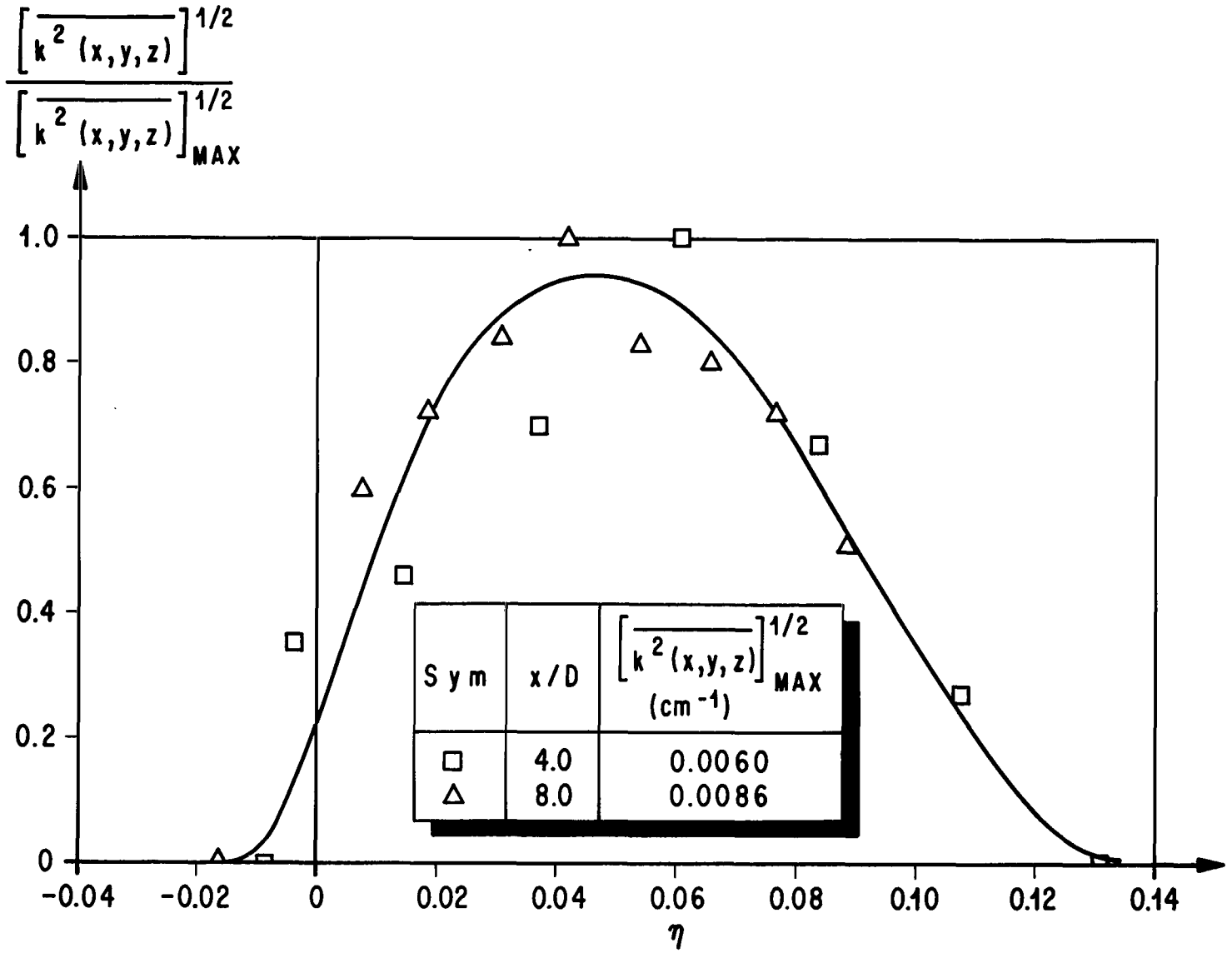

FIGURE 26. NON-DIMENSIONAL INTENSITY PROFILE OF MACH 3.34 JET

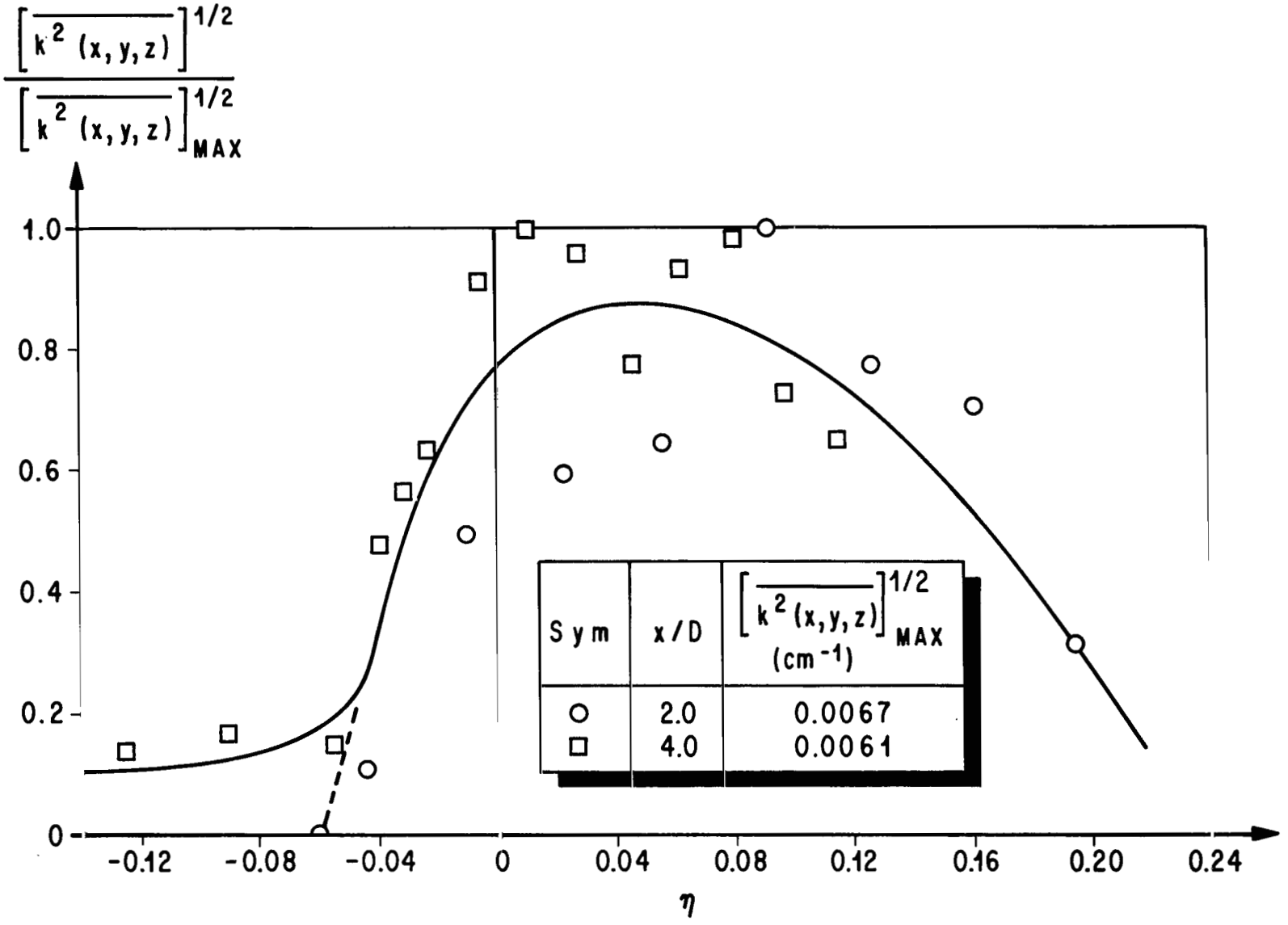

FIGURE 27. NON-DIMENSIONAL INTENSITY PROFILE OF MACH 2.46 JET (With Screen)

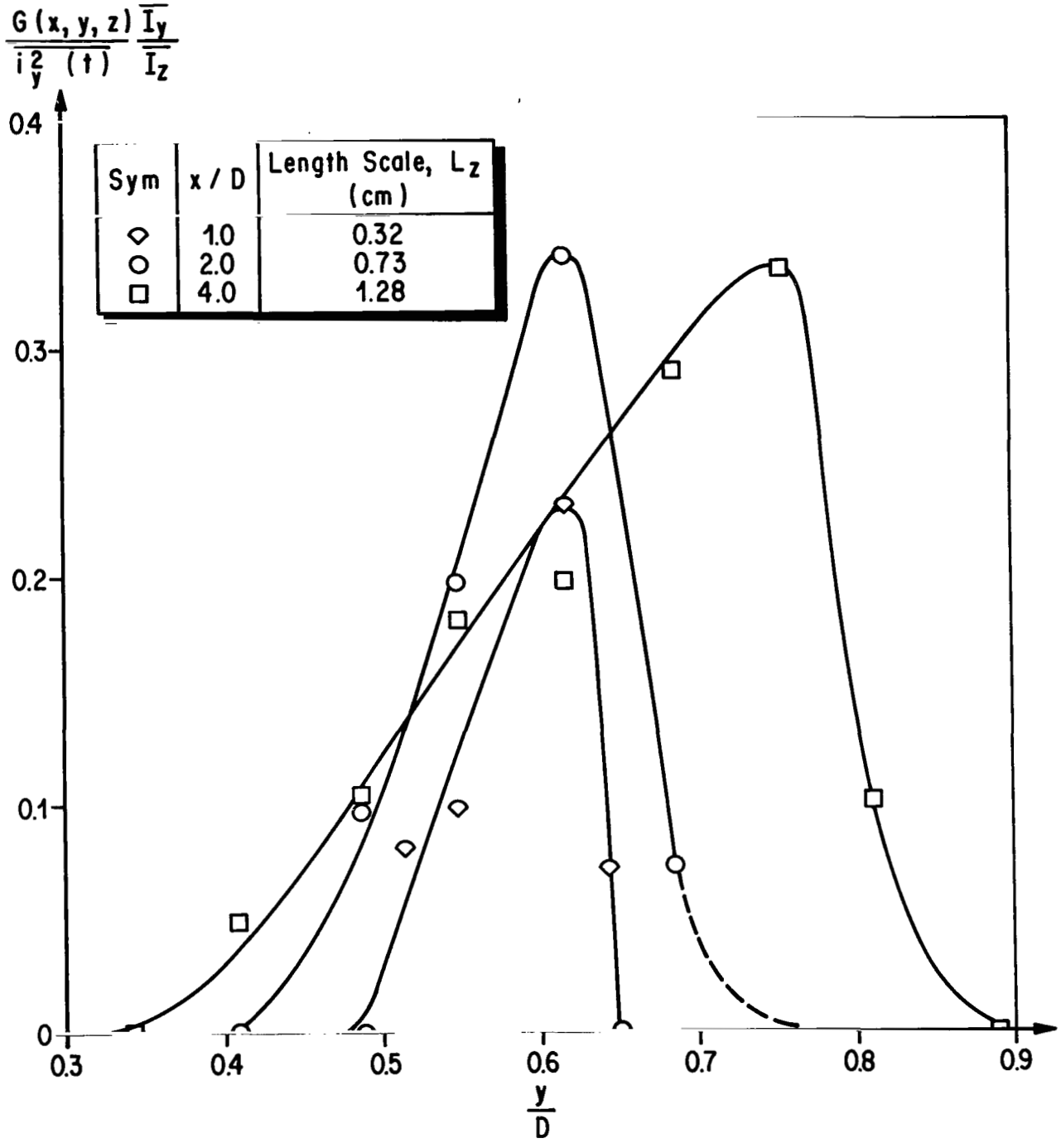

FIGURE 28. DETERMINATION OF INTEGRAL LENGTH SCALES, L_z, OF MACH 2.46 JET

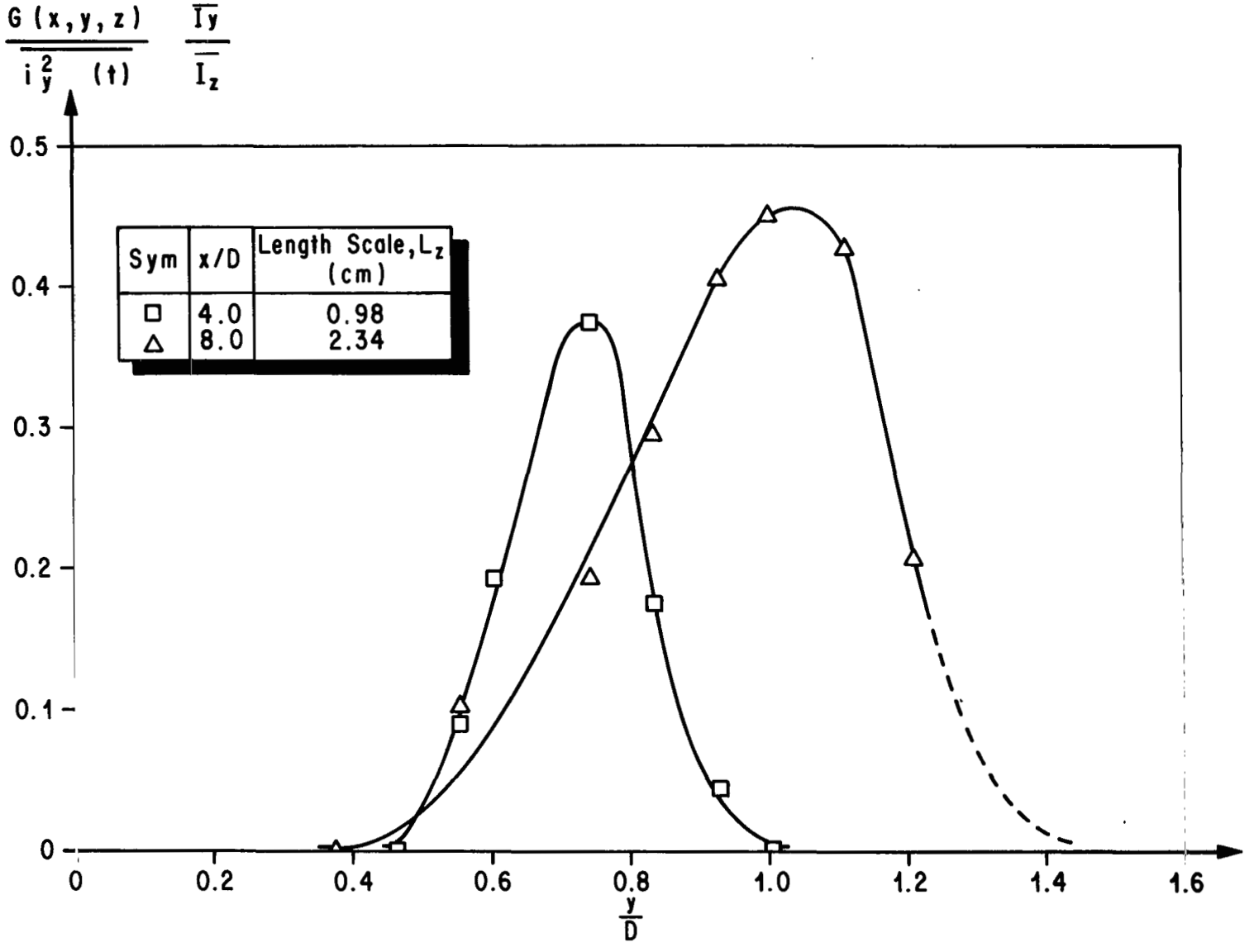

FIGURE 29. DETERMINATION OF INTEGRAL LENGTH SCALES, L_z, OF MACH 3.34 JET

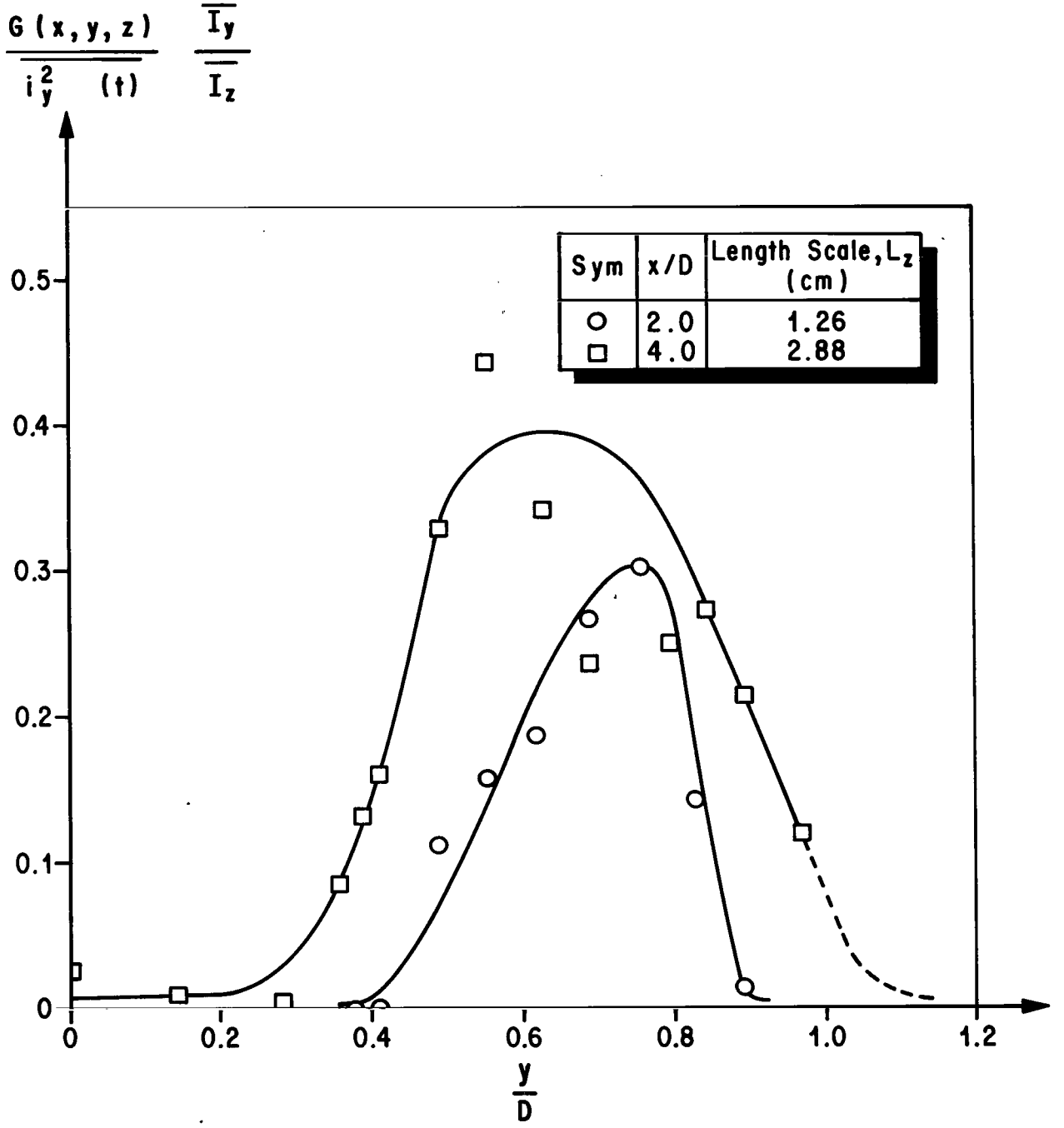

FIGURE 30. DETERMINATION OF INTEGRAL LENGTH SCALES, L_z, OF MACH 2.46 JET (With Screen)

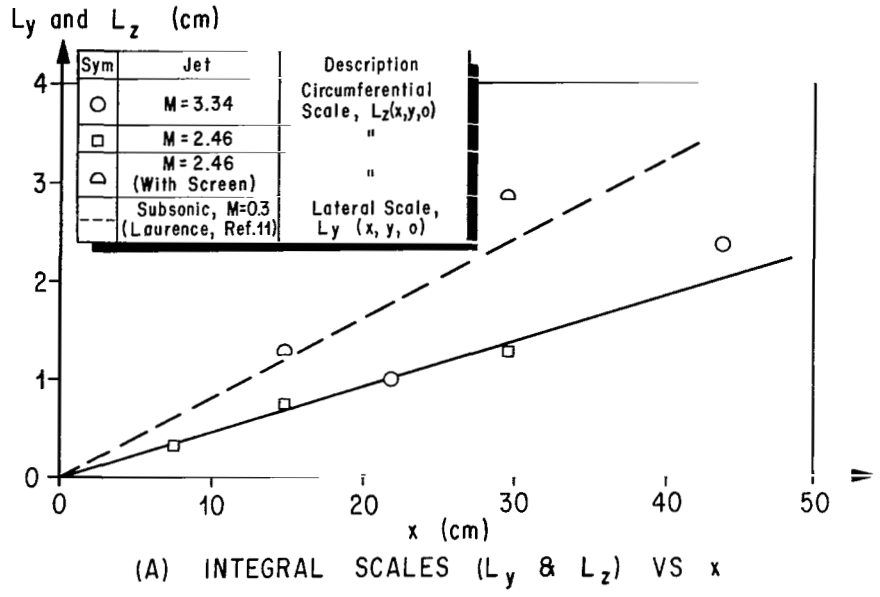

(A) INTEGRAL SCALES (L_y & L_z) VS x

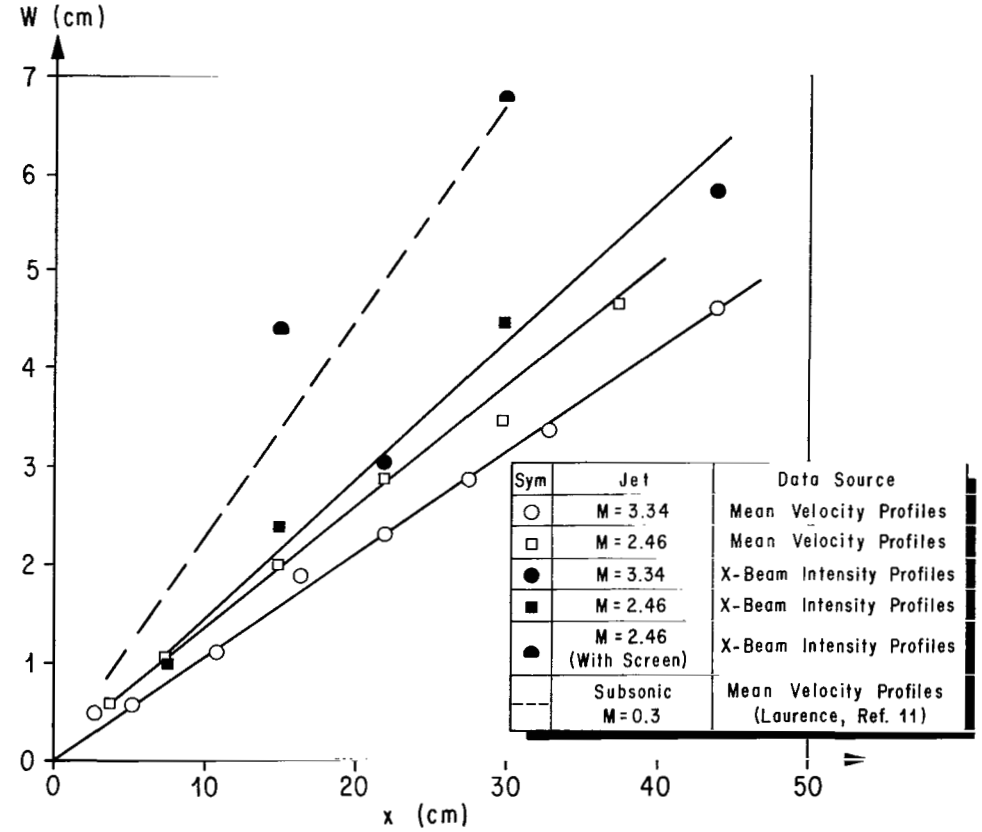

(B) W VS x

FIGURE 31. VARIATION OF INTEGRAL SCALES AND SHEAR LAYER THICKNESS, W, WITH DISTANCE FROM NOZZLE EXIT

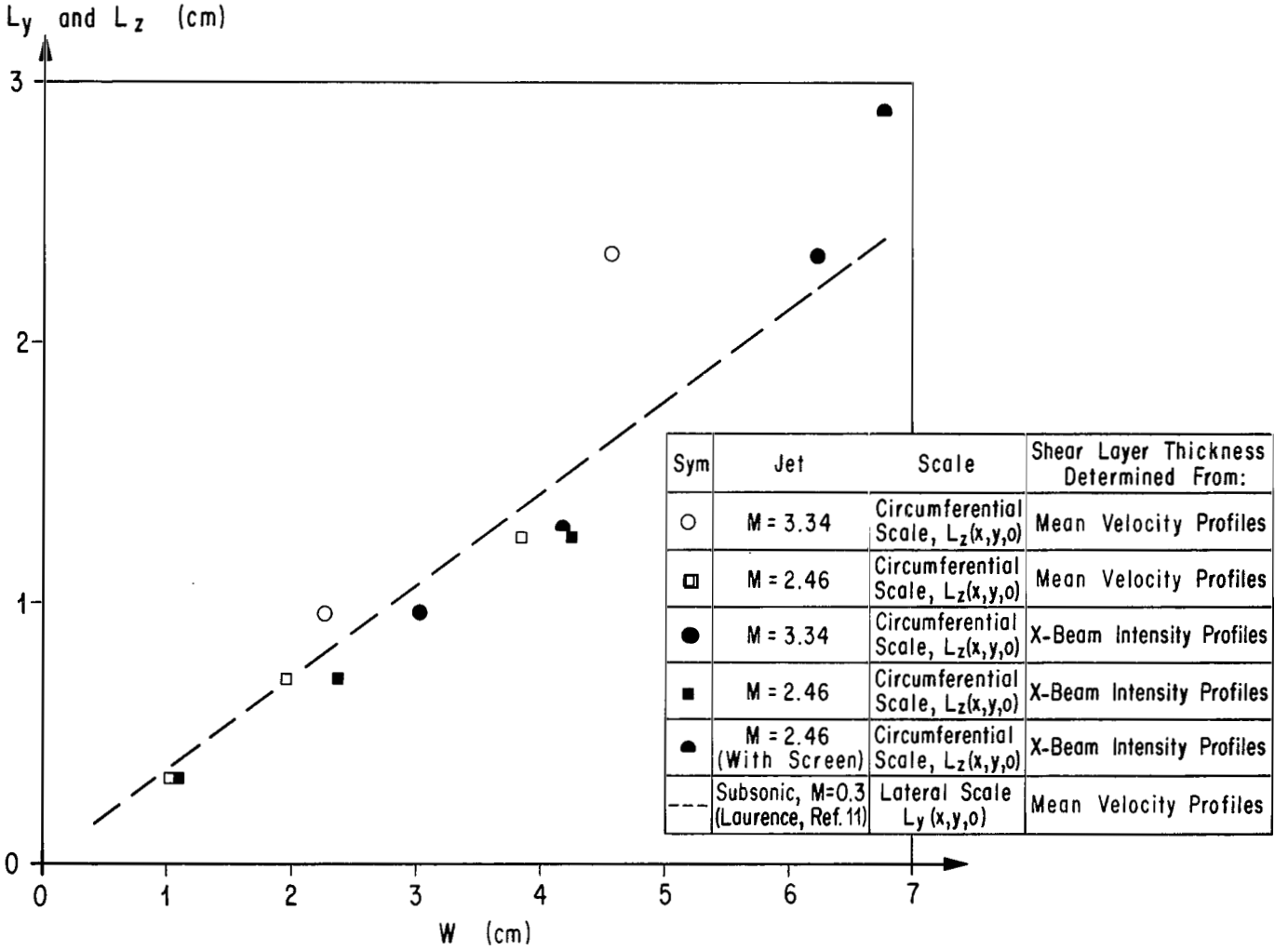

FIGURE 32. VARIATION OF INTEGRAL SCALES (L_y and L_z) WITH SHEAR LAYER THICKNESS, W

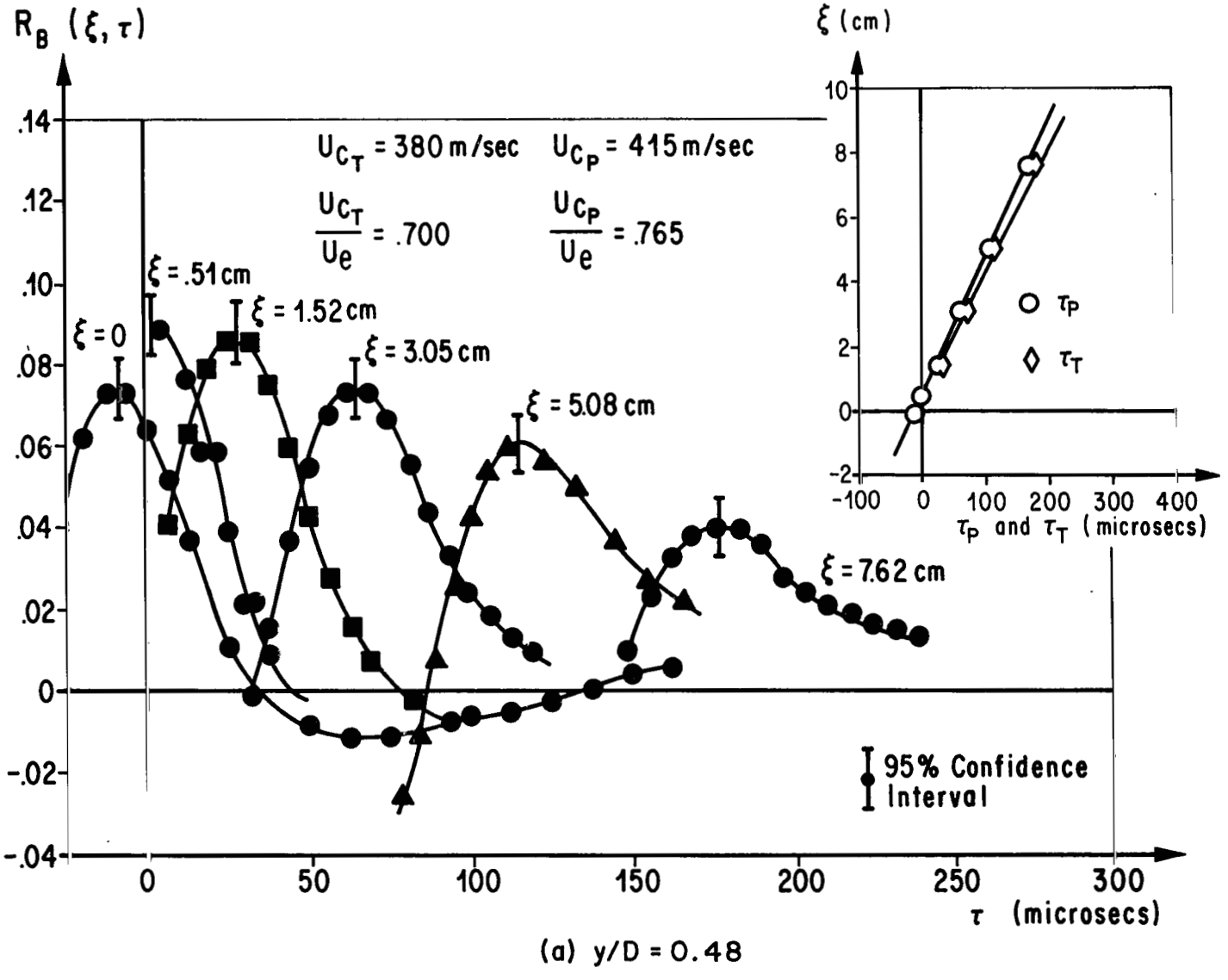

FIGURE 33. TWO BEAM SPACE-TIME CORRELATIONS IN MACH 2.46 JET AT x/D = 2

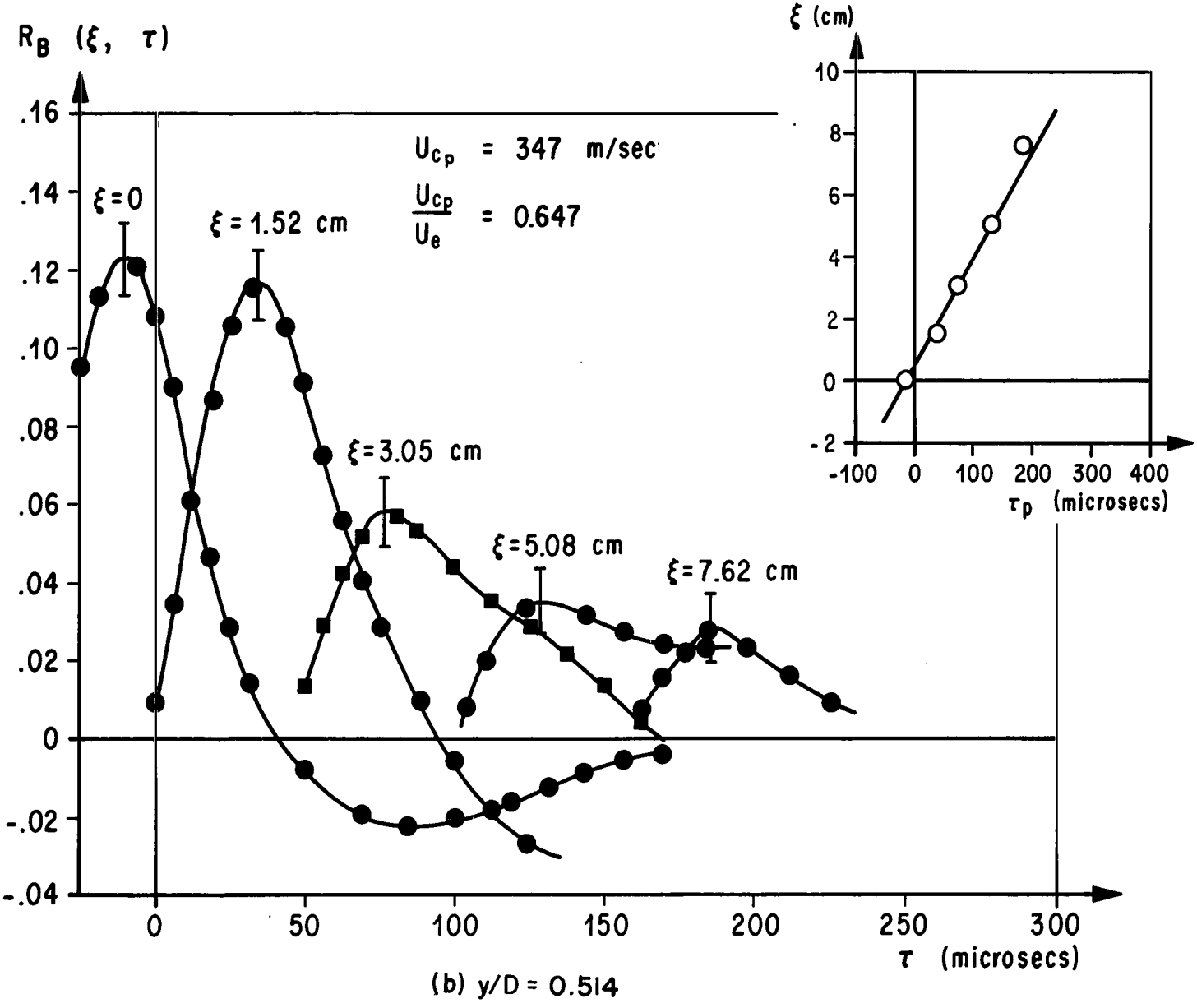

FIGURE 33. (Continued)

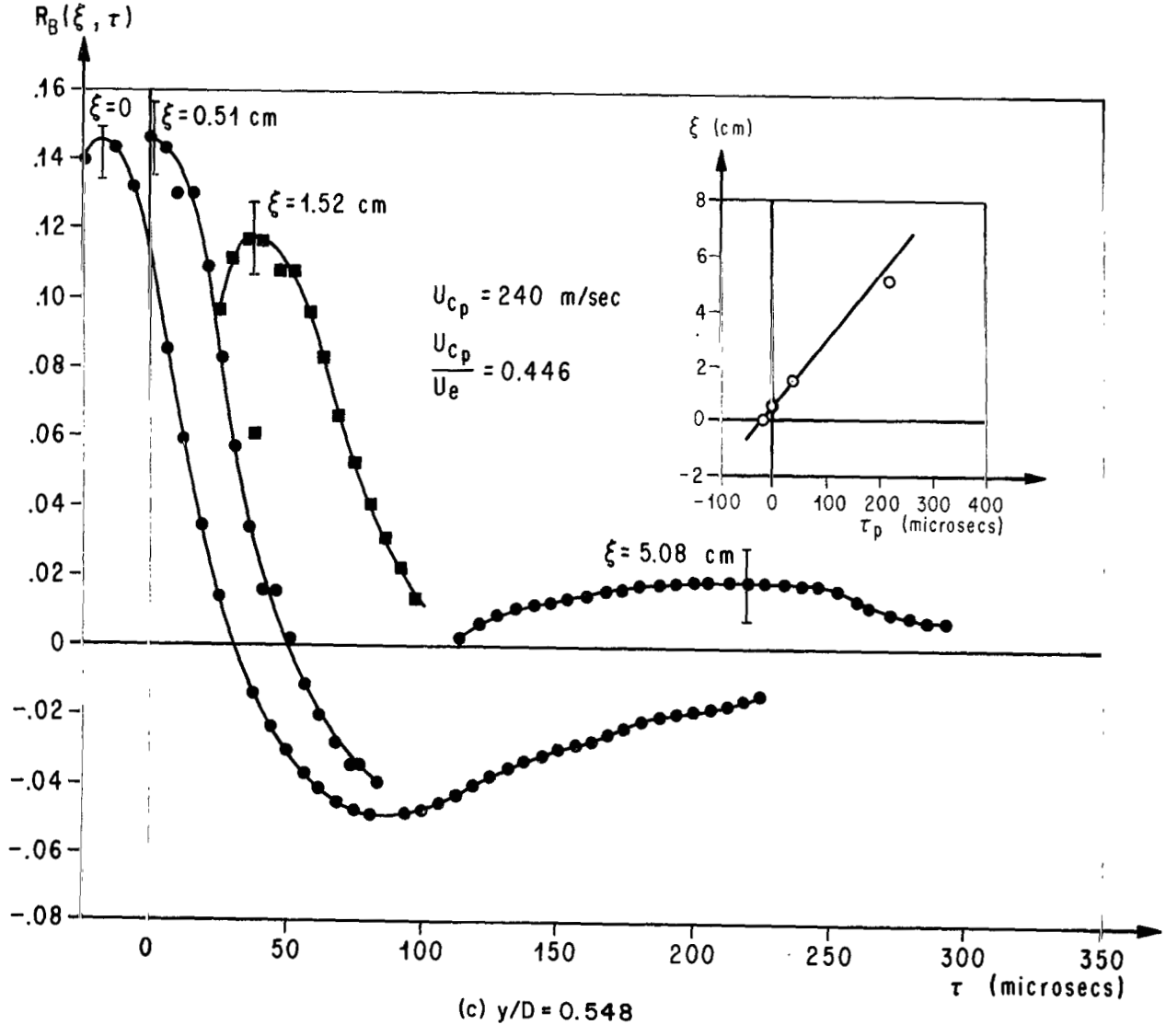

FIGURE 33. (Continued)

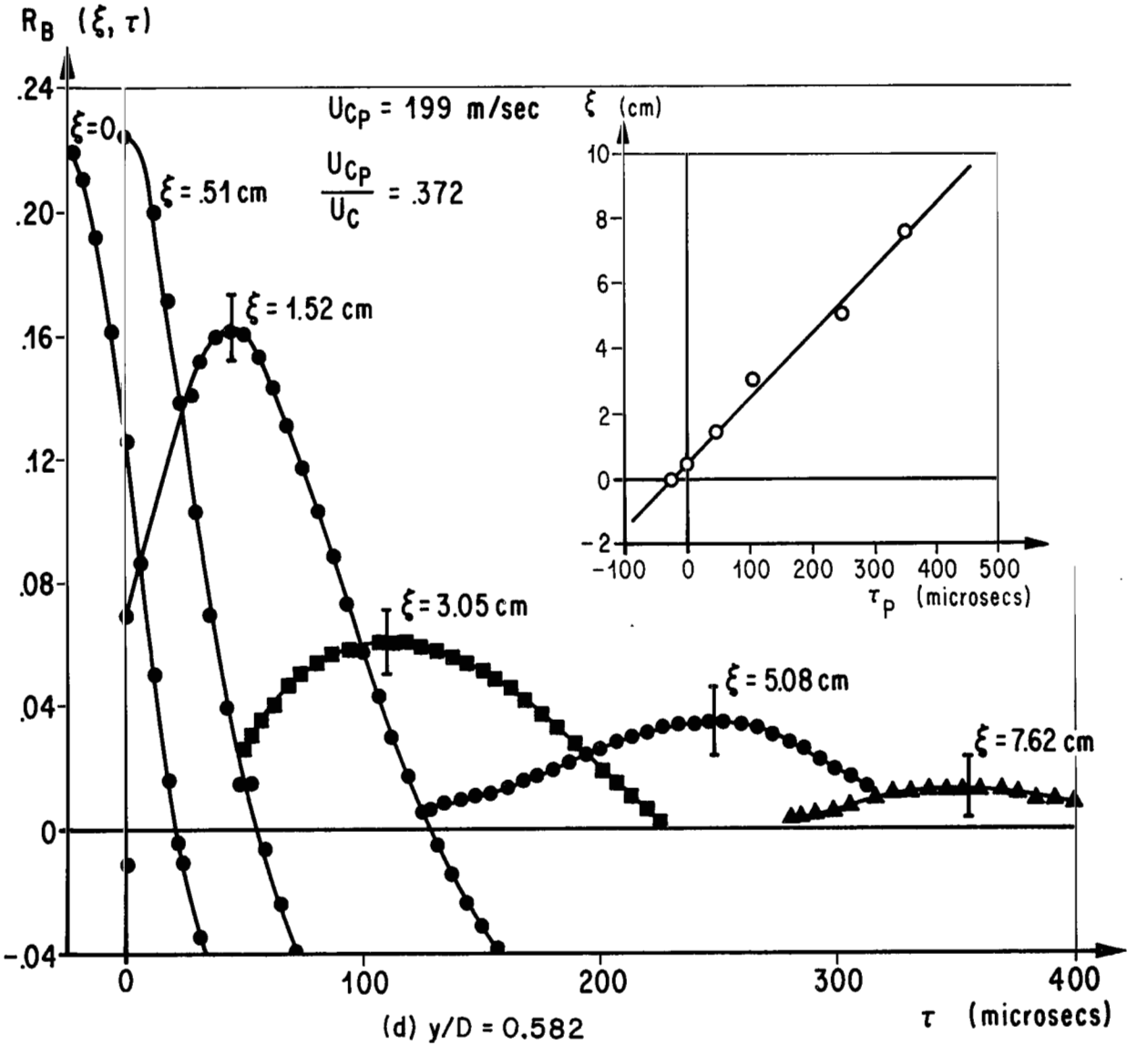

FIGURE 33. (Continued)

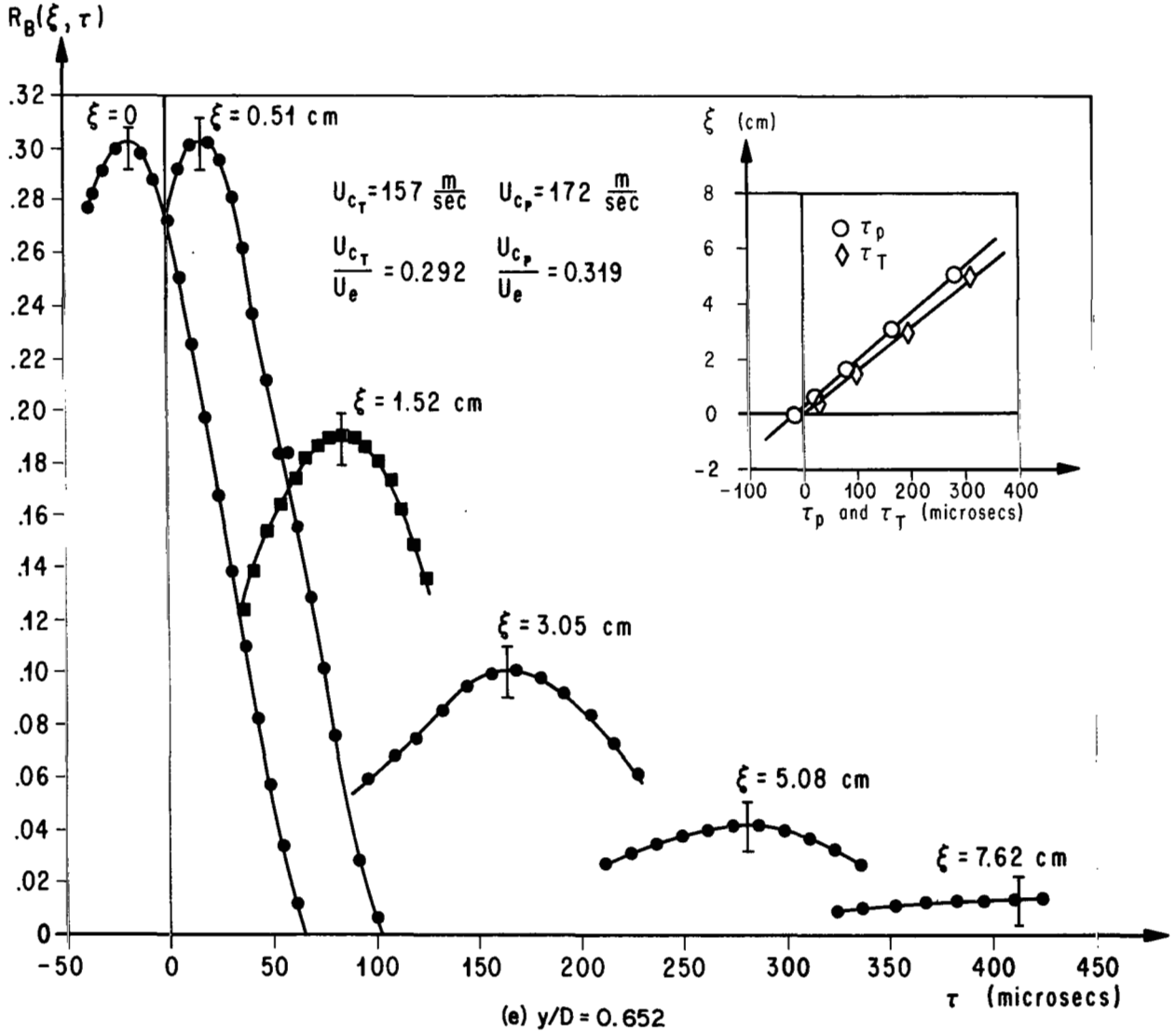

FIGURE 33. (Concluded)

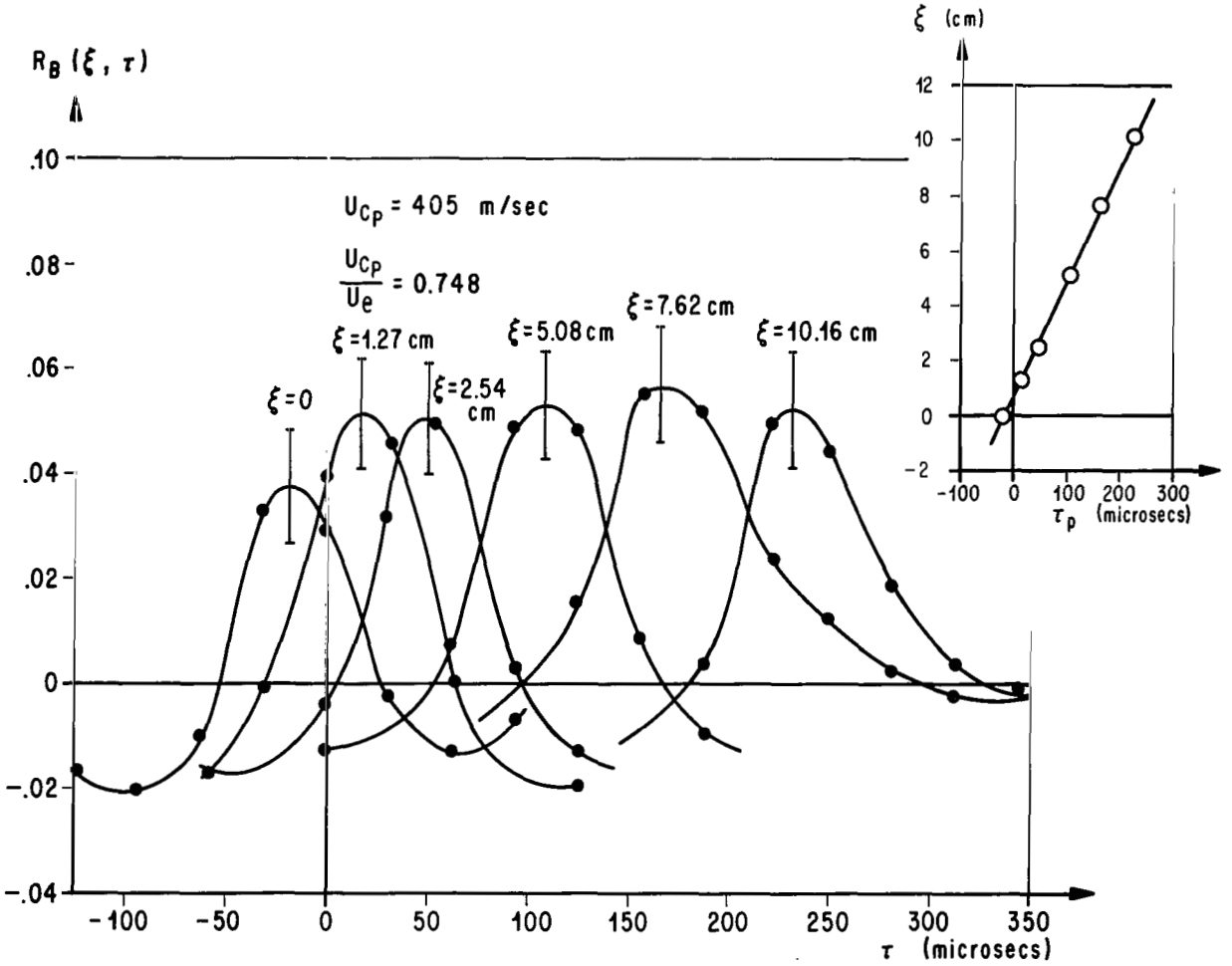

(a) y/D = 0.411

FIGURE 34. TWO BEAM SPACE-TIME CORRELATIONS IN MACH 2. 46 JET AT x/D = 4

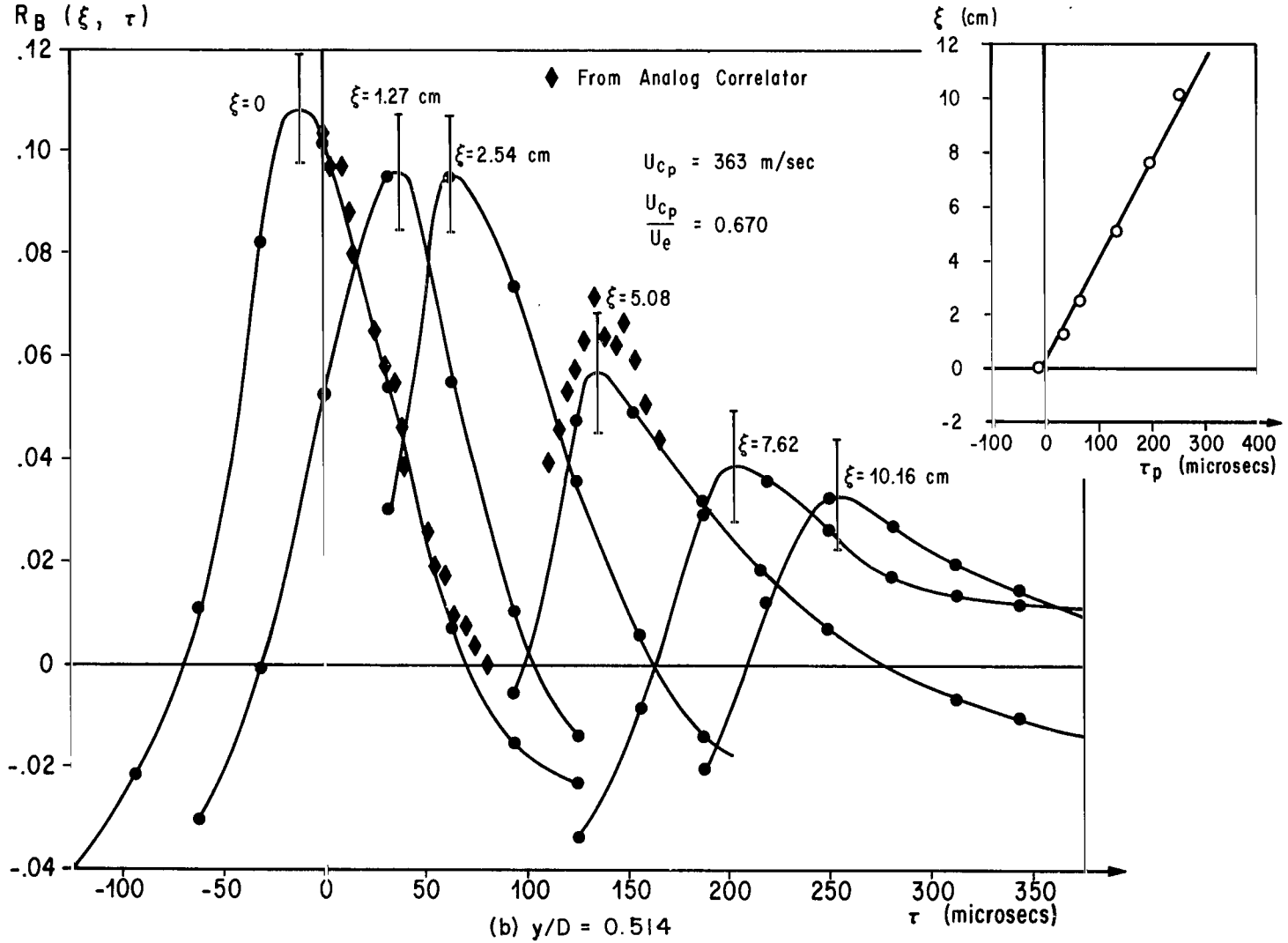

FIGURE 34. (Continued)

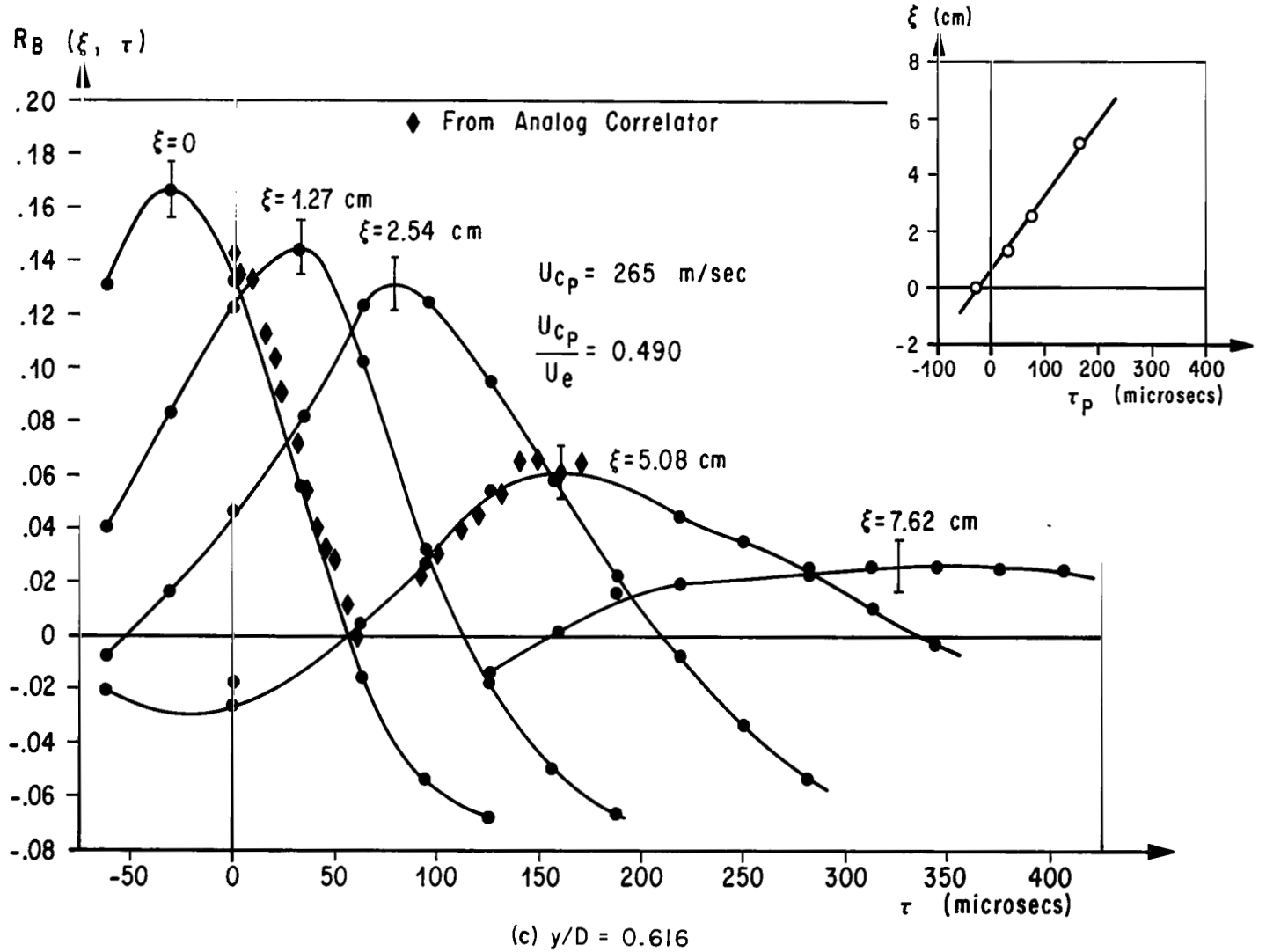

(c) y/D = 0.616

FIGURE 34. (Continued)

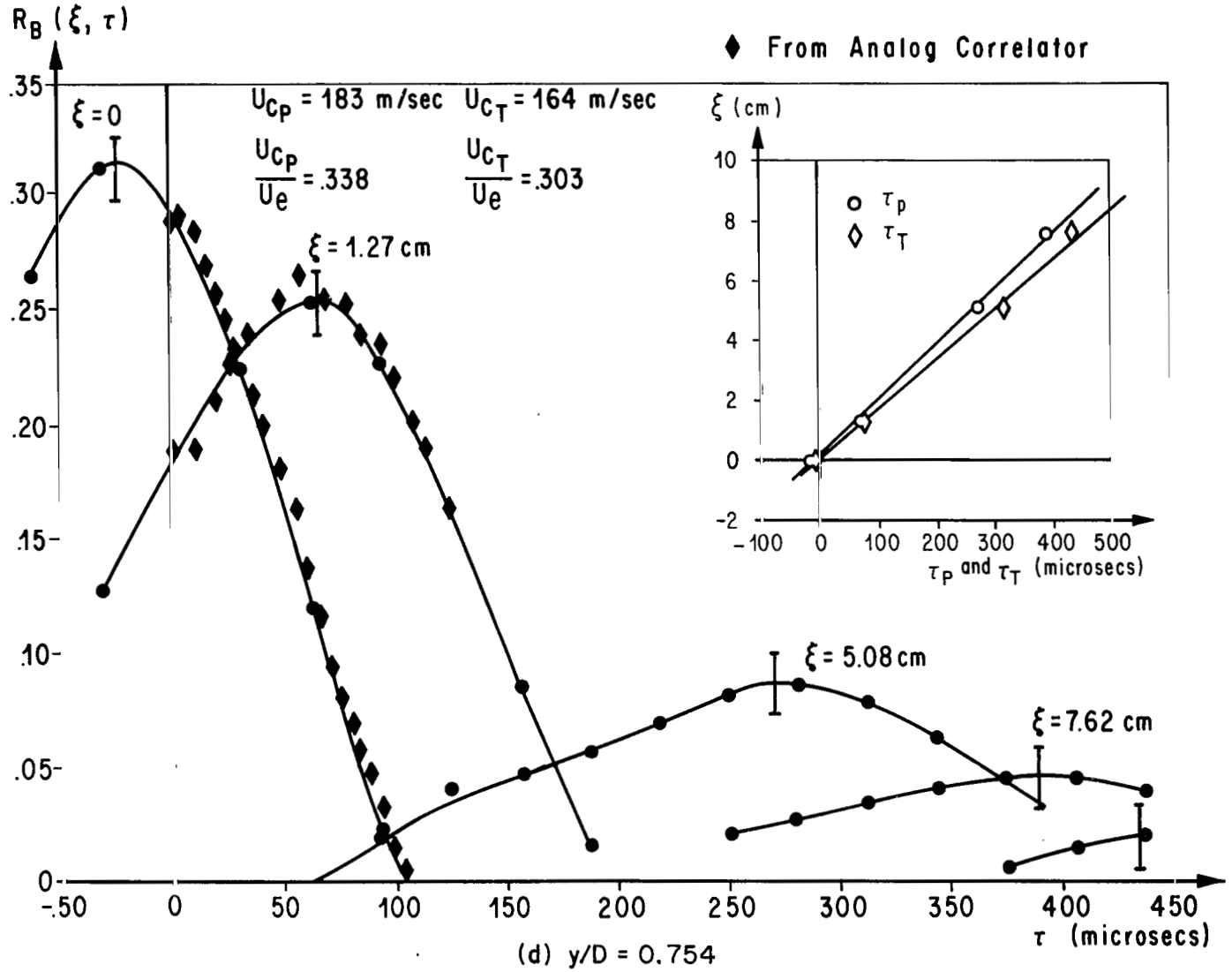

FIGURE 34. (Continued)

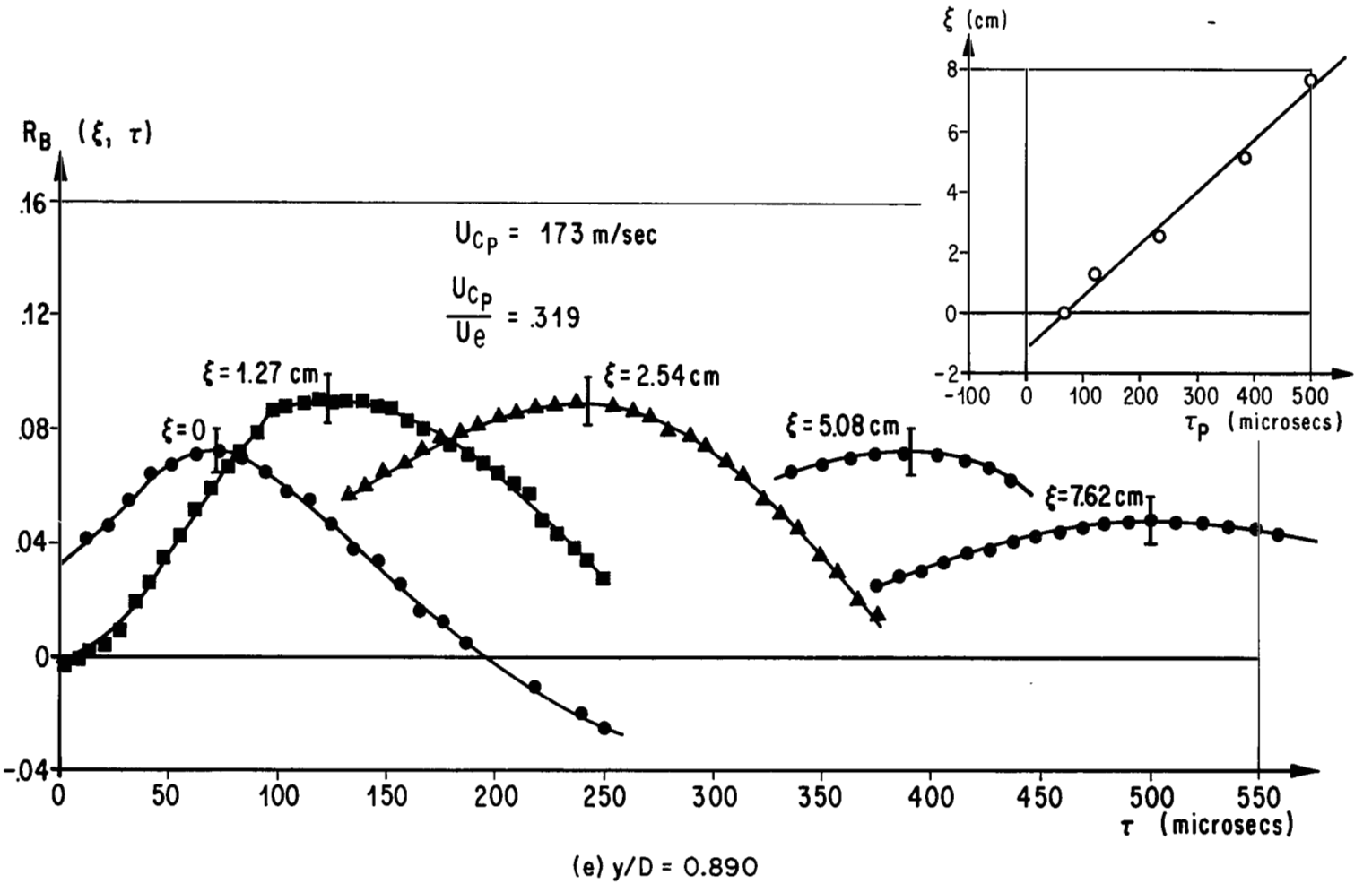

(e) y/D = 0.890

FIGURE 34. (Concluded)

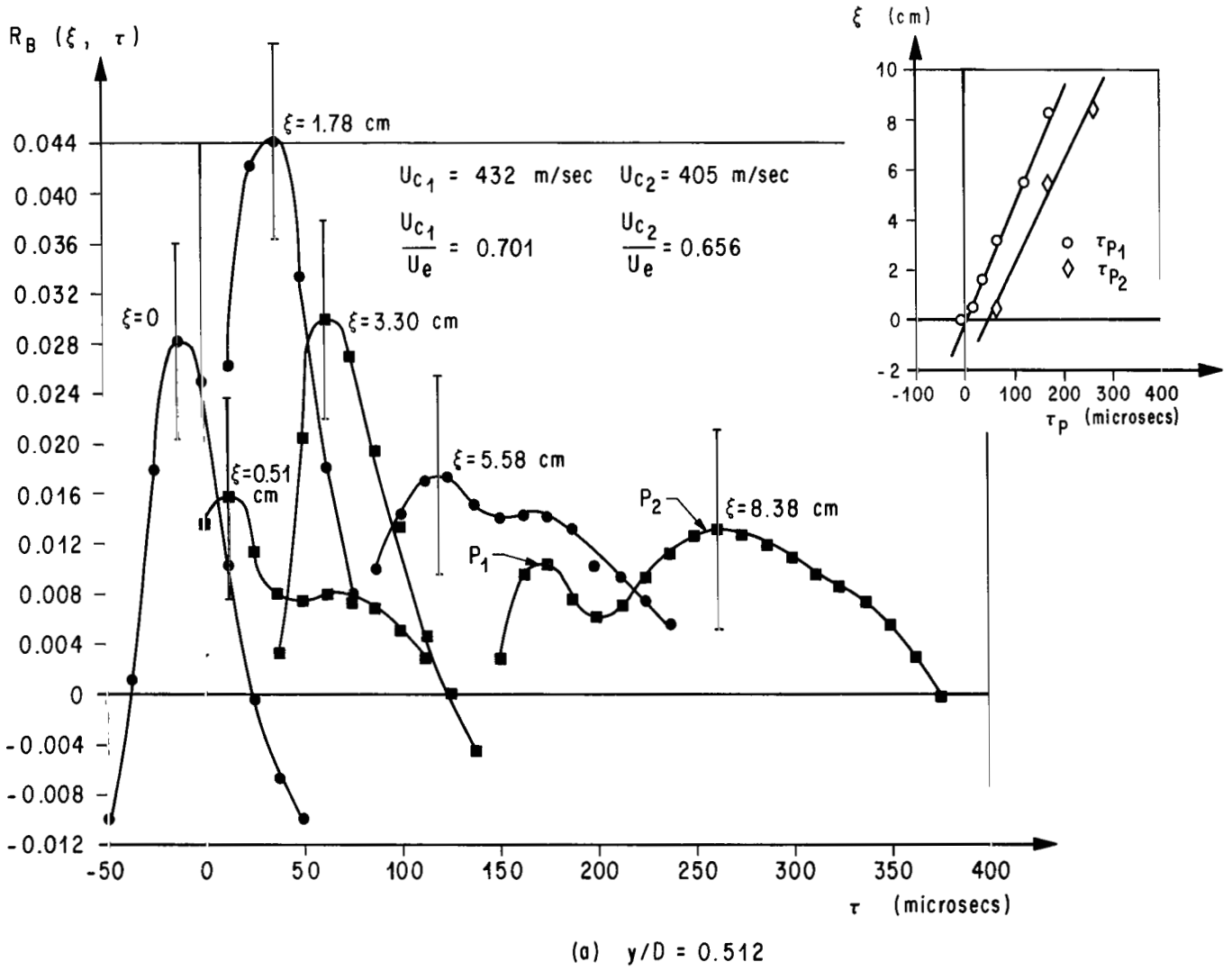

FIGURE 35. TWO BEAM SPACE-TIME CORRELATIONS IN MACH 3.34 JET AT x/D = 4

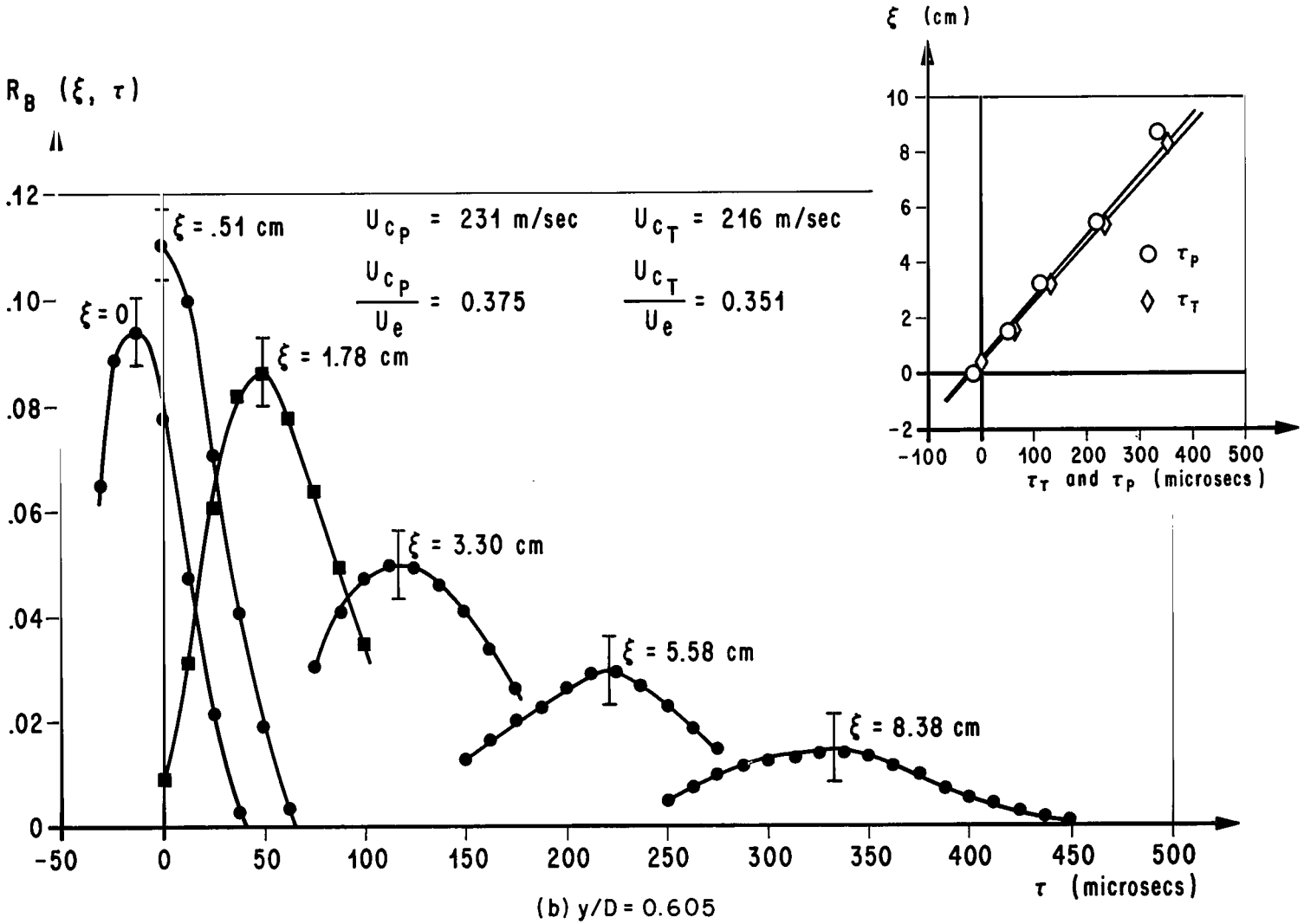

FIGURE 35. (Continued)

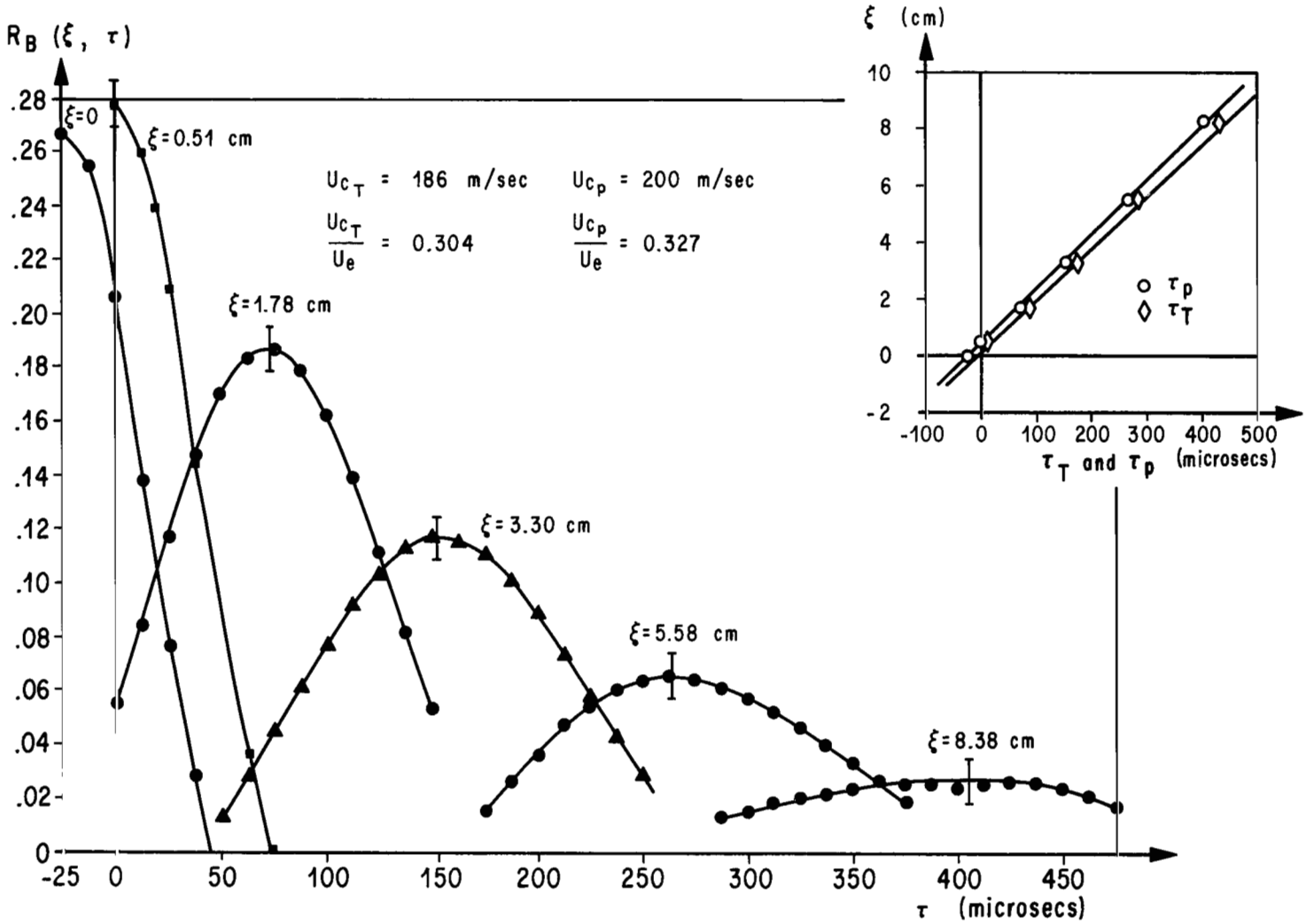

(c) y/D = 0.698

FIGURE 35. (Continued)

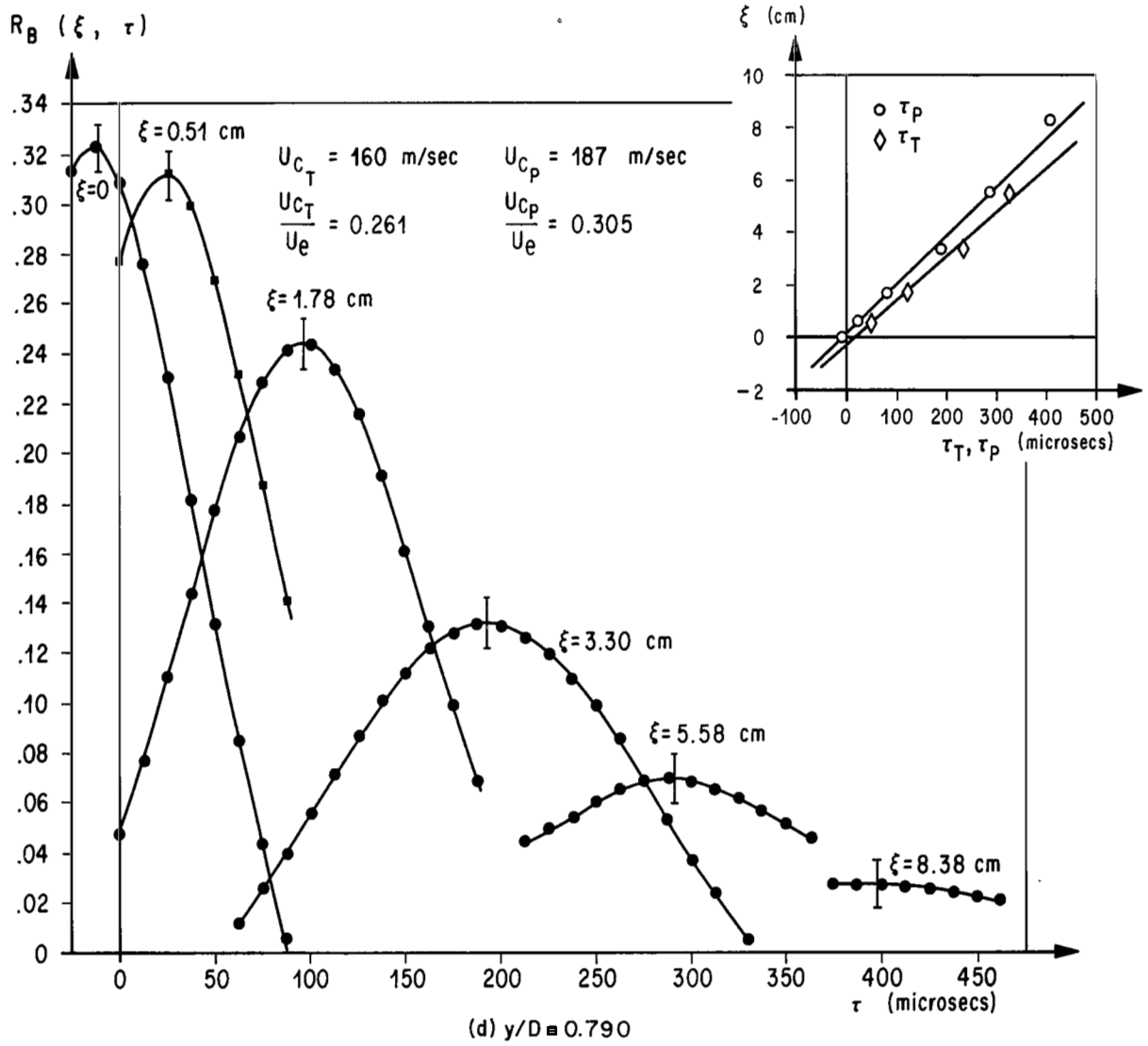

FIGURE 35. (Continued)

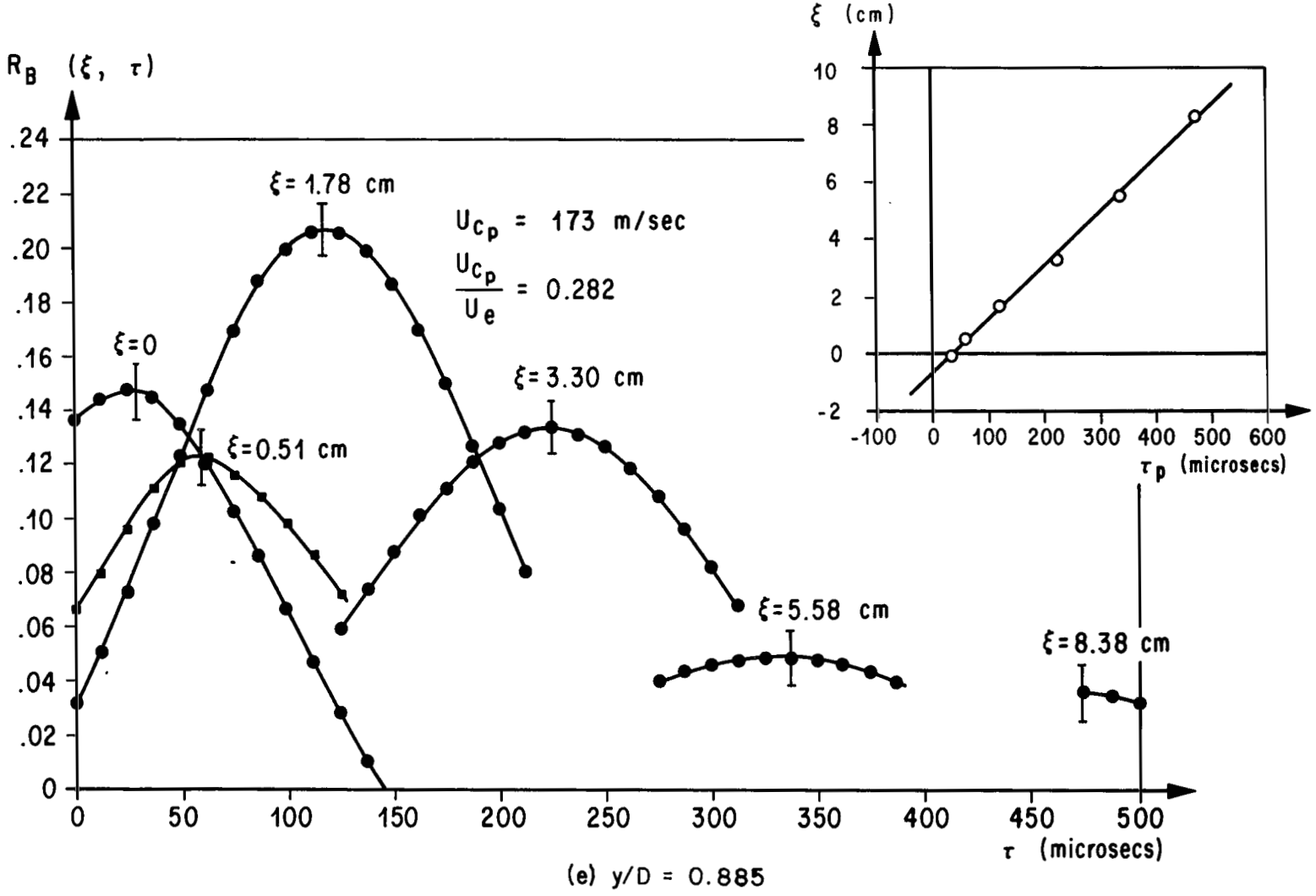

FIGURE 35. (Concluded)

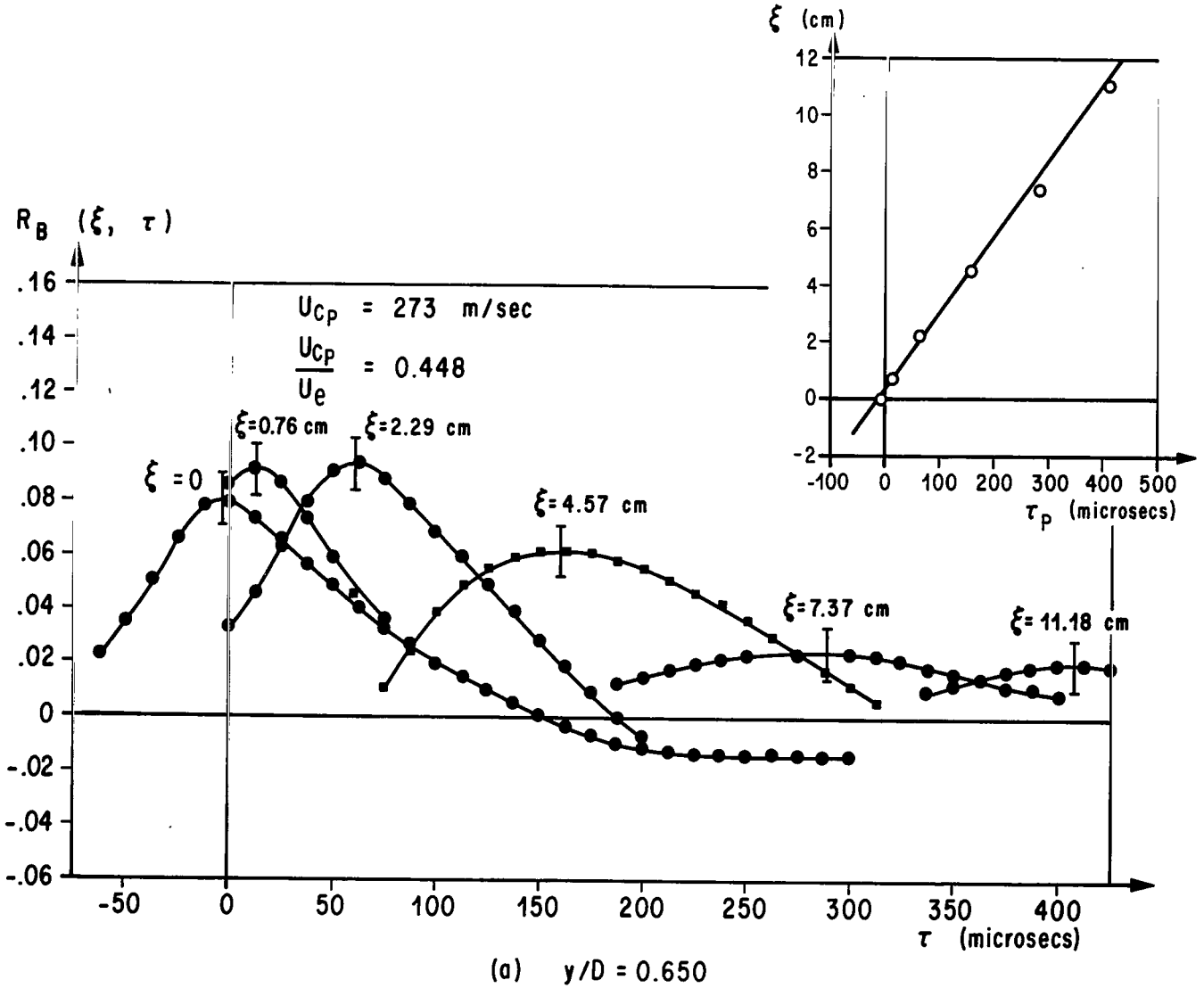

FIGURE 36. TWO BEAM SPACE-TIME CORRELATIONS IN MACH 3.34 JET AT x/D = 8

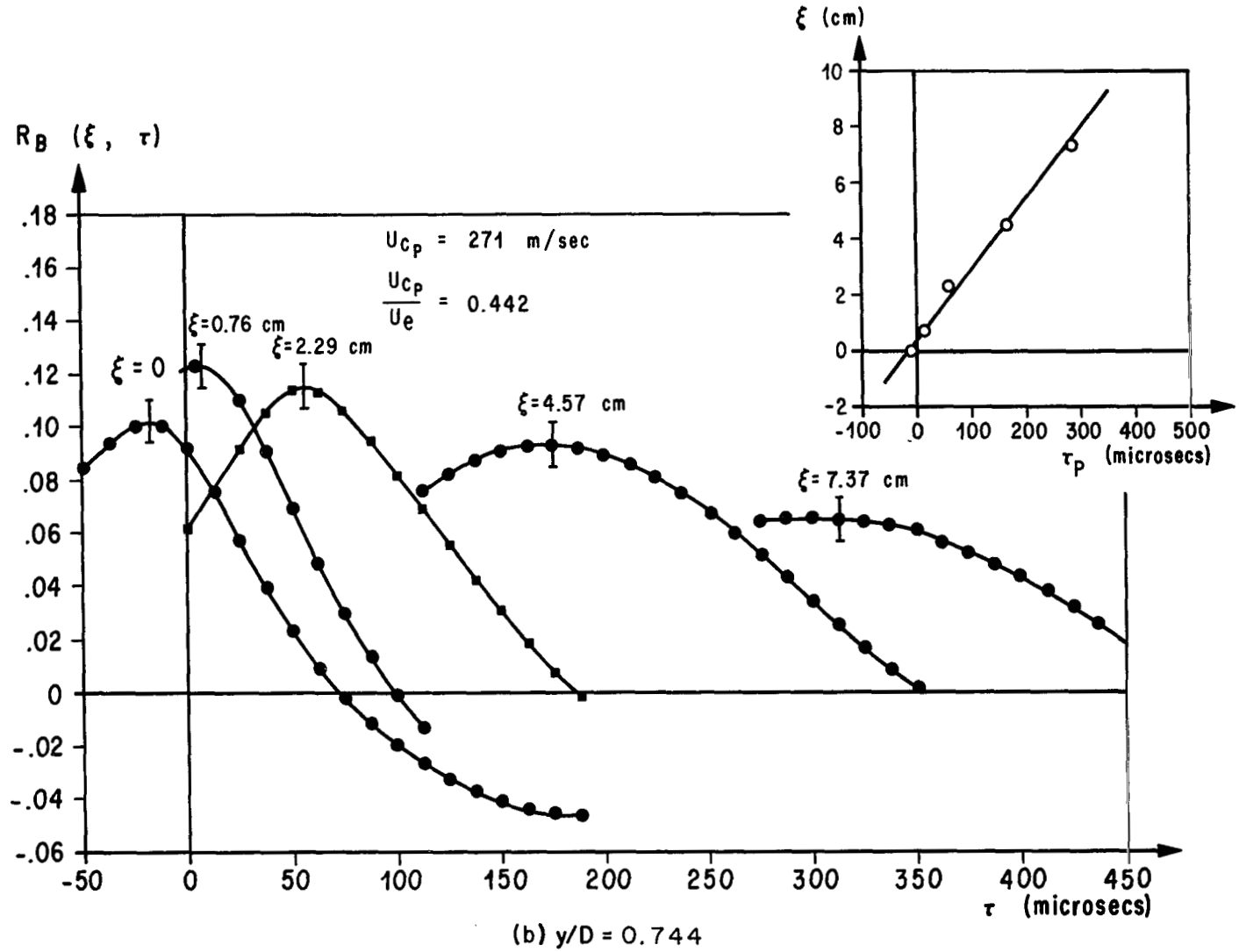

(b) y/D = 0.744

FIGURE 36. (Continued)

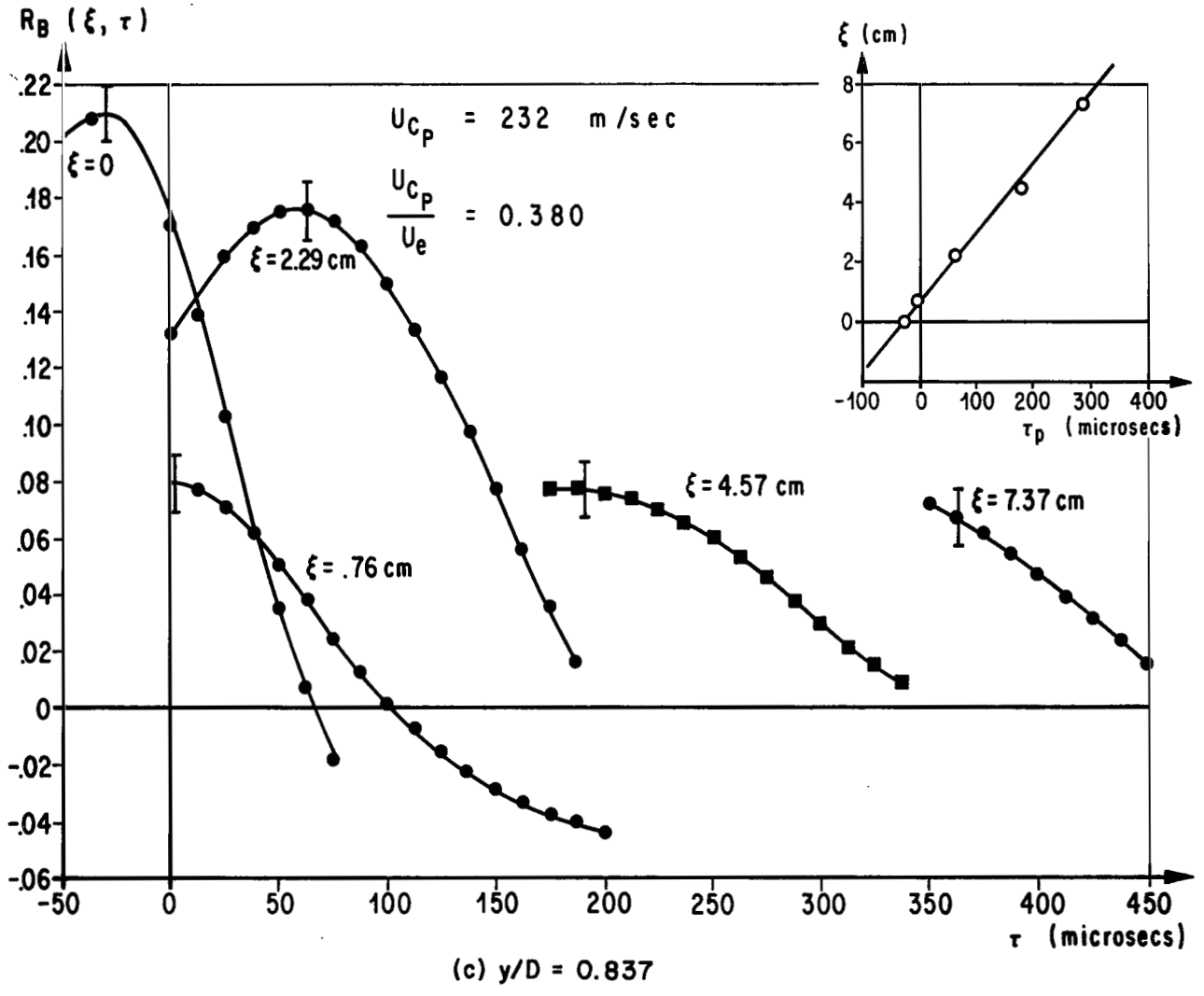

(c) y/D = 0.837

FIGURE 36. (Continued)

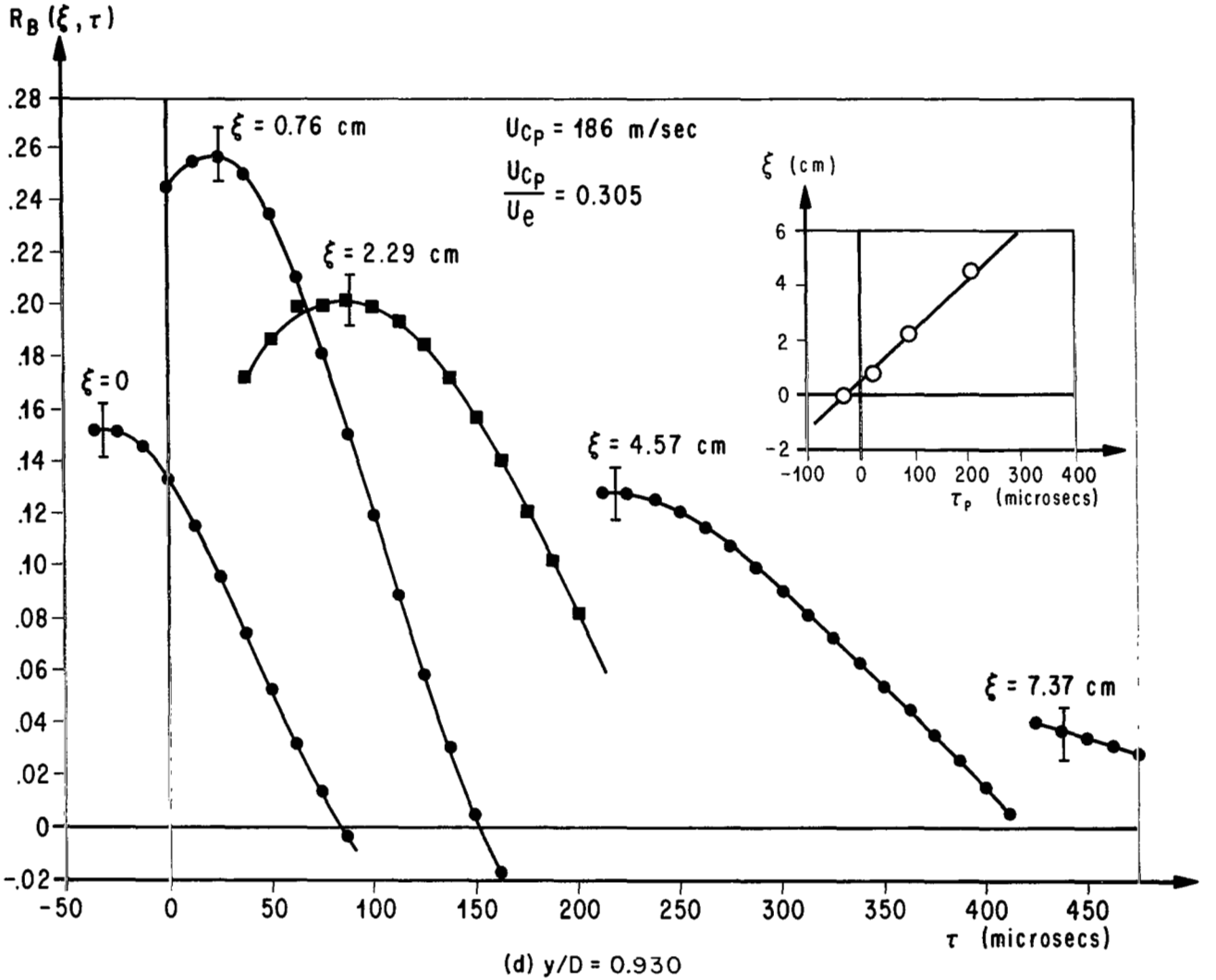

FIGURE 36. (Continued)

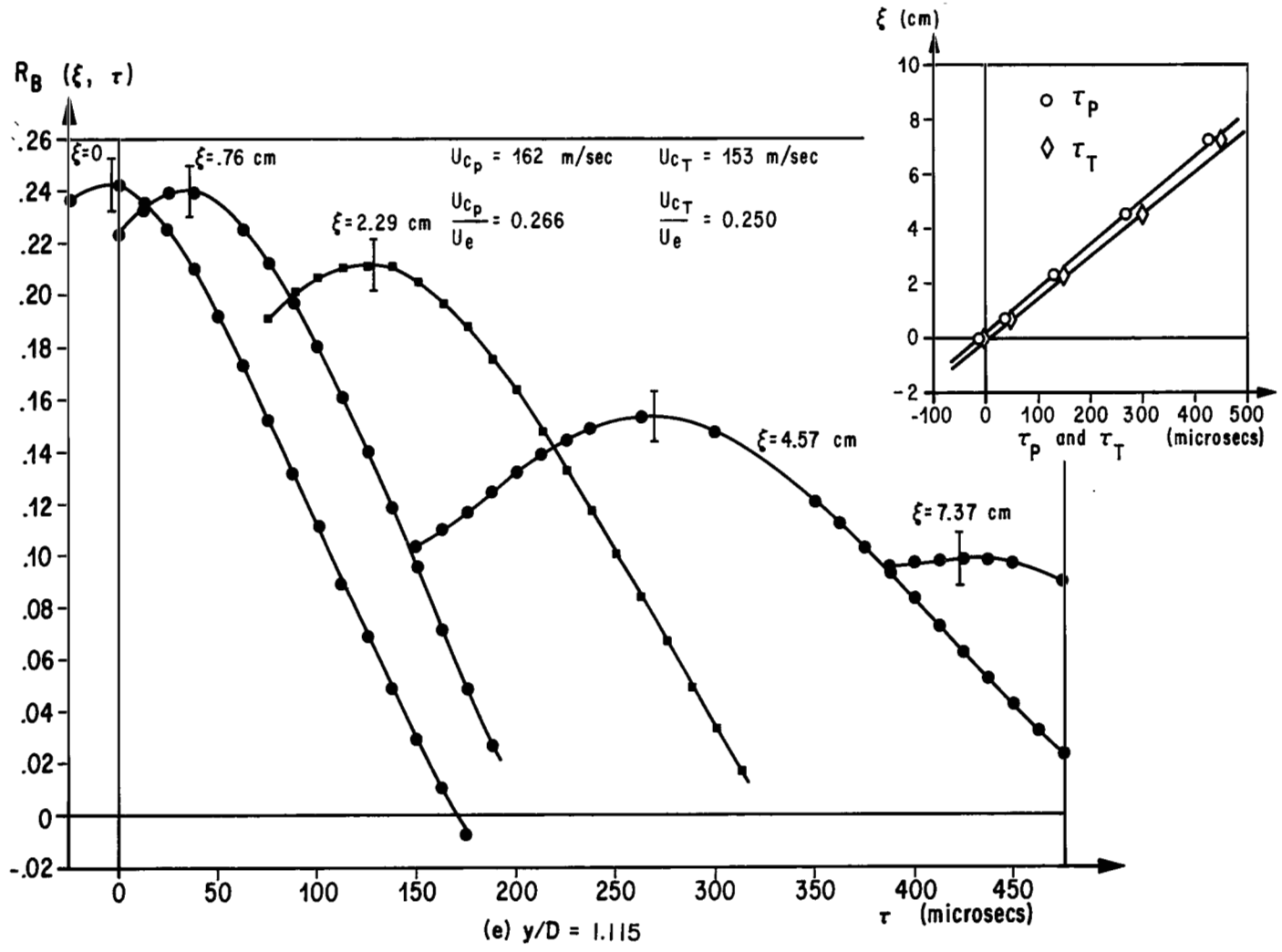

FIGURE 36. (Concluded)

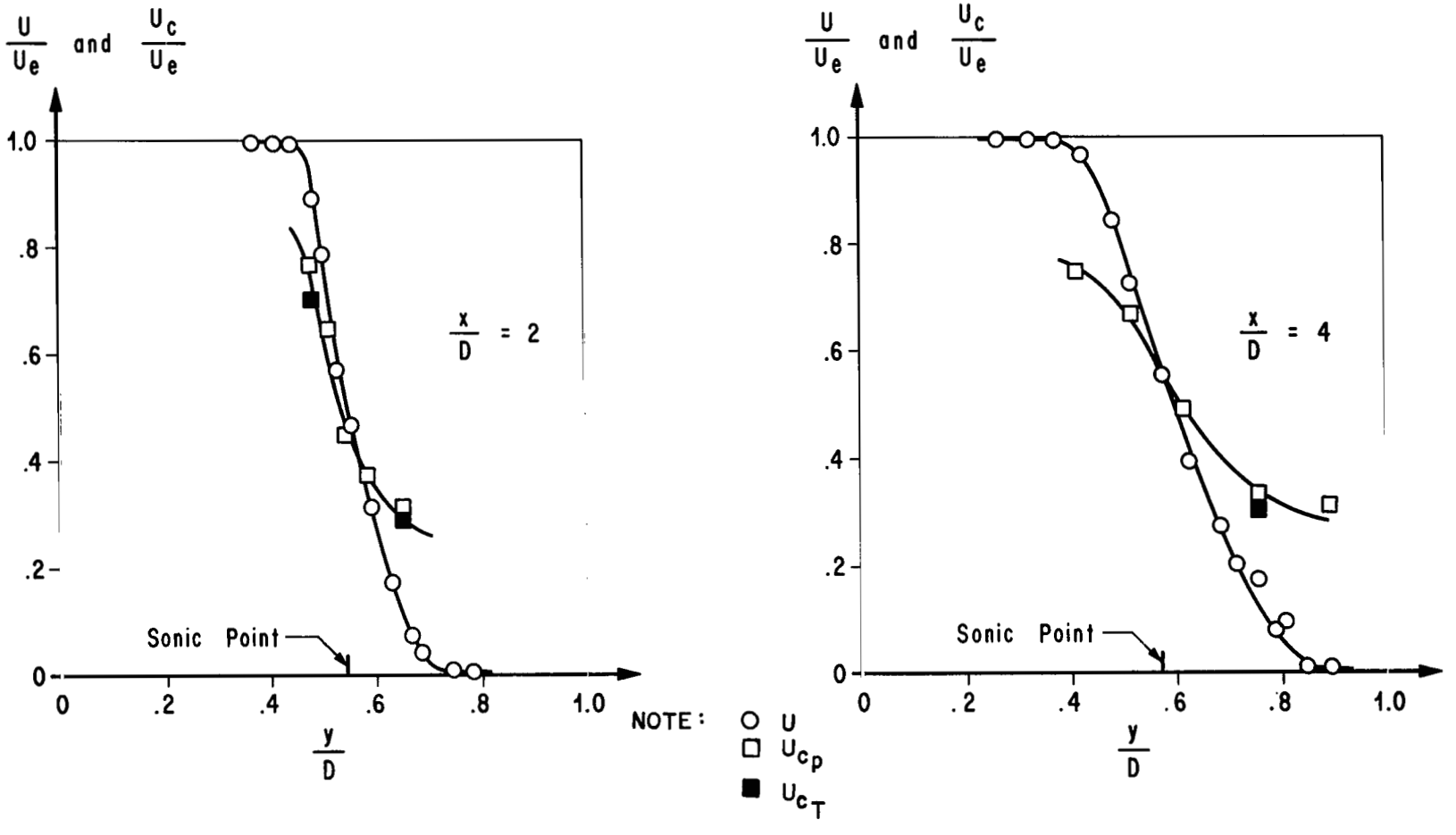

FIGURE 37. CONVECTION AND MEAN SPEED PROFILES IN MACH 2.46 JET

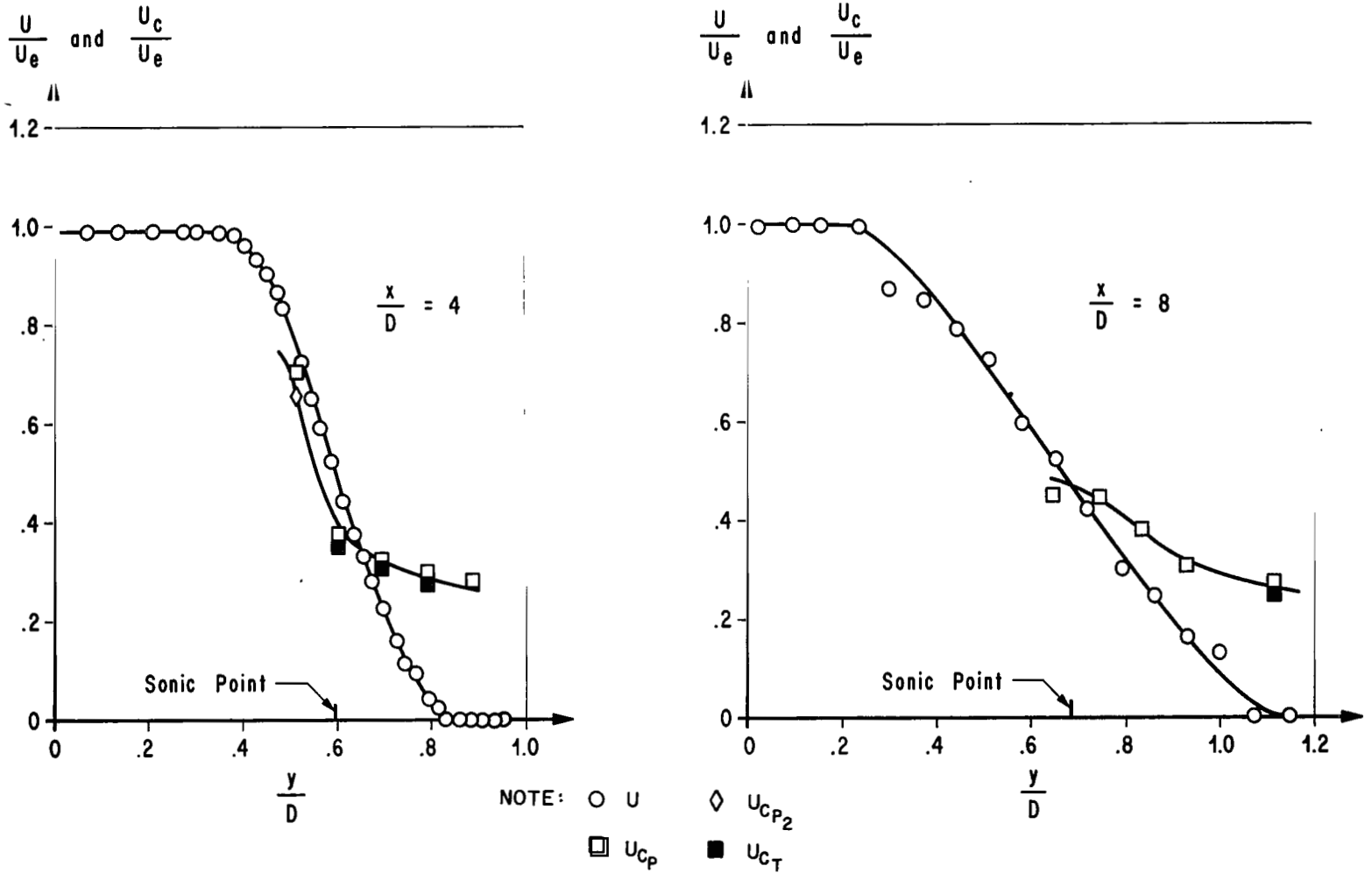

FIGURE 38. CONVECTION AND MEAN SPEED PROFILES IN MACH 3.34 JET

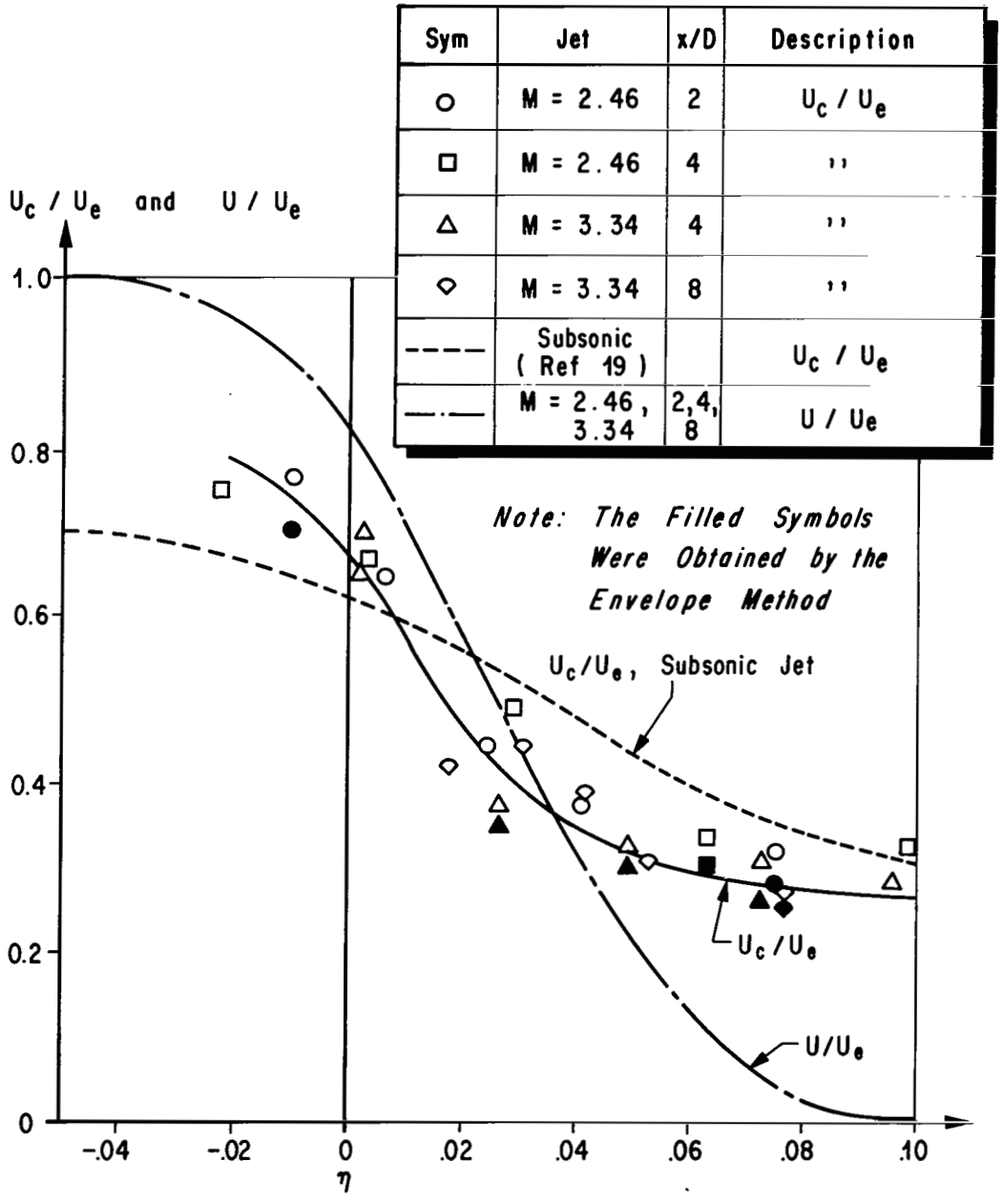

FIGURE 39. VARIATION OF CONVECTION AND MEAN SPEEDS WITH η

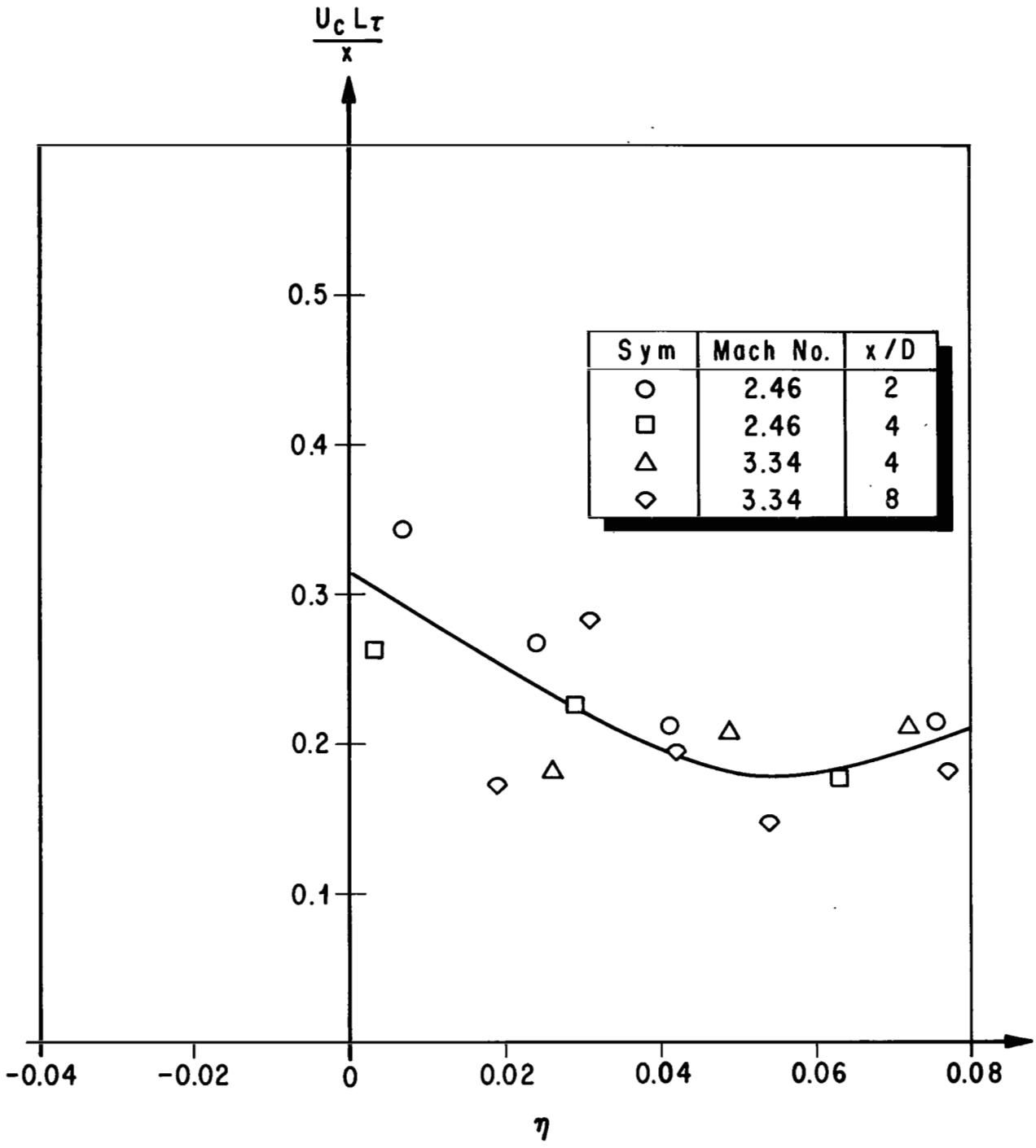

FIGURE 40. THE MOVING-AXES TIME SCALE

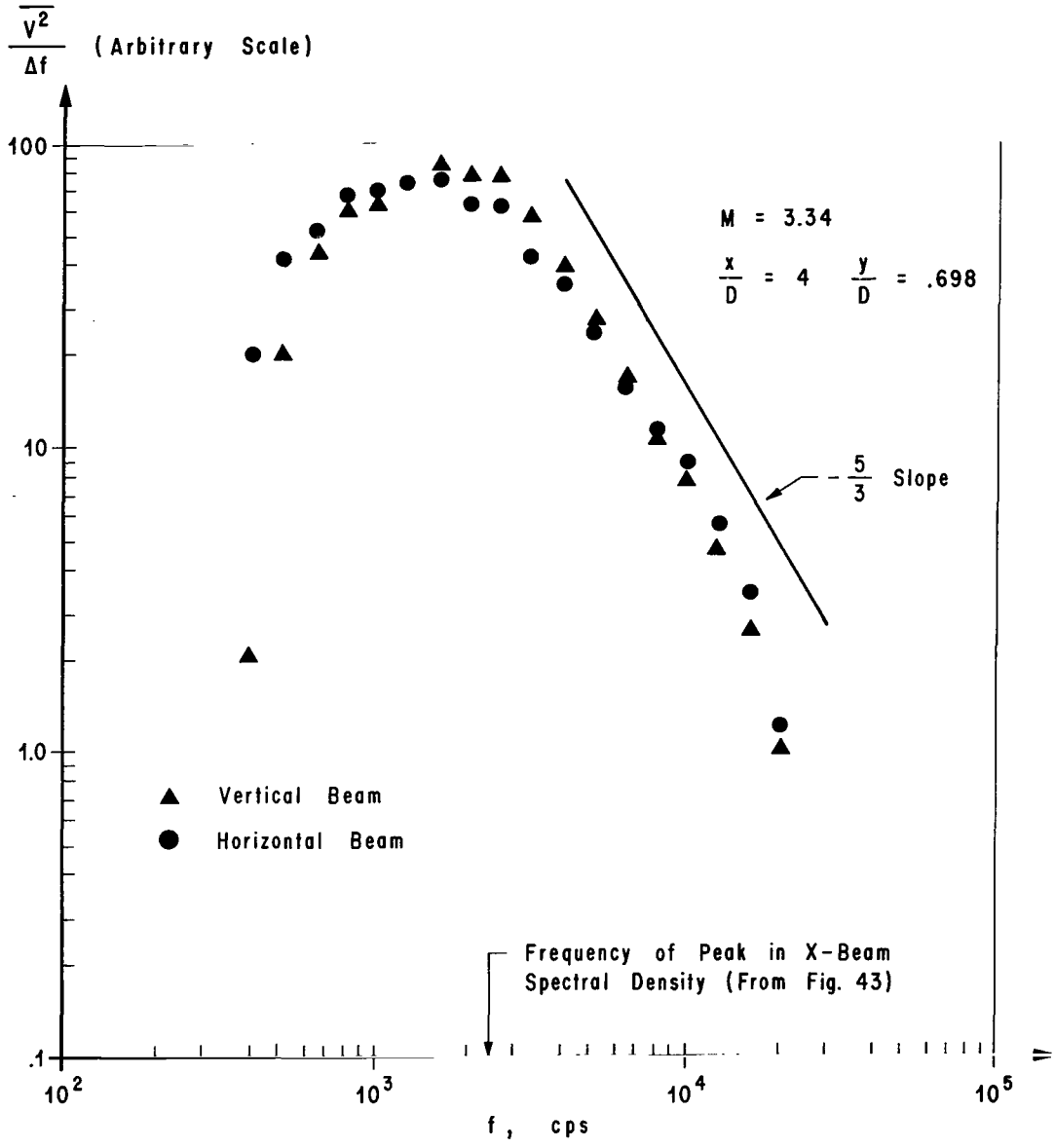

FIGURE 41. INTEGRATED SPECTRA OF THE HORIZONTAL AND VERTICAL BEAMS

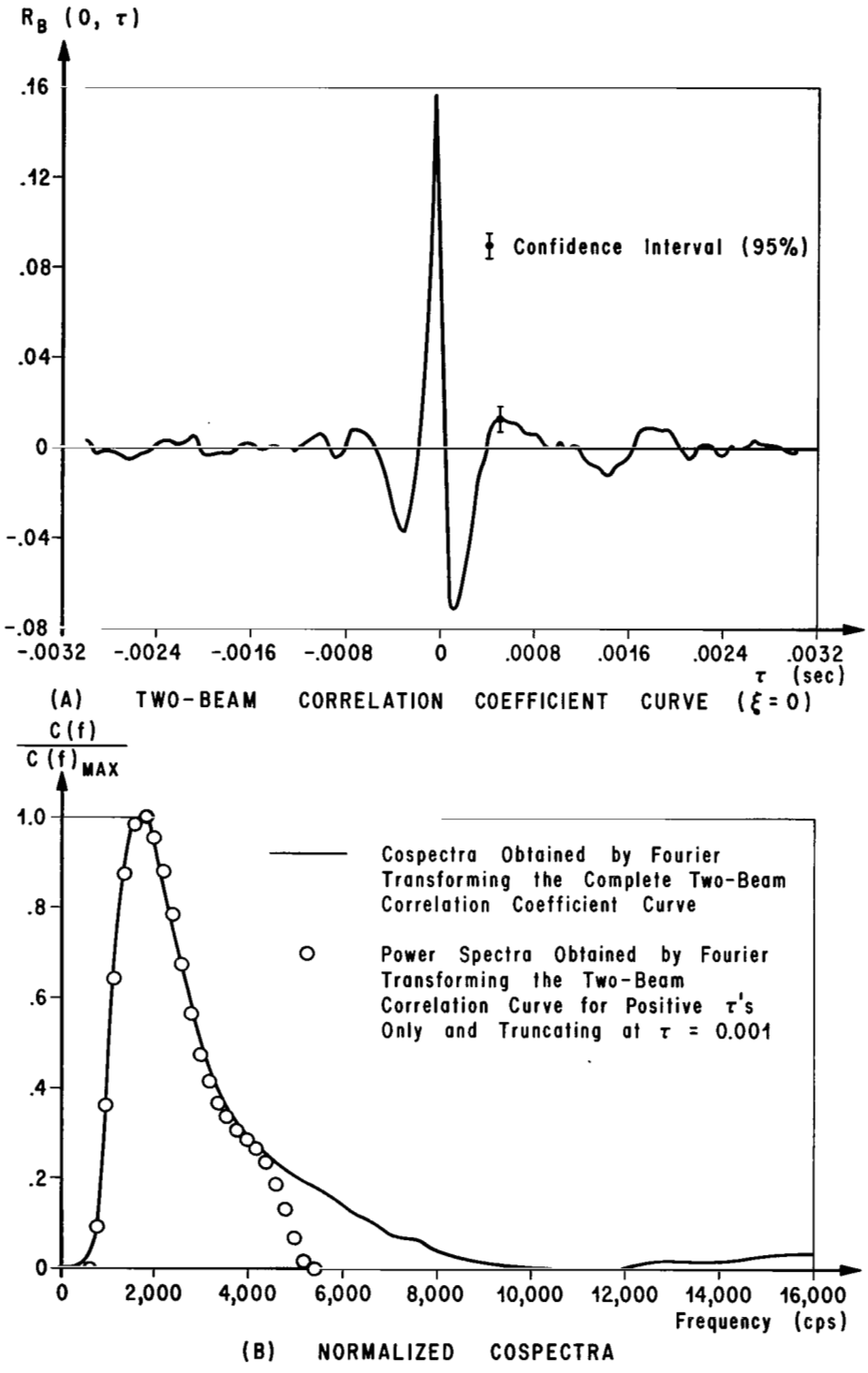

FIGURE 42. DETERMINATION OF TYPICAL SPECTRAL DENSITY CURVE
(M = 2.46, x/D = 4, y/D = 0.616)

SYM	MACH NO.	x/D	y/D	x/U_c (sec)
○	2.46	2	0.549	6.19×10^{-4}
◒	2.46	2	0.582	7.45×10^{-4}
●	2.46	2	0.652	8.63×10^{-4}
□	2.46	4	0.514	8.18×10^{-4}
▬	2.46	4	0.616	11.20×10^{-4}
■	2.46	4	0.754	16.22×10^{-4}
△	3.34	4	0.698	10.94×10^{-4}
▲	3.34	4	0.790	11.70×10^{-4}
◇	3.34	8	0.930	23.53×10^{-4}
◆	3.34	8	1.115	27.02×10^{-4}

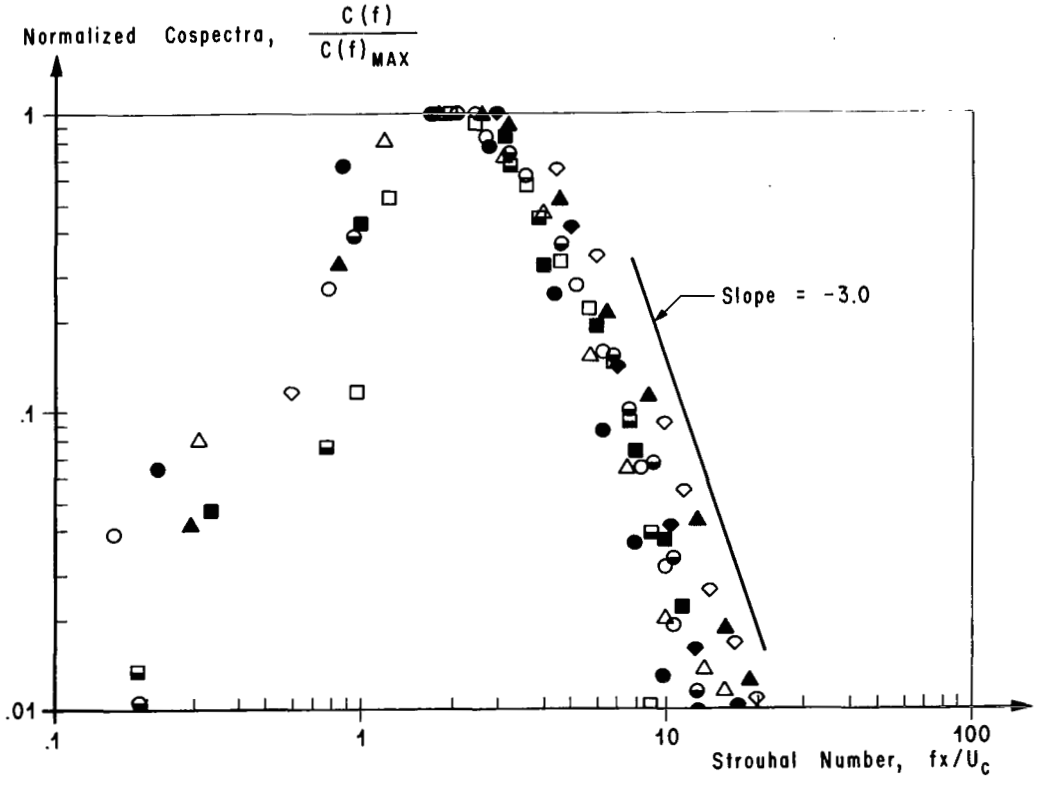

FIGURE 43. SUMMARY OF SPECTRAL DENSITY DATA

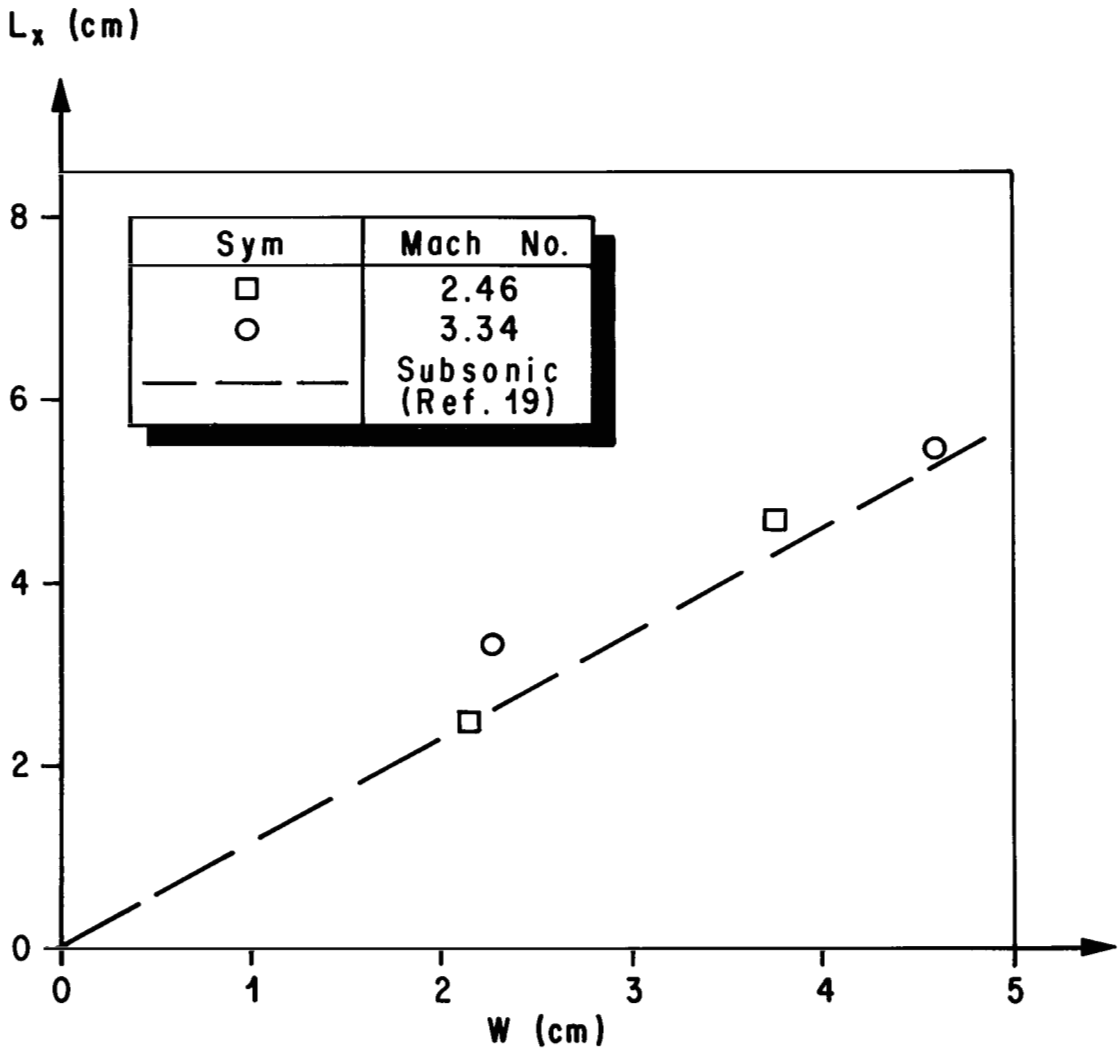

FIGURE 44. VARIATION OF STREAMWISE LENGTH SCALE WITH SHEAR LAYER THICKNESS

REFERENCES

1. Fisher, M. J., and Krause, F. R.: The Crossed-Beam Correlation Technique. J. Fluid Mech., vol. 28, part 4, 1967, pp. 705-717.

2. Fisher, M. J., and Krause, F. R.: Local Measurements in Turbulent Flows Through Cross Correlation of Optical Signals. MSFC, Aero-Astrodynamics Research Review No. 2, NASA TM X-53295, April 1965.

3. Fisher, M. J., and Damkevala, R. J.: Fundamental Considerations of the Crossed-Beam Correlation Technique. NASA CR-61252, 1969.

4. Fisher, M. J., Prosser, D. W., and Clinch, J. M.: Local Turbulence Measurements in a Supersonic Jet. Proceedings of the 1967 Heat Transfer and Fluid Mechanics Institute, Stanford University Press, 1967.

5. Krause, F. R., and Fisher, M. J.: Remote Sensing of Local Flow Instabilities and Turbulence. Proceedings of the ASME Fluid Meter 50th Anniversary Symposium, Pittsburgh, Pennsylvania, Sept. 26-29, 1966.

6. Krause, F. R., and Fisher, M. J.: Optical Integration Over Correlation Areas in Turbulent Flows. Proceeding of the fifth International Congress on Acoustics, Paper K-65, Liege, Belgium, September, 1965.

7. Van de Hulst, H. C.: Light Scattering by Small Particles. John Wiley and Sons, Inc., New York, 1962.

8. Krause, F. R.: Mapping of Turbulent Fields by Crossing Optical Beams. Invited Paper, presented at 20th Anniversary Meeting of American Physical Society, Division of Fluid Mechanics, Bethlehem, Pa., Nov. 20-22, 1967.

9. Davies, W. O., and Cann, M. W. P.: Study of Noise Generation and Turbulent Fluxes on Saturn IB and V Exhausts. Final Report, Parts I and II, Contract No. NAS8-20108, May 1967.

10. Krause, F. R., Davies, W. O., and Cann, M. W. P.: The Determination of Thermodynamic Properties with Optical Cross Correlation Methods. MSFC, Aero-Astrodynamics Research Review No. 6, NASA TM X-53647, October 1967.

REFERENCES (Continued)

11. Laurence, J. C.: Intensity, Scale, and Spectra of Turbulence in Mixing Region of Free Subsonic Jet. NACA Report 1292, 1956.

12. Hinze, J. O.: Turbulence. McGraw-Hill Book Co., Inc., New York, 1959.

13. Fisher, M. J., and Damkevala, R. J.: Shock Wave Shear Layer Interaction in Clustered Rocket Exhausts. Final Report, Contract No. NAS8-20408, October 1967.

14. Johnson, G., and Montgomery, A. J.: Survey of Detectors and Dynamic Calibration Methods for Remote Sensing Systems. NASA CR-751, April 1967.

15. Delany, B. R., and Tidmore, W. C.: Data Report of the Characteristics of a Cold Flow Free Jet Experimental Investigation. Northrop/Huntsville TR 317, April 1967.

16. Elliot, D. G., Bartz, D. R., and Silver, S.: Calculation of Turbulent Boundary Layer Growth and Heat Transfer in Axisymmetric Nozzles. JPL Report 32-387, February 1963.

17. Krause, F. R., and Hablutzel, B. C.: Noise Elimination by Piecewise Cross Correlation of Photometer Outputs. Proceedings of the National Academy of Sciences Panel on "Remote Atmospheric Probing," Chicago, Ill., May 17, 1968.

18. Bradshaw, P., Ferris, D. H., and Johnson, R. F.: Turbulence in the Noise Producing Region of a Circular Jet. AGARD Report 450, April 1963.

19. Davies, P. O. A. L., Fisher, M. J., and Barratt, M. J.: The Characteristics of the Turbulence in the Mixing Region of a Round Jet. J. Fluid Mech., vol. 15, 1963, pp. 337-367.

20. Cann, M. W. P.: Coefficient of Temperature Variation of the Ultraviolet Absorption of Air at 1850Å. IIT Research Institute Report No. J6112-VO6-2, August 1968.

21. Cann, M. W. P.: Pressure and Temperature Dependence of the Ultraviolet Absorption of Air. IIT Research Institute Report No. 22-08-1, August 1968.

REFERENCES (Concluded)

22. Penndorf, R. B.: New Tables of Mie Scattering Functions for Spherical Particles. Part 6: Total Mie Scattering Coefficients for Real Refractive Indices. AFCRC-TR-56-204 (6), or ASTIA Document Number AD-98772, March 1956.

23. Wilcox, Donald E., Weir, Alexander, Nicholls, J. A., and Dunlap, Roger: Location of Mach Discs and Diamonds in Supersonic Air Jets. J. of the Aeronautical Sciences, vol. 24, February 1957.

24. Fisher, M. J., and Davies, P. O. A. L.: Correlation Measurements in a Non-frozen Pattern of Turbulence. J. Fluid Mech., vol. 19, 1964, pp. 97-116.

25. Corrsin, Stanley: The Decay of Isotropic Temperature Fluctuations in an Isotropic Turbulence, Jour. of Aeronautical Sciences, vol. 18, 1951, pp. 417-423.

26. Johnson, Donald S.: Turbulent Heat Transfer in a Boundary Layer With Discontinuous Wall Temperature. Ph. D. Dissertation, Johns Hopkins University, 1955.

NASA-Langley, 1970 —— 12 M143

NATIONAL AERONAUTICS AND SPACE ADMINISTRATION
WASHINGTON, D.C. 20546

OFFICIAL BUSINESS

FIRST CLASS MAIL

POSTAGE AND FEES PAID
NATIONAL AERONAUTICS AND
SPACE ADMINISTRATION

"The aeronautical and space activities of the United States shall be conducted so as to contribute . . . to the expansion of human knowledge of phenomena in the atmosphere and space. The Administration shall provide for the widest practicable and appropriate dissemination of information concerning its activities and the results thereof."

—NATIONAL AERONAUTICS AND SPACE ACT OF 1958

NASA SCIENTIFIC AND TECHNICAL PUBLICATIONS

TECHNICAL REPORTS: Scientific and technical information considered important, complete, and a lasting contribution to existing knowledge.

TECHNICAL NOTES: Information less broad in scope but nevertheless of importance as a contribution to existing knowledge.

TECHNICAL MEMORANDUMS: Information receiving limited distribution because of preliminary data, security classification, or other reasons.

CONTRACTOR REPORTS: Scientific and technical information generated under a NASA contract or grant and considered an important contribution to existing knowledge.

TECHNICAL TRANSLATIONS: Information published in a foreign language considered to merit NASA distribution in English.

SPECIAL PUBLICATIONS: Information derived from or of value to NASA activities. Publications include conference proceedings, monographs, data compilations, handbooks, sourcebooks, and special bibliographies.

TECHNOLOGY UTILIZATION PUBLICATIONS: Information on technology used by NASA that may be of particular interest in commercial and other non-aerospace applications. Publications include Tech Briefs, Technology Utilization Reports and Technology Surveys.

Details on the availability of these publications may be obtained from:

SCIENTIFIC AND TECHNICAL INFORMATION DIVISION

NATIONAL AERONAUTICS AND SPACE ADMINISTRATION

Washington, D.C. 20546